



**Critical process parameters for optimum yield of  $\text{Co}_3\text{O}_4$  catalyst for application in textile effluent treatment**

**by**

**Jorika Theart**

**Thesis submitted in fulfilment of the requirements for the degree**

**Master of Engineering in Chemical Engineering**

**in the Faculty of Engineering & the Built Environment**

**at the Cape Peninsula University of Technology, Cape Town**

**Supervisor: Prof. Veruscha Fester**

**CPUT copyright information**

The thesis may not be published either in part (in scholarly, scientific or technical journals), or as a whole (as a monograph), unless permission has been obtained from the University.

## Declaration

I, Jorika Theart, hereby declare that this research dissertation is my own unaided work. It is being submitted for the MEng Degree at the Cape Peninsula University of Technology. It has not been submitted before for any degree or examination in any other University. Furthermore, it represents my own opinions and not necessarily those of the Cape Peninsula University of Technology.

Signed



11 March 2023

Date

## Abstract

The interest in nanostructured materials has increased due to the electrical, catalytic, optimal and magnetic properties of the nanoscale particles that are uniquely different from those of their corresponding bulk counterparts. The technological applications of  $\text{Co}_3\text{O}_4$  nanostructures such as solid-state sensors, anode materials in lithium-ion rechargeable batteries, electrochromic sensors, heterogeneous catalyst, energy storage and magnetic materials have drawn attention to the controlled synthesis of these nanomaterials. There is a lack in the understanding of the effect of synthesis operating conditions (such as reaction temperature, residence time, type of precursor anion and precursor concentration) and their interactions on the produced  $\text{Co}_3\text{O}_4$  nanoparticles. During this study the produced  $\text{Co}_3\text{O}_4$  nanostructures were applied as a catalyst for the degradation of methyl orange (MO) solution to establish if there is a relationship between the product yield, crystallite size and the degradation percentage. The chemicals that are used during the dyeing process as well as the structure of the dyestuff makes the generated effluent highly polluted and difficult to treat. Advantaged oxidation processes (AOP) have gained considerable interest due to the low selectivity to organic pollutants in wastewater. AOPs involve the generation of hydroxyl free radicals by using different oxidants that ultimately destroy components that are not removed under conventional oxidation processes.

During this study, a  $\text{Co}_3\text{O}_4$  nanocatalyst was produced through the hydrothermal synthesis using three precursor salts with different counter anions (cobalt acetate tetrahydrate, cobalt chloride and cobalt nitrate). A factorial design (face-centred central composite design) was applied to create a design that would produce a prediction model to evaluate the effect of the operating parameters (reaction temperature, precursor concentration and residence time) on the product yield and crystallite size. X-ray diffraction (XRD) analysis showed that after calcination  $\text{Co}_3\text{O}_4$  nanostructures were produced.

Comparing the maximum yield obtained for each precursor the order was as follows:  $\text{Co}(\text{NO}_3)_2 \cdot 6\text{H}_2\text{O}$  (100%) >  $\text{CoCl}_2 \cdot 6\text{H}_2\text{O}$  (82%) >  $\text{Co}(\text{C}_2\text{H}_3\text{O}_2)_2$  (66%). The product yields obtained for  $\text{Co}(\text{NO}_3)_2 \cdot 6\text{H}_2\text{O}$ -derived  $\text{Co}_3\text{O}_4$  ranged from 56% to 100%. The product yields obtained for  $\text{CoCl}_2 \cdot 6\text{H}_2\text{O}$ -derived  $\text{Co}_3\text{O}_4$  ranged from 1% to 82%. The product yields obtained for  $\text{Co}(\text{C}_2\text{H}_3\text{O}_2)_2$ -derived  $\text{Co}_3\text{O}_4$  ranged from 12% to 66%.

The crystallite size of  $\text{Co}(\text{NO}_3)_2 \cdot 6\text{H}_2\text{O}$ - and  $\text{Co}(\text{C}_2\text{H}_3\text{O}_2)_2$ -precursor derived  $\text{Co}_3\text{O}_4$  presented the same trends and ranged between 4.15 nm and 21.22 nm. For  $\text{CoCl}_2 \cdot 6\text{H}_2\text{O}$ -derived  $\text{Co}_3\text{O}_4$  nanoparticles, the crystallite sizes ranged between 3.06 nm and 17.97 nm.

Methyl orange (MO) was treated using peroxymonosulfate that was activated by the synthesised heterogeneous  $\text{Co}_3\text{O}_4$  nanocatalyst for 30 minutes. Comparing the efficiency of the  $\text{Co}_3\text{O}_4$  nanocatalyst that was produced by three different precursor salts; it was found that  $\text{Co}(\text{NO}_3)_2 \cdot 6\text{H}_2\text{O}$  –derived  $\text{Co}_3\text{O}_4$  nanocatalyst performed the best, removing 96% of the MO solution while  $\text{Co}(\text{C}_2\text{H}_3\text{O}_2)_2$ –precursor derived  $\text{Co}_3\text{O}_4$  nanocatalyst performed the worst, only removing 67.93%.

A cost comparative analysis on the synthesis cost of  $\text{Co}_3\text{O}_4$  via various cobalt precursors and treatment cost of MO solution was used to evaluate the viability of a full-scale treatment process. It was found that  $\text{Co}(\text{NO}_3)_2 \cdot 6\text{H}_2\text{O}$ -derived  $\text{Co}_3\text{O}_4$  nanocatalyst is the most cost efficient and had the best performance in the treatment of MO solution. The production process involves low reaction temperature and residence time to achieve the maximum yield whereas  $\text{CoC}_{12}\text{H}_6\text{O}$  and  $\text{Co}(\text{C}_2\text{H}_3\text{O}_2)_2$  precursor salts have the higher requirements for the process conditions.

## **Dedication**

To my wonderful and loving parents,  
Johan Theart and Magdelt Theart

Thank you for your encouragement, support and guidance through this journey.

## ACKNOWLEDGEMENTS

To Professor Veruscha Fester, thank you for guidance, support and encouragement. I am grateful for the opportunity to pursue this research under your supervision. Thank you for never giving up on me and pushing me to higher grounds.

To Mr Nico Laubscher for your guidance and advice on the application of Design-Expert and statistical analysis.

I thank the Eyethu Community Trust (administered by the Nedbank Foundation) for the financial support.

To the staff in the FPRC unit: Mr Siyasanga Makaluza, Ms Pamela Matshaya, Mr Richard du Toit, Mr Kwezi Xashimba and Mr Sbongiseni Ntombela for your administrative and laboratory assistance. None of this would have been possible without you and every task is appreciated.

I would like to thank Mr Remy Bucher from iThemba Labs for your aid in the characterisation of my nanostructures.

To Christian Theart, Robert Theart, Jevanè Loots, Gerrit Maass and Whitney Heuvel. Thank you for your encouraging, love and support throughout the years.

# Table of contents

Chapter 1	Introduction.....	1
1.1.	Background and Motivation.....	1
1.2.	Statement of the research problem.....	3
1.3.	Aims and objectives.....	3
1.4.	Significance.....	3
1.5.	Delineation.....	3
1.6.	Thesis structure.....	4
Chapter 2	Literature Review.....	6
2.1.	Introduction.....	6
2.2.	Metal oxide nanoparticles.....	6
2.3.	Methods for synthesis of nanoparticles.....	10
2.3.1.	Introduction.....	10
2.3.2.	Solid State Reaction.....	10
2.3.3.	Chemical and physical vapour phase reactions.....	11
2.3.4.	Co-precipitation synthesis.....	11
2.3.5.	Micro-emulsion synthesis.....	12
2.3.6.	Sol-gel synthesis.....	12
2.3.7.	Hot injection.....	13
2.3.8.	Hydrothermal synthesis.....	13
2.4.	Application of metal oxide nanostructures as catalysts for the treatment of textile wastewater.....	23
2.4.1.	Catalyst.....	23
2.4.2.	Treatment processes of textile wastewater.....	26
2.4.3.	Treatment of textile wastewater.....	28
2.5.	Design of experiments.....	37
2.5.1.	Response surface methodology.....	38
2.5.2.	Analysis of variance.....	39
2.6.	Material characterisation techniques.....	40

2.6.1.	X-ray diffraction.....	40
2.6.2.	Brubauer, Emmett and Teller (BET) surface area .....	41
2.5	Conclusions .....	42
Chapter 3	Experimental Procedure .....	44
3.1.	Introduction .....	44
3.2.	Research design .....	44
3.3.	Experimental methods .....	46
3.4.	Evaluation of the catalytic efficiency of the produced catalyst .....	48
3.5.	Characterisation methods .....	49
3.6.	Conclusions .....	50
Chapter 4	Effect of the process conditions on the product yield and crystallite size.....	51
4.1	Introduction .....	51
4.2	Effect of process conditions on precursor complex solution, cobalt hydroxide and cobalt oxide .....	55
4.2.1	Samples obtained after hydrothermal synthesis .....	55
4.2.2	Samples obtained after calcination .....	56
4.3	The effect of operating parameters on the yield and crystallite size of the produced nanocatalyst .....	59
4.3.1	Effect of process parameters on the yield of produced nanocatalyst.....	63
4.3.2	Effect of process parameters on the crystallite size of produced nanocatalyst.....	69
4.3.3	Final summary based on the findings.....	76
Chapter 5	Evaluation of the synthesised Co <sub>3</sub> O <sub>4</sub> nanoparticles during colour degradation.....	80
5.1	Introduction .....	80
5.2	Degradation studies using Co <sub>3</sub> O <sub>4</sub> nanocatalyst to treat MO dye water .....	80
5.3	Effect of process parameters for the production of the produced Co <sub>3</sub> O <sub>4</sub> nanocatalyst on the degradation of methyl orange .....	83
5.4	Effect of Co <sub>3</sub> O <sub>4</sub> crystallite size and surface area on the degradation percentage... ..	88
5.5	Final summary based on the findings.....	90
Chapter 6	Cost comparison analysis on the production cost of Co <sub>3</sub> O <sub>4</sub> via various precursors.....	92

6.1	Calculation of cost.....	92
6.2	Conclusions .....	98
Chapter 7	Conclusions and Recommendations.....	100
7.1.	Introduction .....	100
7.2.	Conclusions .....	100
7.2.1	Effect of process conditions on product yield .....	100
7.2.2	Effect of process conditions on crystallite size .....	101
7.2.3	Degradation of MO solution by synthesised $\text{Co}_3\text{O}_4$ nanocatalyst.....	102
7.2.4	Cost comparison analysis on the production and treatment cost of $\text{Co}_3\text{O}_4$ via various precursors .....	103
7.3.	Recommendations for future studies.....	104
Reference List.....		105
Appendix A .....		115
Basis of Safety and Safety Precautions.....		115

## List of figures

Figure 2.1: Quantity of cobalt measured in treated wastewater (taken from Depgni, 2020) ...	9
Figure 2.2: Photograph and schematic representation of a laboratory autoclave (taken from Zheng, 2009) .....	14
Figure 2.3: XRD patterns of (a) $\text{CoCO}_3$ nanoparticles and (b) $\text{Co}_3\text{O}_4$ nanoparticles (taken from Nassar, 2013) .....	15
Figure 2.4: SEM images of $\text{CoCO}_3$ nanoparticles produced by a) cobalt acetate, b) cobalt chloride and c) cobalt nitrate (taken from Nassar and Ahmed, 2011) .....	16
Figure 2.5: XRD patterns for a) $\alpha\text{-Co(OH)}_2$ and b) $\beta\text{-Co(OH)}_2$ (taken from Al-Ghoul et al., 2010). .....	17
Figure 2.6: XRD patterns for the $\text{Co}_3\text{O}_4$ nanoparticles produced with cobalt chloride hexahydrate and cobalt nitrate hexahydrate precursors (taken from Heuvel, 2020) .....	18
Figure 2.7: XRD patterns for $\text{Co}_3\text{O}_4$ nanoparticles a) dried at $90^\circ\text{C}$ and 6 hours and b) calcined for a further 3 hours at $400^\circ\text{C}$ (taken from: Yarestani et al., 2014).....	19
Figure 2.8: Conversion rate of $\text{Co}_3\text{O}_4$ nanoparticles as a function of reaction temperature and residence time (adapted from Lester et al., 2012) .....	20

Figure 2.9: XRD patterns for cubic spinel $\text{Co}_3\text{O}_4$ particles synthesised at a) 0.03 M and reaction temperature: 200°C, 300°C and 430°C b) 215 °C using different precursor concentrations (taken from Lester et al., 2012) .....	20
Figure 2.10: An energy diagram that illustrates the oxidation process of CO to $\text{CO}_2$ , in gas phase, on the surface of the heterogeneous catalyst (taken from: Mielby., 2014) .....	24
Figure 2.11: Comparison between homogeneous, nano- and heterogeneous catalysts (taken from Singh & Tandon, 2014) .....	25
Figure 2.12: a) The dependence of the selectivity of the pyrrole hydrogenation on the particle size and b) The dependence of the selectivity of the pyrrole hydrogenation on the particle shape (taken from Yimin & Somorjar, 2010).....	26
Figure 2.13: Chemical structure of Azo dyes (taken from Ghaly et al., 2014) .....	27
Figure 2.14: Treatment techniques for the treatment of textile wastewater (adapted from Punzi, 2015) .....	29
Figure 2.15: Classification of advance oxidation processes (adapted from Mayyahi & Al Asadi, 2018) .....	32
Figure 2.16: Cobalt-mediated activation of Oxone (taken from Anipsitakis et al., 2005) .....	34
Figure 2.17: 2,4-DCP transformation with $\text{Co}_3\text{O}_4$ / Oxone <sup>®</sup> and homogeneous Co / Oxone <sup>®</sup> at acidic pH (taken from Anipsitakis et al., 2005).....	36
Figure 2.18: 2,4-DCP transformation with $\text{Co}_3\text{O}_4$ / Oxone <sup>®</sup> and homogeneous Co/ Oxone <sup>®</sup> at neutral pH (taken from Anipsitakis et al., 2005).....	36
Figure 2.19: Flow diagram for the CCD method (taken from Asghar et al., 2014).....	38
Figure 2.20: The diffraction in terms of reflection of an incident wave redrawn as described by Bragg's law (Williams & Carter, 1996).....	41
Figure 3.1: Preparation of the cobalt salt precursor.....	47
Figure 3.2: 200 mL pressure vessel inside oven .....	47
Figure 3.3: Multipurpose X-ray diffractometer D8-Advance (photo provided by Dr R. Bucher) .....	49
Figure 4.1: XRD patterns results for $\text{Co}_3\text{O}_4$ nanoparticles produced by a) cobalt acetate tetrahydrate, b) cobalt chloride hexahydrate and c) cobalt nitrate hexahydrate precursors .	58
Figure 4.2: Normal plot of residuals.....	60
Figure 4.3:The crystallite size as a response of the interaction between residence time and precursor concentration at a reaction temperature of 90°C .....	73
Figure 4.4: The crystallite size as a response of the interaction between residence time and precursor concentration at a reaction temperature 180°C .....	74
Figure 4.5: Effect of the reaction temperature and precursor concentration interaction on product yield (a) low precursor concentration and (b) high precursor concentration .....	78

Figure 5.1: Degradation of the MO dye using $\text{Co}_3\text{O}_4$ derived by $\text{Co}(\text{C}_2\text{H}_3\text{O}_2)_2^-$ precursor.....	81
Figure 5.2: Degradation of the MO dye using $\text{Co}_3\text{O}_4$ derived by $\text{CoCl}_{12}\cdot 6\text{H}_2\text{O}$ - precursor ....	81
Figure 5.3: Degradation of the MO dye using $\text{Co}_3\text{O}_4$ derived by $\text{Co}(\text{NO}_3)_2\cdot 6\text{H}_2\text{O}$ - precursor	82
Figure 5.4 Degradation of MO using $\text{Co}(\text{NO}_3)_2\cdot 6\text{H}_2\text{O}$ -, $\text{CoCl}_{12}\cdot 6\text{H}_2\text{O}$ – and $\text{Co}(\text{C}_2\text{H}_3\text{O}_2)_2$ derived $\text{Co}_3\text{O}_4$ .....	90
Figure 6.1: Comparison of the synthesis cost of cobalt precursors.....	95
Figure 6.2: Comparison of production cost for different precursor salts at the highest produced yield .....	95
Figure 6.3: Comparison of the treatment cost .....	97
Figure 6.4: Comparison of treatment cost using different precursor salts .....	98

## List of tables

Table 2.1: Comparison of hydrothermal synthesis methods for the production of $\text{Co}_3\text{O}_4$ .....	22
Table 2.2: The oxidant potential of various oxidants (taken from Mayyahi & Al Asadi, 2018) .....	31
Table 2.3: Comparative results from the transformation of 2,4-DCP using different cobalt compounds (adapted from Anipsitakis et al., 2005).....	35
Table 3.1: Three level three factor experimental design .....	45
Table 3.2: Chemical quantity used .....	46
Table 4.1: Cobalt oxide nanoparticles produced by means of a cobalt salt precursor.....	52
Table 4.2: Analysis of variance table for product yield.....	60
Table 4.3: Analysis of variance table for crystallite size.....	62
Table 4.4: The product yield as a response of the interaction between residence time and precursor concentration at a reaction temperature of a) $90^\circ\text{C}$ , b) $135^\circ\text{C}$ and c) $180^\circ\text{C}$ . .....	64
Table 4.5: Operating parameters for maximum $\text{Co}(\text{OH})_2$ to $\text{Co}_3\text{O}_4$ production yield.....	68
Table 4.6: The crystallite size as a response of the interaction between precursor concentration and reaction temperature at a residence time a) 0.5 hours, b) 3.25 hours and c) 6 hours.....	70
Table 4.7: Operating parameters for minimum $\text{Co}_3\text{O}_4$ crystallite size .....	74
Table 4.8: Operating parameters for maximum $\text{Co}_3\text{O}_4$ crystallite size .....	75
Table 5.1: Analysis of variance table for degradation .....	83
Table 5.2: The degradation as a response of the interaction between residence time and precursor concentration at a reaction temperature of a) $90^\circ\text{C}$ b) $135^\circ\text{C}$ and c) $180^\circ\text{C}$ .....	85
Table 5.3: Operating parameters for minimum degradation of methyl orange .....	87
Table 5.4: Operating parameters for maximum degradation of methyl orange .....	88
Table 5.5: Degradation percentage vs crystallite size.....	88

Table 5.6: Degradation percentage vs the surface area of the best and worst $\text{Co}_3\text{O}_4$ nanocatalyst.....	89
Table 6.1: Chemical product cost.....	92
Table 6.2: Production and treatment cost of $\text{Co}_3\text{O}_4$ nanocatalyst .....	93
Table 6.3: Process conditions for highest yield producing samples for synthesis cost.....	95
Table 6.4: Process conditions for the best performing samples and the samples that had the lowest treatment cost .....	97
Table 7.1: Range of $\text{Co}_3\text{O}_4$ yield produced and optimal operating parameters .....	101
Table 7.2: Effect of operating parameters on $\text{Co}_3\text{O}_4$ product yield .....	101
Table 7.3: Crystallite sizes of $\text{Co}_3\text{O}_4$ nanoparticles .....	102
Table 7.4: Operating parameters for maximum degradation of MO solution and surface area of best performing $\text{Co}_3\text{O}_4$ nanoparticles.....	103
Table A.1: Safety precautions on materials and equipment used. ....	115

## Terminologies

Cobalt(III)oxide	Formula: $\text{Co}_3\text{O}_4$ . Cobaltoxide is an inorganic compound with magnetic properties that makes it extremely feasible for applications such as: heterogenous catalyst, biomedical applications etc.
Hydrothermal synthesis	Hydrothermal synthesis is defined as the process that utilises single or heterogenous reactions in order to promote crystal growth under conditions of elevated pressure and temperature.
Nanomaterials	Nanomaterials are defined as any material that has an average particle size between 1 nm and 100 nm.
Nanotechnology	Nanotechnology is the characterisation, design, production and application of nanostructures, devices and systems by controlling the size and shape of these structures.

## List of abbreviations

- MO:** Methyl orange solution
- AOP:** Advanced Oxidation Processes
- ANOVA:** Analysis of variance
- PMS:** Peroxymonosulfate
- BET:** Brunauer–Emmett–Teller
- XRD:** X-ray Diffraction
- JCPDS:** Joint Committee on Powder Diffraction Standards

# Chapter 1 Introduction

## 1.1. Background and Motivation

Nanotechnology has been described as a broad field with connections to almost all disciplines that still have room for development and improvement (Roco, 2001). Nanostructured materials have potential applications in the fields of technology, science and engineering (Almeida, 2010). In 2011 the global market for nanotechnology was valued at \$201.1 billion. In 2009 a revenue of \$9 billion was achieved and was expected to rise to \$37.3 billion by the end of 2017 (McWilliams, 2010). Consequently, in recent years the synthesis, characterisation and application of nanomaterials have been widely investigated (Almeida, 2010).

The reason for interest in metal and metal oxide nanoparticles is their interesting properties in ceramic, optical and catalytic fields (Kawai-Nakamura et al., 2008). The application of nanoparticles in magnetic recording media, biomedical technology, energy and ferrofluids requires particles with well-defined size distribution, composition and magnetic properties (Hao & Teja, 2003). Salavati-Niasari et al. (2009) stated that metal oxide nanoparticles are excellent candidates for electronic and optoelectronic applications due to their unique and diverse physical and chemical properties. Byrappa et al. (2008) and Hao and Teja (2003) reported that the large-scale production of nanoparticles of controlled shape and size is still a major challenge.

Cobalt oxide is a transitional metal oxide that occurs in five different oxidation states: CoO, CoO(OH), CoO<sub>2</sub>, Co<sub>2</sub>O<sub>3</sub>, and Co<sub>3</sub>O<sub>4</sub>. It has been found that cobalt(III) oxide (Co<sub>3</sub>O<sub>4</sub>) exhibits mixed oxidational states (Co<sup>2+</sup> and Co<sup>3+</sup>) and that it has a regular cubic structure with tetrahedral sites (8a) that are occupied by Co<sup>2+</sup> ions and octahedral sites (16d) that are occupied by Co<sup>3+</sup> ions (Anipsitakis & Dionysiou, 2004). Man et al. (2011) stated that cobalt(II) oxide (Co<sub>2</sub>O<sub>3</sub>) and cobalt(III) oxide (Co<sub>3</sub>O<sub>4</sub>) are considered as important p-type semiconductors, which belong to spinel structure based on cubic close packing array of oxide ions. Spinel cobalt oxide nanostructured materials have been investigated by several inorganic chemists due to its wide variety of applications such as cobalt catalyst for the treatment of textile wastewater, anode materials in lithium rechargeable batteries, semiconductors, energy storage, solid state sensors and magnetic materials (Anipsitakis & Dionysiou, 2004; Li et al., 2005; Poizot et al., 2000). According to Nassar and Ahmed (2011), the size and morphology is strongly affected by the properties of the nanostructures. Several novel synthetic methods have been developed to create nanostructured Co<sub>3</sub>O<sub>4</sub> with different morphologies such as nanowires, nanotubes, nanorods, nanowalls, nanoplatelets, flower-like nanomaterials, nanofibers, hollow sphere nanomaterials, etc. Several methods have been

applied for the synthesis of  $\text{Co}_3\text{O}_4$  nanomaterials, such as heat decomposition processes, coprecipitation, reflux processes, and sol-gel synthesis (Jolivet et al., 1997; López Pérez et al., 1997; Albuquerque et al., 1999). The hydrothermal route for the synthesis of cobalt (III) oxide nanoparticles is considered as an appropriate and efficient approach due to the low cost, simplicity and multiplicate morphologies of the products.

Various strategies have been implemented to remove colours from wastewater in order to diminish its effect on the environment (Deng & Zhao, 2015). The coloured wastewater displays ecotoxic risks such as diminishing oxygen levels in water, influencing photosynthetic forms of sea-going plants and in critical cases the suffocation of sea-going vegetation and fauna. This is due to the poisonous nature of the dyestuff and azo colours that diminish light entrance photosynthesis. Methods for the purification of the produced wastewater include photocatalyst, adsorption, oxidation, coagulation, filtration and biological treatment (Mathew & Shetty, 2017). Advanced oxidation processes (AOPs) involve the generation of sulphate radicals by using different oxidants that ultimately destroy components that are not removed under conventional treatment processes. Oxidation strategies or progressed oxidation forms (AOP) have become a popular removal technology (Deng & Zhao, 2015). Oxidisers that are used for these processes include ultraviolet light, fenton, ozone,  $\text{TiO}_2$  and hydrogen peroxide. One of the main advantages of advanced oxidation processes are that they are considered to be low or non-waste generation technologies that are able to terminate complex structures using short-lived chemical species that have high oxidation power. An efficient way to produce reactive sulphate radicals is by coupling a cobalt-based catalyst with peroxymonosulfate (PMS).

Deng & Zhao (2015) stated that effect of the operating parameters, their interactions as well as the type of precursor salt used on the product yield needs to be studied further in order to understand effect of the interactions between the process parameters on  $\text{Co}_3\text{O}_4$  nanoparticles produced by various cobalt precursors. Control of the nanoparticle morphology and an understanding of how it effects the catalytic ability in an AOP during the degradation of wastewater will enable us to economically scale up the process (Mathew & Shetty, 2017).

## 1.2. Statement of the research problem

There is a need for perfectly controlled nanocobalt oxide structures. Firstly, there is a lack of understanding of the effect of synthesis operating conditions and their interactions on  $\text{Co}_3\text{O}_4$  nanoparticles, produced using different cobalt precursors. Secondly, the efficiency of the produced nanocatalyst needs to be evaluated in order to determine if there is a relationship between the produced yield, crystallite size and the degradation percentage. By establishing this, the potential of upscaling the process can be assessed.

## 1.3. Aims and objectives

The aim of this work was to determine the optimal conditions for maximum yield of nano  $\text{Co}_3\text{O}_4$  nanoparticles by means of the hydrothermal synthesis and its efficiency in the degradation of synthetic textile wastewater. The specific objectives are:

- To evaluate the effect of different precursor counter ions on the particle characteristics.
- To evaluate the effect of reaction temperature, residence time and precursor concentration and their interactions on the crystallite size and  $\text{Co}_3\text{O}_4$  yield.
- To evaluate the degradation percentage of methyl orange (MO) solution by using a  $\text{Co}_3\text{O}_4$  nanocatalyst mediated AOP.
- To evaluate the cost efficiency of the production of the nanocatalyst and the treatment cost using the produced catalyst.

## 1.4. Significance

This study contributes to an understanding of the effect of process parameters and counter ions on the yield and crystallite size of  $\text{Co}_3\text{O}_4$  nanoparticles. An understanding of the relationship between the produced yield and degradation potential using the  $\text{Co}_3\text{O}_4$  nanocatalyst provides an indication the viability of upscaling the process.

## 1.5. Delineation

During the evaluation of the efficiency of the  $\text{Co}_3\text{O}_4$  produced catalyst in the degradation of MO solution, the concentration of MO, and the amount of catalyst and oxidiser were kept constant based on results found in literature studies. The efficiency of the  $\text{Co}_3\text{O}_4$  nanocatalyst were only evaluated on the degradation of synthetic MO dye solution prepared in a laboratory.

## 1.6. Thesis structure

### Chapter 1: Introduction

This chapter includes a background and motivation as well as the significance of the study that was conducted. It also presents the problem statement, research question, aims and objectives of the study and lastly the outline of the thesis.

### Chapter 2: Literature review

This chapter is an in-depth investigation of nanomaterials, classification of nanomaterials, the effect of size of nanostructures, toxicity of cobalt, growth mechanisms of one-dimensional nanomaterials, methods of synthesis, treatment of textile wastewater and characterisation techniques.

### Chapter 3: Experimental methodology

This chapter firstly provides an outline of the experimental set-up using Design-Expert<sup>®</sup> software. Secondly the hydrothermal synthesis for the production of cobalt hydroxide and calcination to cobalt(III)oxide is outlined. Further the evaluation processes of the catalytic efficiency of the produced nanocatalyst are discussed. Lastly the applied characterisation methods are discussed.

### Chapter 4: Results and discussion: Effect of the process conditions on the product yield and crystallite size

This chapter discusses the hydrothermal synthesis of  $\text{Co}_3\text{O}_4$  nanoparticles using three different types of cobalt salts (cobalt acetate tetrahydrate, cobalt chloride hexahydrate and cobalt nitrate hexahydrate), ammonium hydroxide and water as the solvent. The effect of the interaction between the operational process parameters on the product yield and crystallite size of the produced nanoparticles are analysed.

### Chapter 5: Results and discussion: Evaluation of synthesised $\text{Co}_3\text{O}_4$ nanoparticles during colour degradation

The aim of this chapter was to evaluate the synthesised  $\text{Co}_3\text{O}_4$  nanoparticles that were produced using  $\text{Co}(\text{C}_2\text{H}_3\text{O}_2)_2$ ,  $\text{CoC}_{12}\text{H}_2\text{O}$  and  $\text{Co}(\text{NO}_3)_2 \cdot 6\text{H}_2\text{O}$  precursor salts as a catalyst for the degradation of methyl orange dye.

**Chapter 6:** Chapter 6 Results and Discussion: Cost comparison analysis on the production cost of  $\text{Co}_3\text{O}_4$  via various precursors.

The purpose of this chapter is to evaluate the cost that is involved in the production of  $\text{Co}_3\text{O}_4$  nanocatalyst and the treatment of wastewater using the produced nanocatalyst.

**Chapter 7:** Conclusions and Recommendations

Conclusions are drawn and recommendations were made for future work.

## Chapter 2 Literature Review

### 2.1. Introduction

This chapter firstly reviews the properties of metal oxide nanoparticles and how the nanostructure affects the properties of the particle. Secondly, different synthesis methods are discussed. Studies done on hydrothermal synthesis of  $\text{Co}_3\text{O}_4$  are compared to establish the type of precursor salt used and how the crystallite size is affected. Lastly, the application of metal oxide nanostructures for the treatment of textile wastewater is discussed. In this chapter the properties of catalyst and nanocatalyst, types of textile wastewater treatment process and AOP processes using  $\text{Co}_3\text{O}_4$  nanocatalyst are discussed.

### 2.2. Metal oxide nanoparticles

Nanomaterials has been known to act as an effective bridge between molecular (or atomic) structures and bulk materials; this has attracted considerable attention to the synthesis and use of nanomaterials. According to Frenkel et al. (2001) materials in bulk will exhibit constant physical properties, despite their mass or size, whilst nanostructures illustrate unique size-dependent properties. A reduction in the size of the particle causes the dominance of the surface area at the lower end of the size limit.

The unique and tuneable properties of these particles such as magnetic, optical, electrical, optoelectrical, thermal, photochemical, catalytic, etc., have made them excellent candidates for technological applications. Applications include optical devices, fuel cells, infrared and solar absorbers, secondary battery materials, ceramics, solar cells, gas sensors and biosensor, pyroelectric, piezoelectric, alkaline and lithium-ion batteries, magnetic, actuators, super capacitors, lasers, waveguides and chemical sensors (Darr, 1999).

Considering the growth mechanisms of one-dimensional nanomaterials, Yadong and Alivisatos (2005) stated that the growth of nanostructures takes place in several stages. Nucleation is the process in which thermodynamically stable clusters are formed when the free atoms or ions in the solution come together. This occurs over a period of time, at a constant monomer concentration. The nucleation ends as soon as the monomer concentration falls (due to the depletion of the monomer supply as the surface growth of clusters begin) below the critical level of nucleation. A general analysis of the growth process is crucial to understand the synthesis of nanostructures. In general, the ratio of surface area to volume in nanostructures is quite high. The large available surface area causes the excess energy of

the surface to become a non-negligible percentage of the total energy. If a solution is not in thermodynamic equilibrium, it requires a mechanism that allows the formation of larger particles at the cost of smaller particles, thus reducing the surface energy. Mass transport or diffusion (referred to as the Ostwald ripening process) often controls the coarsening effects (Liu & Hu, 2020).

### **Cobalt oxide**

Cobalt is a naturally occurring transition element that has magnetic properties and makes up approximately 0.0025% of the weight of the earth's crust. Cobalt is known to be a component of more than seventy naturally occurring minerals including sulfides, arsenides and oxides. Cobalt occurs predominately in two oxidation states: +2 (Co(II)) and +3 (Co(III)) (Neale, 1990).

Cobalt compounds can either be organic or inorganic and that can either be water soluble or insoluble. Cobalt compounds that are water soluble dissolve outside the cells of the fluids for cellular uptake while the particles of poorly soluble cobalt compounds can be taken up intact by the cells of the fluid and can release ions within the cell (Neale, 1990). According to Lison (2015), cobalt nitrate, cobalt sulfate, cobalt acetate and cobalt chloride are soluble in water while cobalt sulfides, cobalt oxides (including  $\text{Co}_3\text{O}_4$  and mixed oxides) and cobalt hydroxides are insoluble or poorly soluble.

The synthesis of cobalt compounds became more popular in the beginning of this century which has led to a variety of applications and research on cobaltous catalysed reactions.  $\text{Co}_3\text{O}_4$  has been applied in the treatment of wastewater due to the thermodynamic stability that has been shown and the desirable catalytic properties such as high concentration of active sites, morphology-dependent properties and high surface to volume ratio (Warang et al., 2013).

### **Cobalt toxicity**

Cobalt and its compounds are extensively found in nature at generally low concentrations and has properties comparable to nickel and iron. Predominantly cobalt compounds occur in two valence states:  $\text{Co}^{2+}$  (cobaltous) and  $\text{Co}^{3+}$  (cobaltic). Cobalt plays a large part of numerous anthropogenic activities (Leyssens et al., 2017; Kim et al., 2006). According to Leyssens et al. (2017) the only known biological function of Co is its role as metal constituent of the  $\text{B}_{12}$  vitamin (cyanocobalamin), whereas it has been found that high and frequent exposure to other cobalt compounds is toxic to the human body and environment.

Although the size reduction of inorganic materials into nanoscale facilitates several properties and technological applications the increase in the surface area and reduction in the density of the nanostructures presents a risk to the ecological environment and human body compared to the bulk materials (Raman et al., 2016).

In unpopulated sites the atmospheric cobalt level is generally lower than 2 ng/m<sup>3</sup>. The earth's crust are reported to contain a cobalt level of approximately 25 mg/kg cobalt and the soil concentration ranges between 1 mg/kg to 40 mg/kg in the US (Leyssens et al., 2017; Kim et al., 2006). The concentration of cobalt in surface – and groundwater ranges between 1 µg/L to 10 µg/L in populated areas (Kim et al., 2006). The cobalt concentration in drinking water ranges between 0.1 µg/L to 5 µg/L. Contamination of air, soil and water by the means of cobalt and other metals typically occurs in areas near factories, mining sites and heavily industrialised cities (Leyssens et al., 2017). To protect the aquatic life in freshwater from acute toxic effects of cobalt it is recommended that the maximum concentration of cobalt should not exceed 110 µg/L. A maximum concentration of 4 µg/L is recommended to protect freshwater aquatic life from chronic toxic effects of cobalt (Nagpal, 2004). A study by Depgni (2020) used a permeable reactive barrier (PRB) containing 0.3 g of cobalt oxide catalyst in a one-step continuous water treatment reactor to treat textile dyeing effluent. Figure 2.1 illustrates the quantity of cobalt in the treated effluents at various dye concentrations of 2%, 4%, 6% and 8%. The PRB was reused for two cycles and the Oxone<sup>®</sup> concentration remained constant as 0.5 g/L. Due to the leaching of the cobalt catalyst during the treatment process, the residual amounts cobalt in the treated effluent increased. At the highest dye concentration, a residual amount of higher than 1.5 mg/L is present in the treated wastewater and would need further treatment if it was to be disposed into natural bodies of water. At the low dye concentrations, for repeated cycles the required limit was met. The objective of the work done by Depgni (2020) was to treat and reuse wastewater and not for disposal, and the work showed some success.

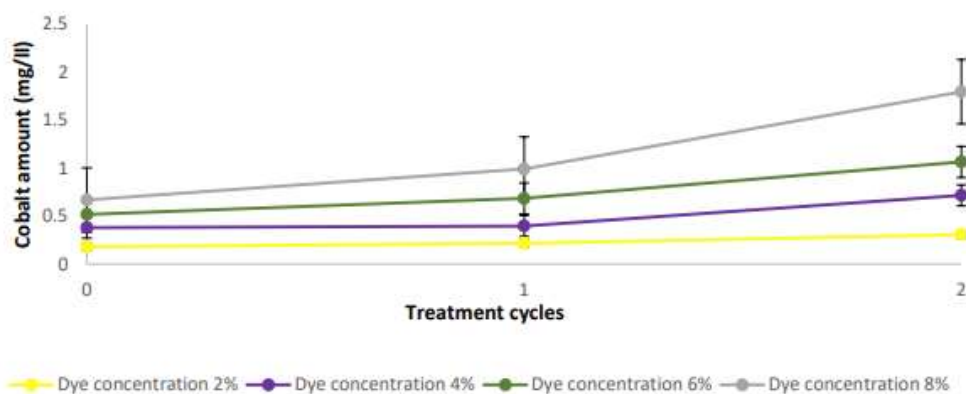


**Figure 2.1: Quantity of cobalt measured in treated wastewater (taken from Depgni, 2020)**

It has been found that frequent exposure to high concentrations of Co has been reported to result in respiratory effect, cardiac effects, immunological effects and congestion of kidneys, liver and conjunctiva (Kim et al., 2006; Leyssens et al., 2017). An exposure level of 0,005  $\mu\text{g}/\text{m}^3$  has led to chronic respiratory effects in mice and rats through inhalation. A tolerable inhalation concentration of  $1 \times 10^{-4} \text{ mg}/\text{m}^3$  was found based on lung function decrement. The ingesting of 150 mg/day of cobalt chloride, over a 22-day period, has resulted in polycythaemia and increased haemoglobin in humans (Kim et al., 2006). Raman et al. (2016) stated that the toxicity of cobalt nanostructures is not well understood and that the biological toxicity of Co is not primarily caused by the release of cobalt ions. Studies that evaluated the genotoxic potential of cobalt- based materials in vitro that made use of cell culture systems found that cobalt nanostructures are highly genotoxic and cytotoxic. It was found that in comparison with cobalt ions, cobalt nanostructures more readily enter the cells. Furthermore, it has been found that the toxicity of nanostructures is influenced by the particle size, morphology and surface characteristics as well as their interactions and interactions with other molecules in vitro (Raman et al., 2016). An assessment was carried out by the Industrial Chemicals Notification and Assessment Scheme (NICNAS) using the Inventory Multitiered Assessment and Prioritisation (IMAP) framework to assess the health and environmental impact of cobalt oxide. It was reported that inhaled particles of cobalt oxide particles are deposited in the respiratory tract. A study conducted in beagle dogs showed that the half-lives of cobalt (II) and cobalt (II, III) is reached in 6 – 80 days, while in rats the lungs were completely clear after 6 months. At a median lethal concentration lower than 5.06 mg/L the acute toxicity was low and no mortalities were found (IMAP Group., 2014).

## **2.3. Methods for synthesis of nanoparticles**

### **2.3.1. Introduction**

Synthesis of inorganic nanostructures is driven by the increasing array of applications that need particles at a reduced size. The properties of the nanostructures are highly dependent on morphology, material composition, crystallinity, purity, particle size, surface chemistry and surface area; these properties are largely determined by the synthesis method. Each synthesis method has its associated advantages and disadvantages; the target material or application determines the choice of the synthesis method. Gunn (2008) stated that nanostructures are mainly synthesised using the top-down or bottom-up method. The top-down method describes the formation of nanomaterials through the breakdown of their bulk counterparts until nanosize is achieved. The bottom-up method describes the formation of nanostructures from an atomic or molecular basis, using precursors; due to the control of the nanoparticle synthesis this method is preferred.

Synthesis methods are characterised in two categories: chemical synthesis methods and physical production methods. Chemical production methods or wet chemical synthesis methods include co-precipitation, micro-emulsion systems, sol-gel and hydrothermal synthesis. According to Gunn (2008), liquid phase methods tend to produce a high product yield and are relatively inexpensive in comparison with physical methods. One of the main advantages of wet phases systems is that the surface character, shape, size and composition of the particles can be controlled by tuning the nucleation and growth process (Teja & Koh, 2009). Physical synthesis methods include gas phase deposition methods and gas phase production (laser pyrolysis, aerosol preparation and plasma prepared nanoparticles) (Gunn, 2008; Teja & Koh, 2009). High quality nanoparticles have been produced by means of physical production methods. In comparison with wet chemical synthesis methods, the yield of the produced nanostructures was found to be low and the upscaling of the equipment for industrial manufacturing proved challenging (Gunn, 2008).

### **2.3.2. Solid State Reaction**

Zhang et al. (2012) stated that the solid stated reaction is a unique process in synthetic chemistry and has been successful in the synthesis of nanostructures. Simple metal oxides or carbonate precursors are mixed at a reaction temperature between 700°C and 1000°C, in air or gasses, over an extensive time period. This approach operates on the premise that pure products are produced due to the stability of the target material (ceramic) at high temperatures.

It is assumed that any contaminants will be unstable at the elevated temperatures and will decompose. It has been found that poor particle size distribution, large particles are generally produced, and there is poor particle morphology control; therefore, an alternative synthesis method is advised if particles with a controlled shape and size are required (Starkey, 2016).

### **2.3.3. Chemical and physical vapour phase reactions**

Thermochemical and physical synthetic techniques (such as chemical vapour deposition (CVD) and physical vapour deposition (PVD)) as well as other vapour phase methods (for example spray pyrolysis) are popular for the production of nanomaterials on an industrial scale due to their relative simplicity and low cost. However, it has high capital cost (Choy, 2003; Helmersson et al., 2006; Tjong & Chen, 2004). The droplets are produced by mixing the organometallic or salt solution compounds together with carrier gasses such as nitrogen. This mixture is then either sprayed onto a heated surface or a furnace at a temperature of about 1000°C which induces evaporation of the solvent. The products of the reaction of the metal-containing precursors are deposited onto the substrate (Starkey, 2016).

This process can be operated as a continuous process with the downside that the process is energy-intensive due to the high temperatures that is required. These techniques are largely used for the production of films and coatings such as CuInSe<sub>2</sub>/CdS heterojunction diodes and CdS thin films (Starkey, 2016; Ramaiah, 1999; Strifler & Bates, 1992).

### **2.3.4. Co-precipitation synthesis**

The precipitation of relative insoluble particles is achieved through the addition of an ion-containing solution under conditions of elevated temperatures or inert atmosphere and the presence of a base (Kumar, 2009). The co-precipitation synthesis method refers to the simultaneous occurrence of nucleation, growth and agglomeration processes (Cushing et al., 2004). Conditions of elevated temperature and pressure (supersaturated conditions) cause the primary step to be nucleation and promote growth of large quantities of small insoluble particles. The secondary processes, Ostwald ripening and agglomeration, largely affect the particle morphology, size and properties of the final obtained particles (Chaudhry, 2008). According to Cushing et al. (2004) the particle morphology, product size and particle size are influenced by the following reaction conditions: stirring rate, rate of reactant addition, concentration, temperature and mixing rate.

### **2.3.5. Micro-emulsion synthesis**

The micro-emulsion preparation method is used to synthesise organic and inorganic nanomaterials. This technique enables control of particle characteristics such as particle size, morphology, geometry, homogeneity and surface area (Cushing et al., 2004; Malik et al., 2010; Hu et al., 2009; Pileni, 2003). Emulsions consist of homogeneous mixtures of surfactants, oil and water. Surfactants exhibit a hydrophobic head and lipophilic tail, while oil is a simple long hydrocarbon chain (Chaudhry, 2008). The volume of water dispersed in the oil is described by the term “micro”. The water in emulsions has a large interfacial area causing the limitation of the particle flocculation and growth (Phillips et al., 2003). Low water levels are found in micro-emulsions and are transparent and stable for long periods of time. Particles are produced from a reaction between two water droplets containing reactants that collide and mix together. The small particle size and narrow particle size distribution is achieved due to the small reaction environment (droplet size) (Cushing et al., 2004).

### **2.3.6. Sol-gel synthesis**

The sol-gel process produces infinite-molecular-weight oxide polymers from homogeneous solution through a combination of a series of chemical reactions such as hydrolysis and condensation of alkoxide-based precursor (Chaudhry, 2008). According to Cushing et al. (2004) the sol-gel synthesis method can be described through a series of distinctive steps. The first step is the formation of the solution, or sol (a stable solution of metal or alkoxide precursor). The second step involves the formation of gelatine (gel) as a result of the alcohol or oxide network that is formed from a polyestriification or polycondensation reaction. This reaction rapidly increases the viscosity of the solution. The third step involves the transformation of the gel into a solid mass by means of the polycondensation reaction. This known as the aging step and can take several days. The fourth step is the removal of water and other volatile liquids, while the fifth step involves the removal of the M-OH groups through dehydration. These processes are done through calcination at temperatures up to 800°C. The final step is the densification and decomposition of the gels at temperatures higher than 800°C (Nolan, 2010). Hakuta et al. (1998) stated that the growth of the nanostructures is more easily achieved by using the sol-gel method. This is due the highly controllable environment in terms of the reaction time, pH, concentration, temperature and the rate of the addition of the reagent or precursor addition. They also stated that this method yields high homogenous samples with particle size and size distribution control; however post-synthesis heating steps are required due to the low purity and crystallinity of the products.

The sol-gel synthesis method poses the following advantages over other synthesis methods: stoichiometric control, ability to produce porous powders and thin coatings, high purity products and homogeneity (Nolan, 2010). This approach is more cost effective and is operated at lower temperatures that can control the chemical composition of the product (Starkey, 2016). On the other hand, the potential for the scale-up for this synthesis method is restricted by the controlled nature that the growth necessitates (prolonged reaction times and low concentrations) (Nolan, 2010).

### **2.3.7. Hot injection**

For the synthesis of quantum dot, hot injection routes are highly popular. Though the injection of the cool precursors into the solvents at boiling point in the presence of chelating agents (for example trioctylphosphine oxide, oleylamine and oleic acid) control over the composition, size and surface chemistry of the nanostructures can be achieved (Donega et al., 2005; Starkey, 2016). Homogeneous diffusion- controlled growth is observed throughout the solution once nucleation has occurred where smaller crystals grow faster than larger crystals. Ostwald ripening occurs as the growth of the crystals progresses where the smaller crystals dissolve as a result of their high chemical potential and the larger crystals continuous to grow. Saturation is the last growth stage and it is observed that up to this point the average particle size increases while the particle concentration decreases. By allowing a rapid nucleation separate from the growth stage a high level of control over the particle size is achieved (Carey et al., 2015).

### **2.3.8. Hydrothermal synthesis**

Traditionally the hydrothermal synthesis process for the production of metal oxides is carried out in an autoclave type reactor where the aqueous solution is heated to the desired temperature and then aged over a period of time (as seen in Figure 2.2). This process is mainly used for the production of highly crystalline inorganic particles, such as single or mixed metal oxides (Hayashi & Torii, 2003). The main advantage that the batch system has over a continuous system is that it is possible to control the oxidation stages of the elements. The batch reactor method is operated within a temperature range of 100°C – 200°C (Arai et al., 2002). The moderate temperatures at which the synthesis reactions take place allow the synthesis of metastable phases that are not accessible by other means. Although this method is operated under relatively mild conditions, in comparison with other ceramic methods, particles that are highly crystalline are obtained without the need of further heating steps (Starkey, 2016).

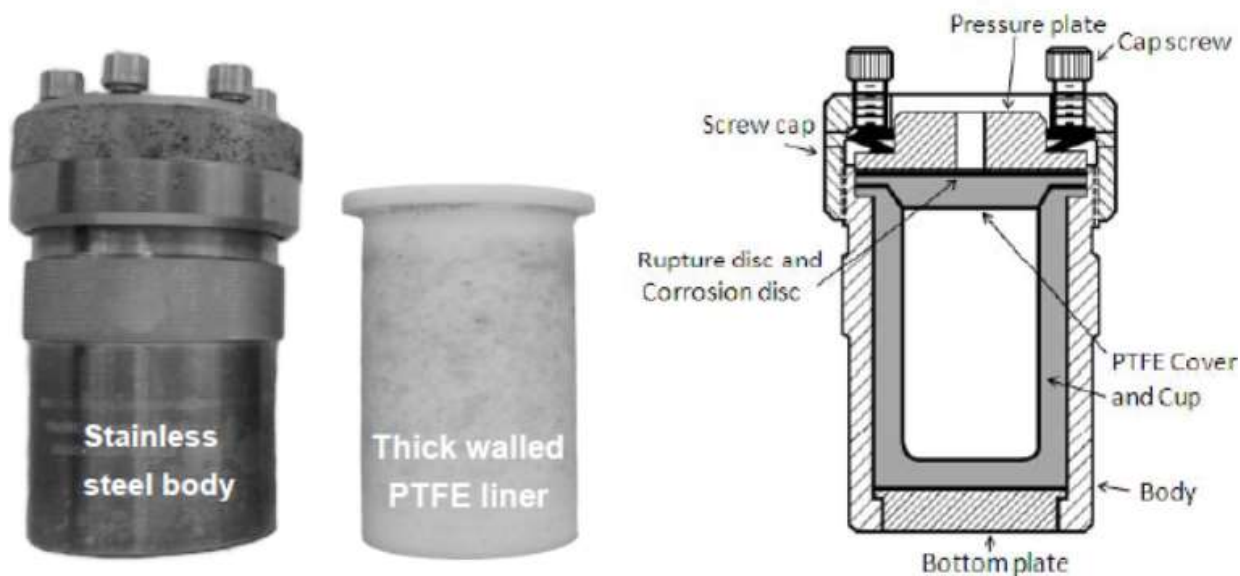
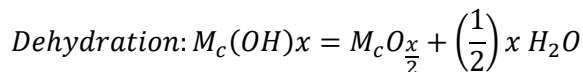
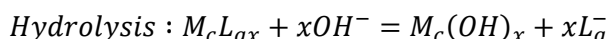


Figure 2.2: Photograph and schematic representation of a laboratory autoclave (taken from Zheng, 2009)

For the formation of metal oxides, hydrothermal synthesis is believed to involve two main reactions: hydrolysis and dehydration (Matson et al., 1996).



Where the metal cation is represented by  $M_c$  and the anion is represented by  $L_a$ . During the heating period of the precursor the production of the nuclei takes place and eventually crystals. During the hydrothermal reactions, homogeneous nucleation and grain growth processes take place, resulting in particles with the desired chemical and physical properties (Starkey, 2016).

#### Hydrothermal Synthesis of $Co(OH)_2$ , $CoCO_3$ and $Co_3O_4$

Synthesis of cobalt oxide by various hydrothermal methods along with the characteristics of the nanostructures has been investigated. Nassar (2013) synthesised  $CoCO_3$  and  $Co_3O_4$  nanoparticles by a surfactant-free hydrothermal method. During the hydrothermal synthesis process reaction temperatures were varied between 80°C and 160°C and residence time between 30 minutes and 24 hours. The precursor was made up of ammonium carbonate and cobalt acetate. It was found that at a molar ratio ( $Co^{2+}:CO_3^{2-}$ )  $\geq 1:3$  the hydrothermal synthesis reaction produces a pure phase of  $CoCO_3$ . Pink-coloured  $CoCO_3$  particles were collected.  $Co_3O_4$  nanoparticles were produced after thermal decomposition of  $CoCO_3$  at 300°C for 2 hours. Figure 2.3 shows the diffraction peaks of a)  $CoCO_3$  nanoparticles and b)  $Co_3O_4$

nanoparticles. The diffraction peaks as shown by the XRD pattern in Figure 2.3 a) can be indexed as pure phase  $\text{CoCO}_3$ , the standard patterns of cobalt carbonate according to the Joint Committee on Powder Diffraction Standards (JCPDS) card 42-1467 for  $\text{Co}_3\text{O}_4$ . The XRD pattern diffraction peaks analysis of  $19.0^\circ$  (111),  $31.3^\circ$  (220),  $36.9^\circ$  (311),  $44.8^\circ$  (400),  $59.4^\circ$  (511), and  $65.2^\circ$  (440) indicated that after calcination as seen in Figure 2.3 b) a pure cubic  $\text{Co}_3\text{O}_4$  was produced. From the XRD the crystallite size was determined to be an average of 25 nm using the Debye-Scherrer equation (Equation 2-1), where  $k = 0.9$ ,  $\lambda$  is the wavelength of the X-ray radiation and  $\beta$  is the full width at half of the diffraction peak.

$$D = (k\lambda)/(\beta\cos\beta\theta) \quad \text{Equation 2-1}$$

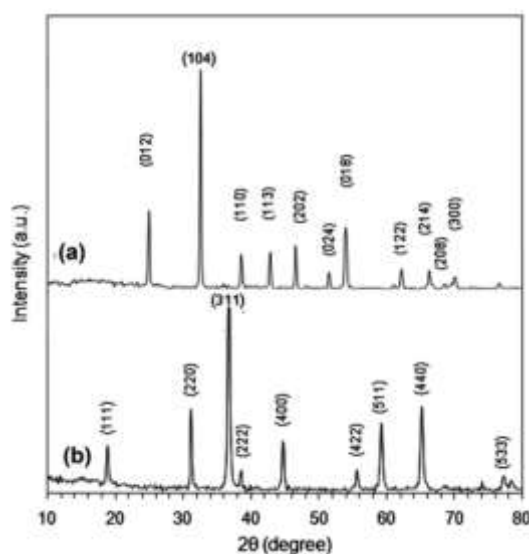


**Figure 2.3: XRD patterns of (a)  $\text{CoCO}_3$  nanoparticles and (b)  $\text{Co}_3\text{O}_4$  nanoparticles (taken from Nassar, 2013)**

Nassar and Ahmed (2012) synthesised  $\text{CoCO}_3$  nanoparticles by the hydrothermal method of different cobalt salts (cobalt chloride ( $\text{CoCl}_2 \cdot 6\text{H}_2\text{O}$ ), cobalt nitrate ( $\text{Co}(\text{NO}_3)_2 \cdot 4\text{H}_2\text{O}$ ) and cobalt sulfate ( $\text{CoSO}_4 \cdot (\text{H}_2\text{O})_7$ ) and ammonium carbonate. A 1:3 molar ratio of  $[\text{Co}^{2+}]:[\text{CO}_3^{2-}]$  was used. The reaction temperature was at  $120^\circ\text{C}$  and the residence time was at 30 minutes. After the reaction was completed, pink solid products of cobalt carbonates ( $\text{CoCO}_3$ ) were collected.  $\text{Co}_3\text{O}_4$  nanoparticles were produced after thermal decomposition of  $\text{CoCO}_3$  at  $500^\circ\text{C}$  for 3 hours. The XRD patterns for the crystal phases of the  $\text{CoCO}_3$  samples prepared by using the different counter ions were found to be similar to that of Nassar (2013) and shown in Figure 2.3 a). It was found that the average particle size increased from 21.8 nm to 29.8 nm by changing the counter ion from sulfate to nitrate. The difference in the particle size for the different precursor salts can be attributed to the fact that  $\text{SO}_4^{2-}$  ions are more negatively charged than the chloride and nitrate ions. The rate of the particle growth is hindered by the

high electrostatic repulsion between the sulfates and carbonate ions. The similar average particle size of the chloride and nitrate ions is attributed to the equality of the negative charge of the two anions. The XRD patterns for all three precursor salts shows that the diffraction peaks are assigned to pure cubic phase of  $\text{Co}_3\text{O}_4$  and no impurity peaks were detected. The diffraction peaks as shown by the XRD pattern had similar peaks to that of Nassar (2013) shown in Figure 2.3 b). The average particle size of the produced  $\text{Co}_3\text{O}_4$  nanoparticles were estimated to be 42.3 nm, 47.35 nm and 30.5 nm for cobalt sulfate, cobalt chloride and cobalt nitrate respectively. The TEM results showed that  $\text{Co}_3\text{O}_4$  nanoparticles derived from cobalt sulfate had a sheet like shape, cobalt chloride derived  $\text{Co}_3\text{O}_4$  nanoparticles had a hexagon shape and cobalt nitrate derived  $\text{Co}_3\text{O}_4$  nanoparticles had a square shape.

Nassar and Ahmed (2011) synthesised  $\text{CoCO}_3$  and  $\text{Co}_3\text{O}_4$  crystalline nanoparticles by the hydrothermal method of different cobalt salts (cobalt acetate ( $\text{Co}(\text{CH}_3\text{COO})_2 \cdot 4\text{H}_2\text{O}$ ), cobalt chloride ( $\text{CoCl}_2 \cdot 6\text{H}_2\text{O}$ ), cobalt nitrate ( $\text{Co}(\text{NO}_3)_2 \cdot 4\text{H}_2\text{O}$ ) and urea. The reaction temperature was at  $160^\circ\text{C}$  and the residence time was varied between 3 hours and 72 hours. After the reaction was completed, pink solid products of cobalt carbonates ( $\text{CoCO}_3$ ) were collected.  $\text{Co}_3\text{O}_4$  nanoparticles were produced after thermal decomposition of  $\text{CoCO}_3$  at  $500^\circ\text{C}$  for 3 hours. The XRD patterns for the crystal phases of the  $\text{CoCO}_3$  samples prepared by using the different counter ions were found to be similar to that of Nassar (2013) and shown in Figure 2.3 a). The intensities of the diffraction peaks indicated that the obtained  $\text{CoCO}_3$  samples had good crystallinity. The diffraction peaks in the XRD patterns could be indexed as a pure hexagonal phase of  $\text{CoCO}_3$  and no other impurity peaks were detected. Figure 2.4 shows the SEM images of the morphologies of the prepared  $\text{CoCO}_3$  samples produced by the different counter ions. It was found that the  $\text{CoCO}_3$  crystals produced by cobalt acetate (Figure 2.4 a) and cobalt nitrate (Figure 2.4 c) were uniform while cobalt chloride produced  $\text{CoCO}_3$  crystals (Figure 2.4 b) had a different morphology.

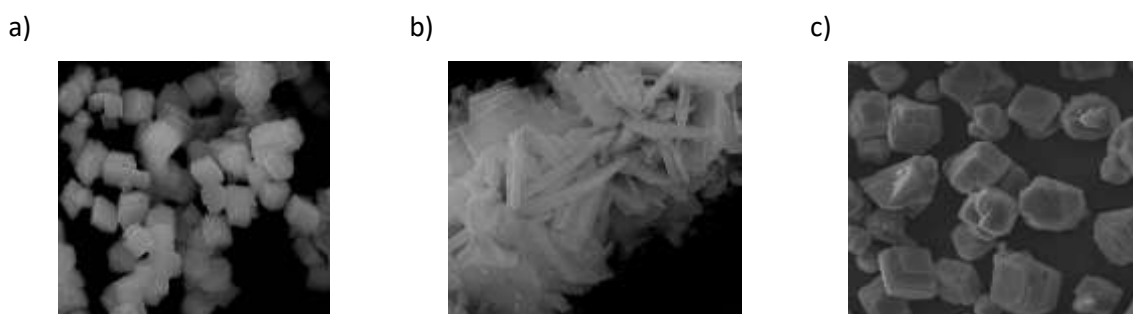


**Figure 2.4: SEM images of  $\text{CoCO}_3$  nanoparticles produced by a) cobalt acetate, b) cobalt chloride and c) cobalt nitrate (taken from Nassar and Ahmed, 2011)**

The diffraction peaks as shown by the XRD pattern had similar peaks to that of Nassar (2013) shown in Figure 2.3 b). This shows that cubic phase  $\text{Co}_3\text{O}_4$  was produced according to the JCPDS card no. 42-1467 with no other peaks for impurities detected. The Debye-Scherrer equation (Equation 2-1) was used to estimate the average crystallite size of the produced  $\text{Co}_3\text{O}_4$  nanoparticles and found that it was 39.0 nm for cobalt acetate, 31.8 nm for cobalt chloride and 30.1 nm for cobalt nitrate.

The effects of cobalt chloride hexahydrate and cobalt nitrate hexahydrate on  $\text{Co}_3\text{O}_4$  nanoparticles were investigated by Heuvel (2020) using the hydrothermal synthesis process. It was found that the cobalt hydroxide powders that were obtained from the cobalt chloride hexahydrate and cobalt nitrate hexahydrate precursors produced  $\alpha$ -phased  $\text{Co}(\text{OH})_2$ . Cobalt hydroxide exists as one of two polymorphs – alpha cobalt hydroxide ( $\alpha\text{-Co}(\text{OH})_2$ ) and beta cobalt hydroxide ( $\beta\text{-Co}(\text{OH})_2$ ), which is a widely used precursor for cobalt(III) oxide ( $\text{Co}_3\text{O}_4$ ). Al-Ghoul et al. (2010) stated that the green-blue colour exhibited by the  $\alpha\text{-Co}(\text{OH})_2$  is due to the octahedral coordinated Co(II) and tetrahedral orientation of hydroxyl and intercalated anions bonded to Co(II). The pink colour of  $\beta\text{-Co}(\text{OH})_2$  is due to the octahedral symmetry of the particles. The  $\alpha$ -phased  $\text{Co}(\text{OH})_2$  was identified by an XRD pattern showing the characteristic peak (003). Figure 2.5 shows the XRD patterns for a)  $\alpha\text{-Co}(\text{OH})_2$  and b)  $\beta\text{-Co}(\text{OH})_2$ .

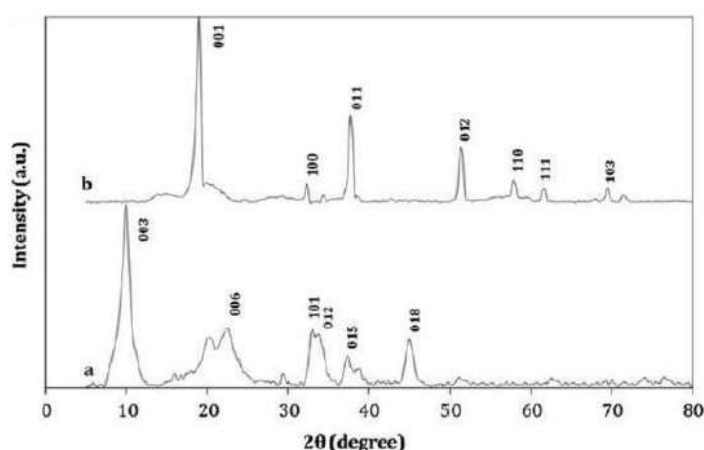
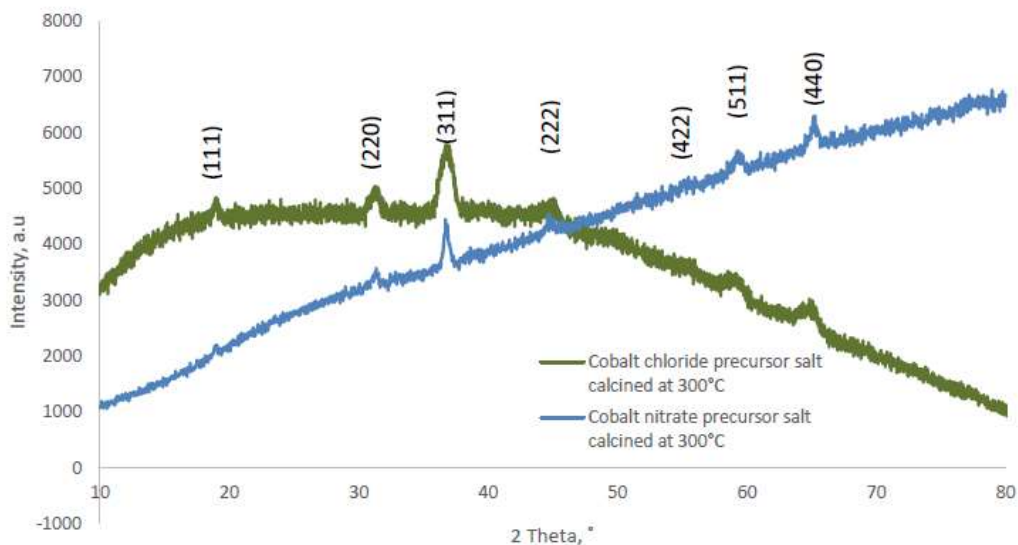


Figure 2.5: XRD patterns for a)  $\alpha\text{-Co}(\text{OH})_2$  and b)  $\beta\text{-Co}(\text{OH})_2$  (taken from Al-Ghoul et al., 2010).

The XRD patterns for  $\text{Co}_3\text{O}_4$  calcined at  $300^\circ\text{C}$  can be seen in Figure 2.6. From this it was observed that the peaks represented are in agreement with the JCPDS card 42-1467 and  $\text{Co}_3\text{O}_4$  with a high purity level were produced.  $\text{Co}_3\text{O}_4$  produced from  $\alpha\text{-Co}(\text{OH})_2$  was shown not to have diffraction peaks analysis of  $44.8^\circ$  (400) and  $77^\circ$  (533), as was the case for  $\text{CoCO}_3$  derived  $\text{Co}_3\text{O}_4$  produced by Nassar and Ahmed (2011).



**Figure 2.6: XRD patterns for the  $\text{Co}_3\text{O}_4$  nanoparticles produced with cobalt chloride hexahydrate and cobalt nitrate hexahydrate precursors (taken from Heuvel, 2020)**

During this study it was found that an increasing the calcination temperature from  $300^\circ\text{C}$  to  $500^\circ\text{C}$  there was an increase in the crystallite size. For the cobalt chloride hexahydrate precursor, the crystallite size increased from 7.09 nm to 34.89 nm while the cobalt nitrate hexahydrate crystallite size increased from 17.08 nm to 27.91 nm.

Yarestani et al. (2014) used the hydrothermal synthesis method to prepare  $\text{Co}_3\text{O}_4$  nanoparticles. A precursor mixture of cobalt chloride, Triton X-100 (a non-ionic surfactant) and KOH were prepared which resulted in a dark green colour. The Teflon-lined autoclave had a reaction temperature of  $180^\circ\text{C}$  and residence time of 6 hours. The obtained dark precipitant particles were first dried at  $90^\circ\text{C}$  for 6 hours and then further calcined for 3 hours at  $400^\circ\text{C}$ . The XRD characterisation of the produced  $\text{Co}_3\text{O}_4$  nanoparticle can be found in Figure 2.3 b). Figure 2.7 showed that the slight differences between the two XRD patterns are due to sample b (further calcined for 3 hours at  $400^\circ\text{C}$ ) which is a mixture of  $\text{Co}_3\text{O}_4$  and CoO phases. Using the Debye-Scherrer equation it was found that sample (a) had a crystallite size of 26.6 nm and sample (b) a crystallite size of 21.3 nm.

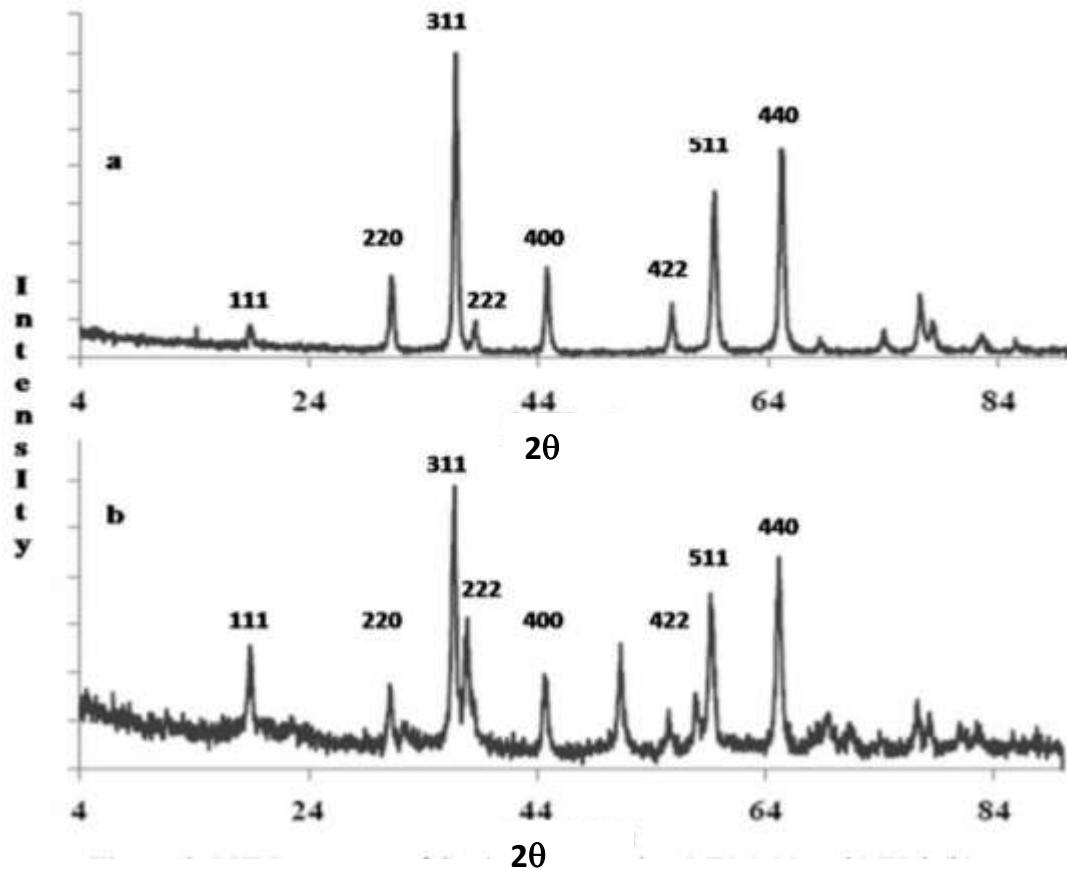
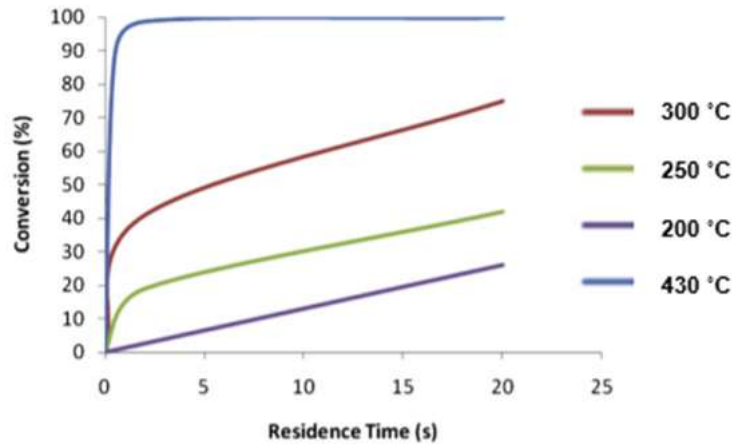


Figure 2.7: XRD patterns for  $\text{Co}_3\text{O}_4$  nanoparticles a) dried at  $90^\circ\text{C}$  and 6 hours and b) calcined for a further 3 hours at  $400^\circ\text{C}$  (taken from: Yarestani et al., 2014)

Lester et al. (2012) produced  $\text{Co}_3\text{O}_4$  nanoparticles by a controlled continuous hydrothermal synthesis process using an aqueous cobalt acetate precursor. The process parameters were varied as follows: residence time between 5 seconds and 25 seconds, reaction temperature between  $200^\circ\text{C}$  to  $430^\circ\text{C}$  and precursor concentration from 0.01 M to 0.05 M. Figure 2.8 shows that the conversion of cobalt acetate tetrahydrate to  $\text{Co}_3\text{O}_4$  nanoparticles increased as the reaction temperature increased from  $200^\circ\text{C}$  to  $430^\circ\text{C}$ . It was found that the influence of the residence time was less significant at higher temperatures.



**Figure 2.8: Conversion rate of  $\text{Co}_3\text{O}_4$  nanoparticles as a function of reaction temperature and residence time (adapted from Lester *et al.*, 2012)**

Figure 2.9 a) shows the XRD diffraction patterns of the cubic spinel  $\text{Co}_3\text{O}_4$  nanoparticles synthesised at 200 °C, 300 °C and 430 °C with a constant precursor concentration of 0.03 M. The cubic spinel  $\text{Co}_3\text{O}_4$  nanoparticle crystal structure is confirmed by the standard JCPDS card 42 - 1467, aligning with the findings in Figure 2.3 b), with no impurities showing. It was observed that the intensity of the peak increased as the reaction temperature increased thus showing a clear increase in crystallinity as the reaction temperature increased. Between a reaction temperature range of 200 °C and 430 °C a particle size distribution between 4 nm and 60 nm were obtained respectively dependant on the reaction conditions.

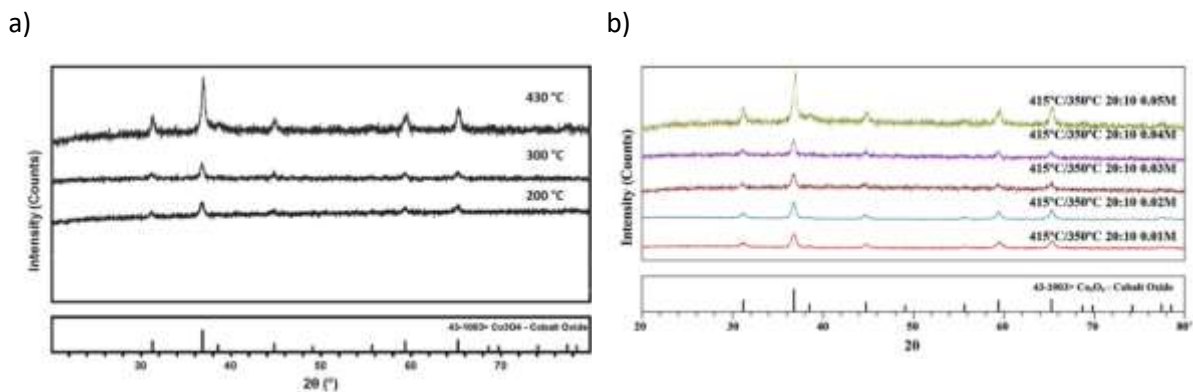


**Figure 2.9: XRD patterns for cubic spinel  $\text{Co}_3\text{O}_4$  particles synthesised at a) 0.03 M and reaction temperature: 200 °C, 300 °C and 430 °C b) 215 °C using different precursor concentrations (taken from Lester *et al.*, 2012)**

Figure 2.9 b) shows the XRD diffraction patterns of the cubic spinel  $\text{Co}_3\text{O}_4$  nanoparticles synthesised at a precursor concentration between 0.01 M and 0.05 M at a constant temperature of 415 °C. It was found that the largest particle sizes were found at the lowest precursor concentrations. Lester *et al.* (2012) stated that this result can be explained by higher

nucleation rates at elevated temperatures or a change in particle kinetics where nucleation kinetics are dominated by growth kinetics dominate, for example larger nanostructures are only obtained when insufficient concentrations of the precursor ions are available to form a new particle. Another possible explanation is that higher nucleation rates result in the production of more particles with a smaller initial size, and the growth phase is paused prematurely by the reduction of precursor solution (due to the high conversion rate at elevated reaction temperatures) thus implying that the fluid runs out of metal ions before the smaller nanoparticles can grow.

It has been shown that  $\text{Co}_3\text{O}_4$  nanoparticles can be successfully produced by a hydrothermal synthesis using various precursor solution and process conditions. Table 2.1 shows that the crystallite size is affected by the precursor solution, precursor concentration, reaction temperature, residence time and calcination conditions. It is observed that at higher calcination temperatures the crystallite size is larger.

**Table 2.1: Comparison of hydrothermal synthesis methods for the production of Co<sub>3</sub>O<sub>4</sub>**

Reference	Nassar (2013)	Nassar and Ahmed (2011)	Nassar and Ahmed (2011)	Heuvel (2020)	Yarestani et al. (2014)	Lester et al. (2012)
<b>Synthesis method</b>	Hydrothermal synthesis	Hydrothermal synthesis	Hydrothermal synthesis	Hydrothermal synthesis	Hydrothermal synthesis	Continuous hydrothermal synthesis
<b>Hydroxide/ carbonate</b>	CoCO <sub>3</sub>	CoCO <sub>3</sub>	CoCO <sub>3</sub>	α-Co(OH) <sub>2</sub>	α-Co(OH) <sub>2</sub>	Co(OH) <sub>2</sub>
<b>Precursor material</b>	- Cobalt acetate tetrahydrate	-Cobalt sulfate hexahydrate -Cobalt chloride hexahydrate -Cobalt nitrate hexahydrate	-Cobalt acetate tetrahydrate -Cobalt chloride hexahydrate -Cobalt nitrate hexahydrate	-Cobalt chloride hexahydrate -Cobalt nitrate hexahydrate	-Cobalt chloride hexahydrate	-Cobalt acetate tetrahydrate
<b>Process conditions</b>	-Reaction temperature: 80°C - 160°C -Precursor concentration: 3.22 mmol -Residence time: 0.5 hours - 24 hours -Calcination: 300°C for 2 hours	-Reaction temperature: 120°C -Precursor concentration: 3.22 mmol -Residence time: 30 minutes -Calcination: 500°C for 3 hours	-Reaction temperature: 160°C -Precursor concentration: 2.5 mmol -Residence time: 3 hours - 72 hours -Calcination: 500°C for 3 hours	-Reaction temperature: 105°C -Residence time: 6 hours -Precursor concentration: 0.23 M -Calcination: 300°C - 500°C for 3 hours	-Reaction temperature: 180°C -Residence time: 6 hours -Calcination: 400°C for 3 hours	-Reaction temperature: 200°C - 430°C -Precursor concentration: 0.01 M – 0.05 M -Residence time: 5 - 25 seconds
<b>Crystallite size</b>	25 nm	-Cobalt sulfate hexahydrate: 42.30 nm -Cobalt chloride hexahydrate: 47.35 nm -Cobalt nitrate hexahydrate: 30.50 nm	-Cobalt acetate tetrahydrate: 39.0 nm -Cobalt chloride hexahydrate: 31.8 nm -Cobalt nitrate hexahydrate: 30.1 nm	-Cobalt chloride hexahydrate: 7.09 nm – 34.89 nm -Cobalt nitrate hexahydrate: 17.08 nm - 27.91 nm	21.3 nm	4 nm – 60 nm

## 2.4. Application of metal oxide nanostructures as catalysts for the treatment of textile wastewater

### 2.4.1. Catalyst

Chorkendorff and Niemantsverdriet (2003) stated that catalytic processes play a critical role in chemical process and lie at the heart of countless chemical processes, from research done for academic purposes in small scale laboratories to industrial level. A variety of products that are essential for human society, such as fibres, fuels (including fossil fuels and alternative energy resources), medicines, energy conversion (for instance for fuel cells and water-splitting) polymers, paints, food production (for example to make hydrogenate oils or fertilisers), fine chemicals or bulk chemical production and pollution control (applied in water purification and flue-gas cleaning) would not be feasible in the absence of a catalyst (Masterton et al., 2012).

A catalyst is defined as a substance that increases the reaction rate without being consumed in the process. The catalyst offers an alternative reaction pathway that requires a lower energy to reach the transition state of the rate-limiting step, thus resulting in an increased rate of reaction (Mielby, 2014). Catalysts can either be homogeneous or heterogeneous. A homogeneous catalyst refers to a catalyst that operates in the same phase as the reactants (Chorkendorff and Niemantsverdriet, 2003). A heterogeneous catalyst refers to the form of the applied catalyst where the reactant and the catalyst exist in different physical phases. Generally, the heterogeneous catalyst is in a solid phase while the reactants are in liquid or gas phase. It has been stated that heterogeneous catalysts promote reactions that take place on the surface-active sites (Perry & Green, 1999). For example, Figure 2.10 illustrates the reduction in the activation energy ( $E_a$ ) if the oxidation reaction of CO to CO<sub>2</sub> takes place on the surface of a heterogeneous catalyst. The red line indicates the  $E_a$  without the catalyst whereas the blue line indicates the required  $E_a$  with the application of the catalyst. The application of the catalyst only has an influence on the reaction kinetics while the thermodynamics properties remain unchanged (Mielby, 2014).

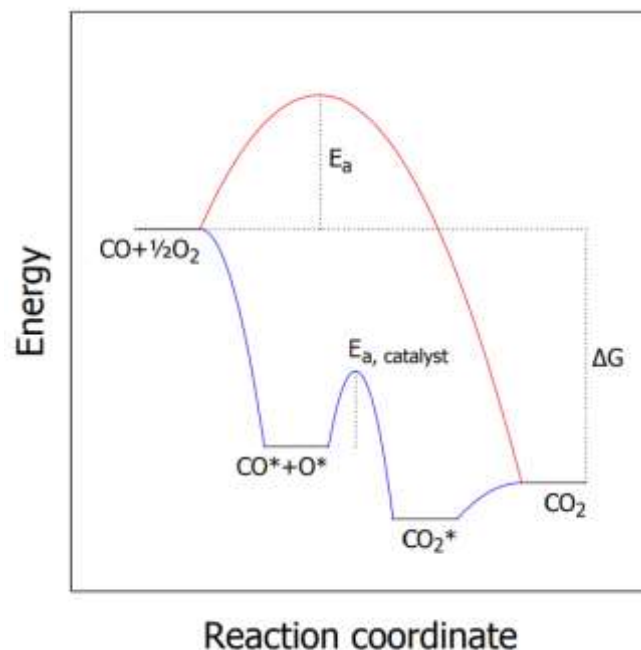


**Figure 2.10: An energy diagram that illustrates the oxidation process of CO to CO<sub>2</sub>, in gas phase, on the surface of the heterogeneous catalyst (taken from: Mielby., 2014)**

Babu and Karvembu (2013) has found that nanocatalysts have combined advantages over heterogeneous and homogeneous catalysts in a catalytic system. The application of nanomaterials has proven to have selective and rapid chemical transformations with excellent product yield; this is joined with the relatively easy catalyst separation and recovery. Nanomaterials including iron, aluminium, cobalt oxide, silica and titanium dioxide have been applied as catalysts.

The catalytic activity and the rate of reaction has been found to be a function of the enhanced surface area, particle structure and shape (Singh & Tandon, 2014). It has been stated that the variable and particle-specific activity of the catalyst of the nanostructures is a result of its heterogeneity as well as the variances in the particle shape and size. The development of higher-selective catalyst reduces the separation energy requirements of the system as well as the quantity of disposable chemical waste (Somorjai & Kliewer, 2009). Figure 2.11 shows a schematic of the general differences between homogeneous and heterogeneous bulk catalysts and nanostructured catalysts.

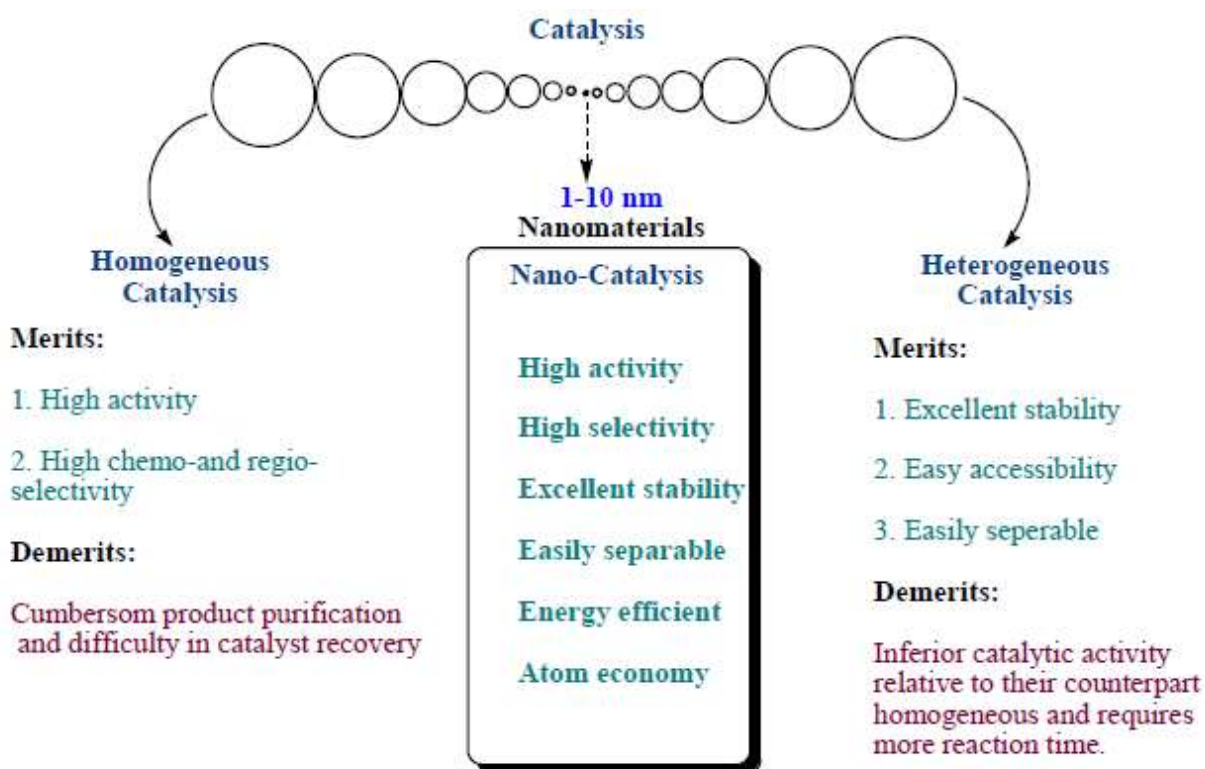


**Figure 2.11: Comparison between homogeneous, nano- and heterogeneous catalysts (taken from Singh & Tandon, 2014)**

A characteristic of nanoparticles is that they have a tendency to aggregate and cluster together to form larger particles, thus resulting in the loss of surface area. Polymer-based stabilisation has been identified as an efficient method to overcome this problem and to stabilise the nanostructures in a solution. The drawback of the stabilisation method is that the overall catalytic activity is reduced (Singh & Tandon, 2014.). If the application of nanocatalyst in a homogeneous system is considered, it is implied that the nanoparticles are in solution or suspension in the solvent. The main drawback of the homogeneous system is that additional steps are required for the recovery of the nanocatalyst from the solution. If the catalyst is non-recoverable, the probability of the process might be affected and an environmental threat arises (Gates, 2008), thus the application of heterogeneous nano-catalysts is favoured. Heterogeneous catalyst is generally in solid phase or immobilised on a solid inert matrix.

The concentration of the active sites on the nanoparticle catalyst is determined by the shape and size of the nanostructure. Advances in the synthesis of nanomaterials enable the accurate control of the surface-active sites by manufacturing catalyst that is mono-dispersed and shape-controlled (Silva et al., 2020). An example of the dependence of the selectivity of pyrrole hydrogenation on both the shape and size of the platinum (Pt) nano-catalyst is displayed in Figure 2.12.

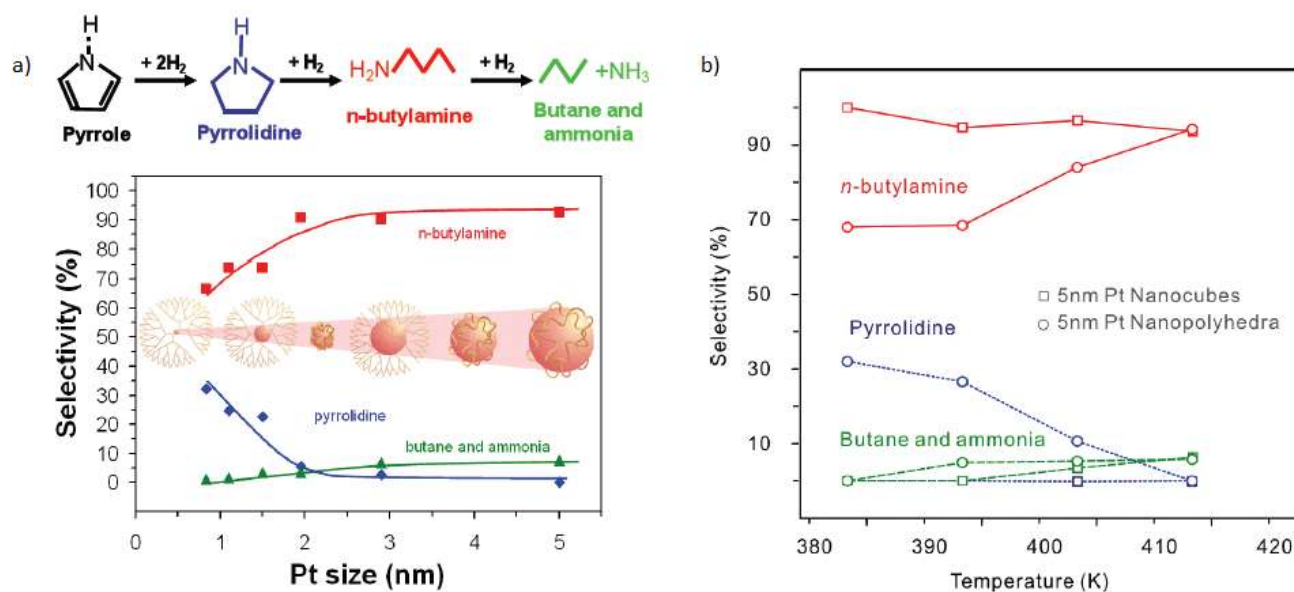


Figure 2.12: a) The dependence of the selectivity of the pyrrole hydrogenation on the particle size and b) The dependence of the selectivity of the pyrrole hydrogenation on the particle shape (taken from Yimin & Somorjar, 2010)

## 2.4.2 Treatment processes of textile wastewater

Rajasimman et al. (2017) and Hayat et al. (2015) state that due to the characteristics of textile wastewater it is considered to be hazardous to the environment and human health if discharged without the proper treatment. The textile wastewater effluent depends on the process type, equipment used and type of fibre the material consists of (Dilaver et al., 2018; Koyuncu and Topacik, 2003). The textile wastewater is characterised by the following: biological oxygen demand (BOD), chemical oxygen demand (COD), total suspended solids (TSS), total dissolved solids (TDS), concentration of chemicals, inorganic salts and heavy metals (Rajasimman et al., 2017).

## Textile Dyes

The classification of dyes is done according to their chemical composition and properties. Three main types of fibres that are applied in the textile manufacturing process have been identified: synthetic fibres (acrylic, nylon, polypropylene, polyester, acetate, ingeo and spandex), cellulose fibres (cotton, rayon, ramie, lyocell hemp and linen) and lastly protein fibres (mohair, wool, cashmere angora and silk) (Ghaly et al., 2014). Each identified type of applied fibre is dyed with a different types of dye. Synthetic fibres are dyed using basic dyes

(basic red 1 and basic orange 37), dispersed dyes (disperse navy 35 and disperse yellow) and direct dyes (for the dyeing of protein fibres), lanaset dyes (Bordeaux B and blue 5G) and acid dyes (triarylmethane dyes, azo dyes and anthraquinone dyes) are used (Burkinshaw, 1995). Direct dyes (direct brown 116, congo red and direct yellow 50), reactive dyes (procion MX, remazol, and cibacron F), indigo dyes (indigo carmine, Tyrian purple and indigo white) and naphthol dyes (fast blue B, fast yellow GC and fast scarlet R) are some of the common dyes used for the dyeing of cellulose fibres (Phillips, 1996). It was stated by Phillips (1996) that reactive dyes are the most commonly used for the dyeing of cellulose fibres.

Acid dyes are most commonly used for protein fibres due to the high pH that is found to denature proteins. According to Ghaly et al. (2014) an insoluble dye molecule is formed on the fibre as a result from the chemical reaction between the fibres and the acid dye. The three most important dyes for protein fibres include triarylmethane dyes, azo dyes, and anthraquinone.

Azo dyes, as illustrated in Figure 2.13, are known to have a chromophoric azo group (-N=N-) attached to an heterocyclic or aromatic nucleus at one end and an unsaturated molecule of heterocyclic, carbocyclic or aliphatic type at the other end. Azo dyes occupy the largest classification of dyes with the Colour Index (CI) (Ghaly et al., 2014). Based on the number of azo groups attached to the centre, the dyes are classified into groups mono-, di-, tri-, tetra-, etc.).

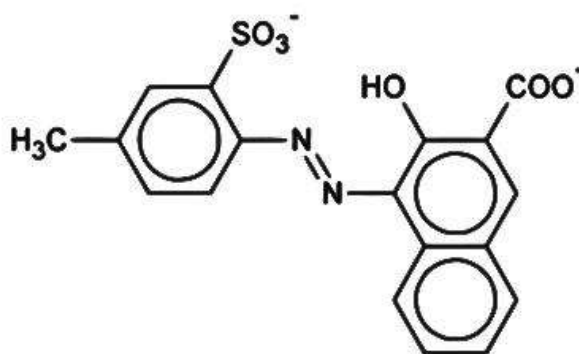
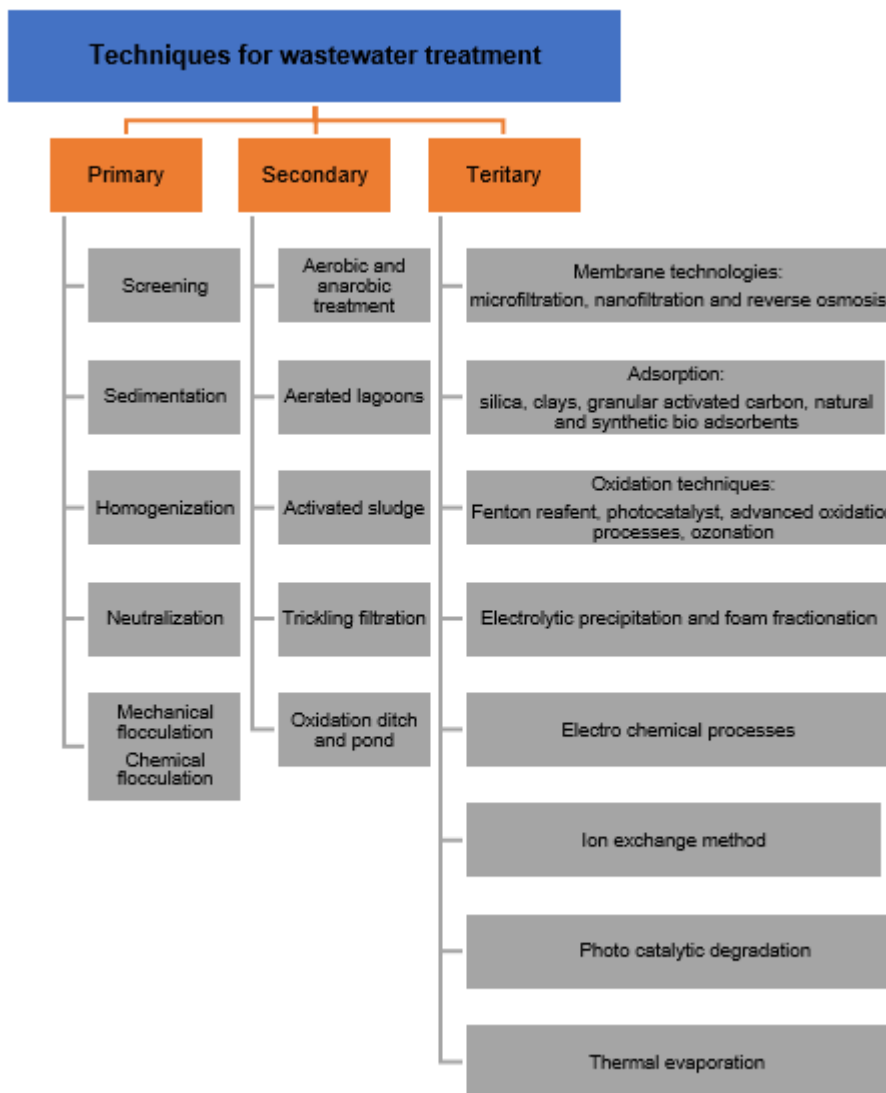


Figure 2.13: Chemical structure of Azo dyes (taken from Ghaly et al., 2014)

### **2.4.3 Treatment of textile wastewater**

Speel and Schwarz (2013) stated that the textile industry consists of various operation divisions such as sieving, scouring, rinsing, washing, bleaching, carbonisation, mercerising, finishing and dyeing processes. Numerous manufacturing processes are applied for the production of different types of textile products. The production process can be divided into two categories: wet processes (involving the application of dyes) and dry processes or spinning processes (Sette et al., 1996). The dyeing process is classified as a wet process and produces hazardous wastewater (Speel and Schwarz, 2013).

Textile wastewater can be treated by means of either physical, biological or chemical methods. Physical treatment methods are achieved by means of adsorption by activated carbon, membrane processes (for example reverse osmosis), and different precipitation methods (for example coagulation, sedimentation and flocculation and filtration). Biological treatment methods involve aerobic and anaerobic biological oxidation processes (Yimin & Somorjar, 2014). The disadvantage of these methods is that they are stunted by microorganism growth due to the presence of toxic metals in effluent water as well as the long retention time for efficient treatment (Ghaly et al., 2014). Chemical treatment methods involve the use of oxidisers such as ozone or hydrogen peroxide. When making a decision on which wastewater technology to apply, the following factors should be considered: conventional treatment options, quality of original water, treatment flexibility, removal of parent contaminants, the facility decontamination capacity, economic studies, final wastewater treatment system efficiency, potential reuse of the treated water and life cycle assessments for the determination of the compatibility of wastewater treatment technology (Yimin & Somorjar, 2014). The treatment of textile effluent wastewater generally involves three treatment processes: primary, secondary and tertiary treatments (as seen in Figure 2.14).



**Figure 2.14: Treatment techniques for the treatment of textile wastewater (adapted from Punzi, 2015)**

The primary treatment step of textile wastewater is the removal of grease and gritty materials, suspended solids and excessive quantities of grease and oil. This treatment process best operates within a pH range of 5 – 9; chemicals commonly used for the altering of the pH are boiler flue gas and sulphuric acid (Punzi, 2015). Firstly, the effluent is screened (using either bar or fine screens) for coarse suspended materials such as fibres, yarns, pieces of fabric and lint (Chipasa, 2001). The next step is the removal of suspended solids through sedimentation. It has been found that the sedimentation process is ineffective because the colloidal particles in the effluent are not removed. The last step in this process is mechanical flocculation which involves the low mixing of the effluent (Punzi, 2015).

The main objective of the secondary treatment process is for the removal of BOD, oil and phenol content of the textile wastewater as well as control of its colour. This can be achieved biologically, with the help of microorganisms under aerobic or anaerobic conditions. Aerobic bacteria use organic matter as a source of energy and nutrients. Among the aerobic systems are aerated lagoons, trickling filters and activated sludge systems. The generated sludge is stabilised by the anaerobic treatment process (Chipasa, 2001).

The tertiary treatment processes include technologies such as reverse osmosis, electro dialysis, ion exchange, and photocatalytic and advanced oxidation processes. The electrolytic precipitation of the effluents from the textile process includes the passing of an electric current through the effluent using electrodes. The electrochemical reactions cause the metal ions to dissolve and combine with finely dispersed particles in the solution that precipitates out (Punzi, 2015).

Reverse osmosis involves the application of membranes that have the ability to remove total dissolved solids along with ions and other larger species that are present in the effluent. This method has an efficiency above 90% (Trishitman et al., 2020).

The electro dialysis process uses membranes that have the ability to separate dissolved salts. The ions are transported through a semipermeable membrane by means of an electrical potential that passes through the water (Oztekin & Altin, 2016).

Ion exchange is a commonly used method that involves the passage of the effluents that move through beds of ion exchange resins. The ion exchange resins can either be anionically or cationically charged. For example, if the effluent passes through a cationic resin its cations are removed and replaced with hydrogen ions, leaving the effluent acidic. In return, if the effluent passes through an anion resin the anions are removed and are substituted with hydroxyl ions (Abdel-Raouf et al., 2019).

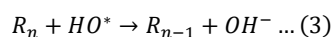
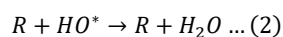
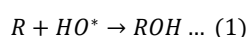
Sreeja & Sosamony (2016) stated that advantage oxidation processes (AOP) produce strong oxidising agents (such as sulphate radicals or hydroxyl radicals) and are thus considered to be a promising textile wastewater treatment process. For, the removal of pollutants in wastewater, AOP are considered as a highly competitive water treatment technology. All AOPs are characterised by a common chemical feature: the ability to produce highly reactive hydroxyl-free radical ( $\text{HO}^*$ ) radicals, a strong non-selective chemical oxidant that destroys organic compounds which cannot be oxidised by means of conventional oxidants such as oxygen, ozone and chlorine (Munter, 2001). Hydroxyl radicals are effective in destroying organic chemicals because they are reactive electrophiles which do not only react rapidly, but also non-selectively with nearly all electron-rich organic compounds. Once the  $\text{HO}^*$  radicals

have been generated they can attack the organic chemicals through hydrogen abstraction, electron transfer and radical combination (Sreeja & Sosamony, 2016). In comparison with conventional oxidation, the oxidation potential of AOPs is quantified as 2.80 V which makes them exhibit faster oxidation reaction rates (Table 2.2). Deng and Zhao (2015) stated that at an oxidation potential between 1.95 V and 2.8 V the hydroxyl radicals are the most reactive oxidising agents in water, depending on the pH.

**Table 2.2: The oxidant potential of various oxidants (taken from Mayyahi & Al Asadi, 2018)**

<b>Oxidant</b>	<b>Oxidation Potential (V)</b>	<b>EOP Relative to Chlorine</b>
Fluorine	3.03	2.25
Hydroxyl radical (OH*)	2.80	2.05
Oxygen (Atomic)	2.42	1.78
Ozone	2.08	1.52
Hydrogen Peroxide	1.78	1.30
Hypochlorite	1.49	1.10
Chlorine	1.36	1.00
Chlorine Dioxide	1.27	0.93
Molecular oxygen	1.23	0.90

The reactions that take place are as follows:



There are several technologies or methods that are classified under advanced oxidation processes. Generally, these methods combine a strong oxidising agent with a catalyst such as transitional ions and irradiation (Mayyahi & Al Asadi, 2018). This can be seen in Figure 2.15.

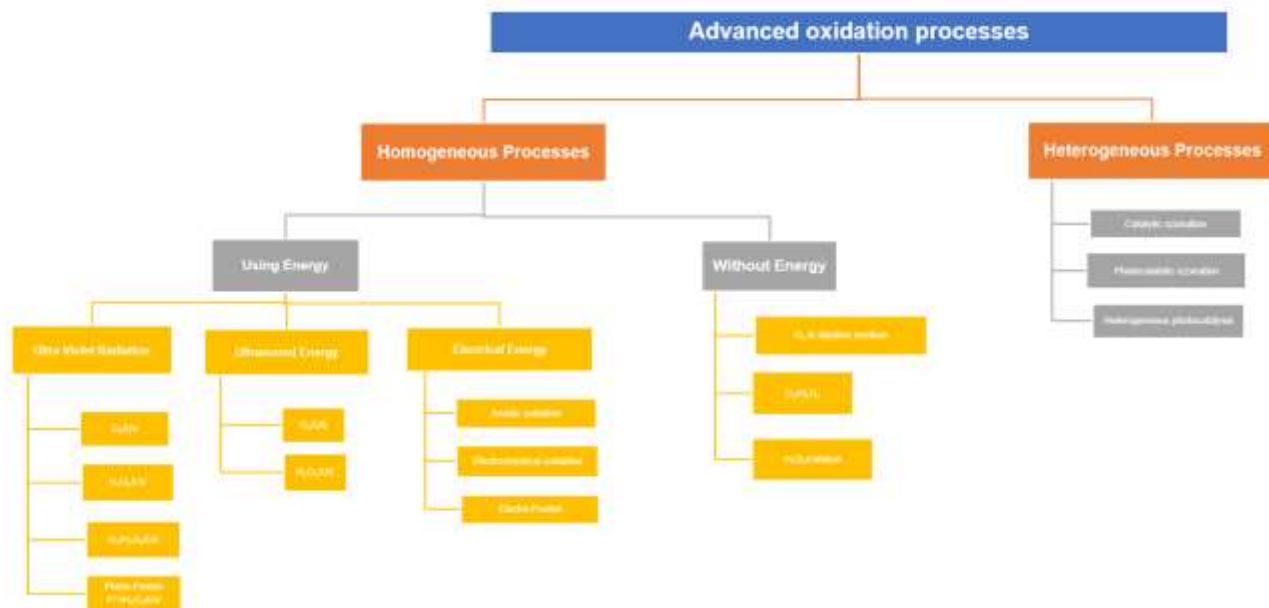


**Figure 2.15: Classification of advance oxidation processes (adapted from Mayyahi & Al Asadi, 2018)**

Homogenous advanced oxidation processes that use UV radiation are normally applied for the degradation of compounds which adsorb UV radiation within the corresponding range of the spectrum. If the compounds are able to absorb UV light at lower wavelengths, it renders them suitable for photodegrading process (Mayyahi & Al Asadi, 2018). These processes involve: (1) Photolytic ozonation ( $O_3/UV$ ) which is effectively used to oxidise and destroy toxic organic compounds in wastewater; (2) The hydrogen peroxide and ultraviolet radiation ( $H_2O_2/UV$ ) process where hydroxyl radicals are generated from the pyrolysis of  $H_2O_2$  and various propagation reactions that correspond with the process. This method requires relatively high doses of  $H_2O_2$  and a longer UV exposure is required (Mayyahi & Al Asadi, 2018). Tisa et al. (2014) stated that various studies have found that rate of photolysis of hydrogen peroxide is highly pH-dependent and the rate tends to increase in alkaline conditions. (3) A mixture of hydrogen peroxide and an ion (II) salt is known as the Fenton reagent. The Fenton process is described as the catalytic generation of  $OH^\bullet$  radicals through a series of chain reactions between hydrogen peroxide ( $H_2O_2$ ) and the ferrous ion ( $Fe^{2+}$ ). The generated  $OH^\bullet$  radicals are then used to oxidise the organic compounds in wastewater (Zhang et al., 2005); (4) anodic oxidation process involves the accelerated electrochemical process that is intensified by the natural oxide skin of the aluminium. Over a set time period, the transparent oxide layer becomes considerably thicker compared to the natural oxide layer (Nidheesh et al., 2012).

In the heterogeneous AOPs catalysts are applied for the degradation of compounds. In other words, the application of the heterogeneous advanced oxidation process that uses catalyst

refers to the presence of contaminants in the aqueous phase and the catalyst is usually in the solid phase. Results have shown that the acceleration of chemical processes is due to the presence of electron-hole pairs (Nidheesh et al., 2012). The photogenerated electrons and holes result in oxidation and reduction processes respectively. For aqueous solutions, oxidation of water molecules is absorbed to the catalyst results in  $\text{OH}^*$  radicals. The process is normally implemented in aerobic conditions with the species to be reduced being oxygen, a process which generates a superoxide radical (Mayyahi & Al Asadi, 2018). Photocatalysts are perceived as good due to being chemically inert, able to utilise visible or near photostable, UV light inexpensive and non-toxic. The activation of Oxone<sup>®</sup> using cobalt was found by Hu & Long (2016) to be more efficient than the Fenton reaction at a pH of 7 with a lower concentration dosage of reagent; this is discussed below.

### **Advance oxidation processes for the treatment of textile wastewater using cobalt-oxide nanocatalyst**

In 1958 the catalytic decomposition of Oxone<sup>®</sup>/peroxymonosulfate using cobalt was firstly reported and was shown to proceed via radical mechanism and since then it has been established that cobalt is the best catalyst-activator of this versatile inorganic peroxide (Anipsitakis et al., 2004). The effects of variables on the decomposition of potassium monopersulphate (Oxone<sup>®</sup>) were studied by Rivas et al. (2009). It was found that the breakdown of the monopersulphate molecule is influenced by the application of radiant or thermal energy and effect of oxide on transition metals and heterogeneous catalysis. As illustrated in Figure 2.16, the cobalt-mediated activation of Oxone<sup>®</sup> leads to the formation of sulfate radicals. The peroxydisulphate anion can also be activated to form sulphate radicals with elevated pH levels, transitional metals and heat (Deng & Zhao, 2015). These species have been found to effectively oxidise and transform several organic compounds (Anipsitakis et al., 2005). It is believed that the mechanism of the heterogeneous catalysis, as illustrated in Figure 2.16, consists of a one-electron transfer process: the oxidation of Co(II) to Co(III) with Oxone<sup>®</sup> / peroxymonosulfate and the formation of sulfate radicals, the reduction of Co(III) to Co(II) and lastly the generation of the Oxone<sup>®</sup> radical.

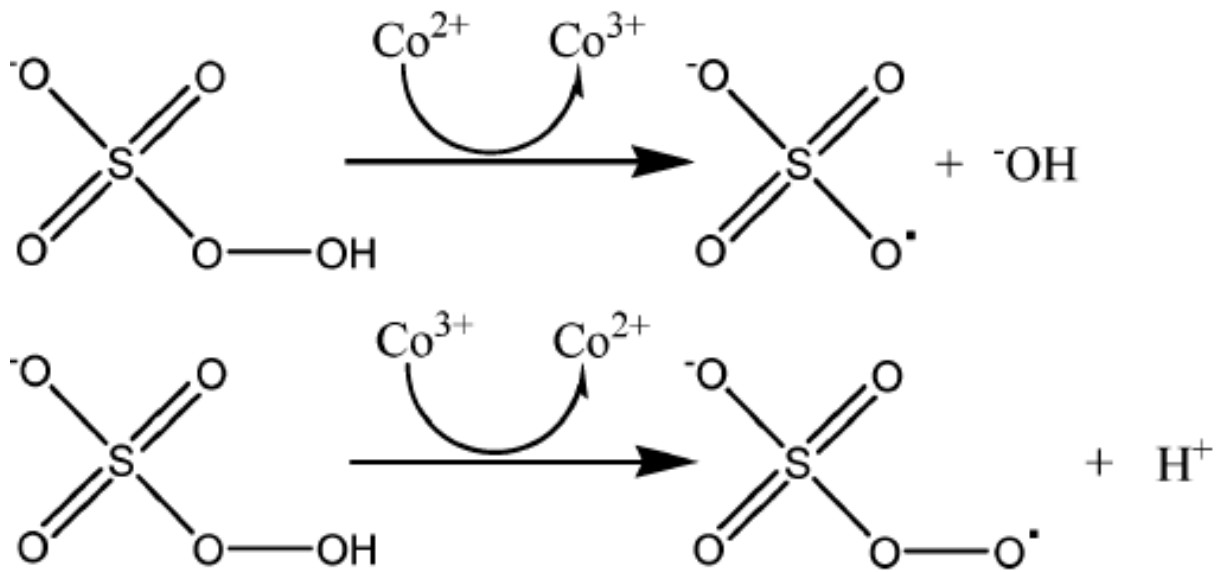


Figure 2.16: Cobalt-mediated activation of Oxone (taken from Anipsitakis et al., 2005)

Anipsitakis et al. (2005) conducted a study where two commercially available cobalt oxide forms ( $\text{CoO}$  and  $\text{Co}_3\text{O}_4$ ) were screened for the heterogeneous activation of Oxone<sup>®</sup> and the destruction of 2,4-dichlorophenol (2,4-DCP) in water. Table 2.3 indicates the results of this screening. In particular the first two rows show the transformation of 2,4-DCP with  $\text{CoO}/\text{Oxone}^{\text{®}}$  and  $\text{Co}_3\text{O}_4/\text{Oxone}^{\text{®}}$  as well as the dissolution of cobalt from the two oxides. With  $\text{CoO}$  almost a complete destruction of 2,4-DCP can be achieved within half an hour of reaction time.

**Table 2.3: Comparative results from the transformation of 2,4-DCP using different cobalt compounds  
(adapted from Anipsitakis et al., 2005)**

Cobalt source	Co <sup>b</sup> (mg/L) (2h)	% tran. DCP (30 min)	pH <sub>0</sub>	pH <sub>f</sub>	pH area
CoO	3.01	100.00	6.40	2.80	Acidic
Co <sub>3</sub> O <sub>4</sub>	0.59	73.80	6.40	2.80	Acidic
Co <sub>3</sub> O <sub>4</sub>	0.73	85.20	6.40	2.80	Acidic
Co <sub>3</sub> O <sub>4</sub>	0.03	99.90	6.40	8.00	Neutral
CoO	2.75	99.90	6.40	2.90	Acidic
CoO <sup>c</sup>	1.01	83.30	6.40	2.90	Acidic
CoCl <sub>2</sub>	1.00	77.20 ± 4.20	6.40	2.90	Acidic
Co <sub>3</sub> O <sub>4</sub>	0.75 ± 0.06	71.70 ± 1.90	6.40	2.90	Acidic
Co(NO <sub>3</sub> ) <sub>2</sub>	0.80 ± 0.08	50.90 ± 9.50	6.40	2.90	Acidic
CoO	0.77	99.10	7.00	8.30	Neutral
CoO <sup>c</sup>	0.39	96.70	7.00	8.30	Neutral
Co <sub>3</sub> O <sub>4</sub>	0.07 ± 0.02	91.00 ± 5.90	7.00	8.30	Neutral
Co(NO <sub>3</sub> ) <sub>2</sub>	0.07 ± 0.01	36.70 ± 1.60	7.00	8.30	Neutral

Figure 2.17 shows that under acidic conditions, Co<sub>3</sub>O<sub>4</sub>/Oxone<sup>®</sup> demonstrated some heterogeneity in comparison with a homogeneous Co/Oxone<sup>®</sup>, while Figure 2.18 illustrated that the heterogeneous character of Oxone<sup>®</sup> activation with Co<sub>3</sub>O<sub>4</sub> was much more distinct at neutral pH, and the quantity of Co leached in solution was approximately tenfold less than the case of an acidic pH.

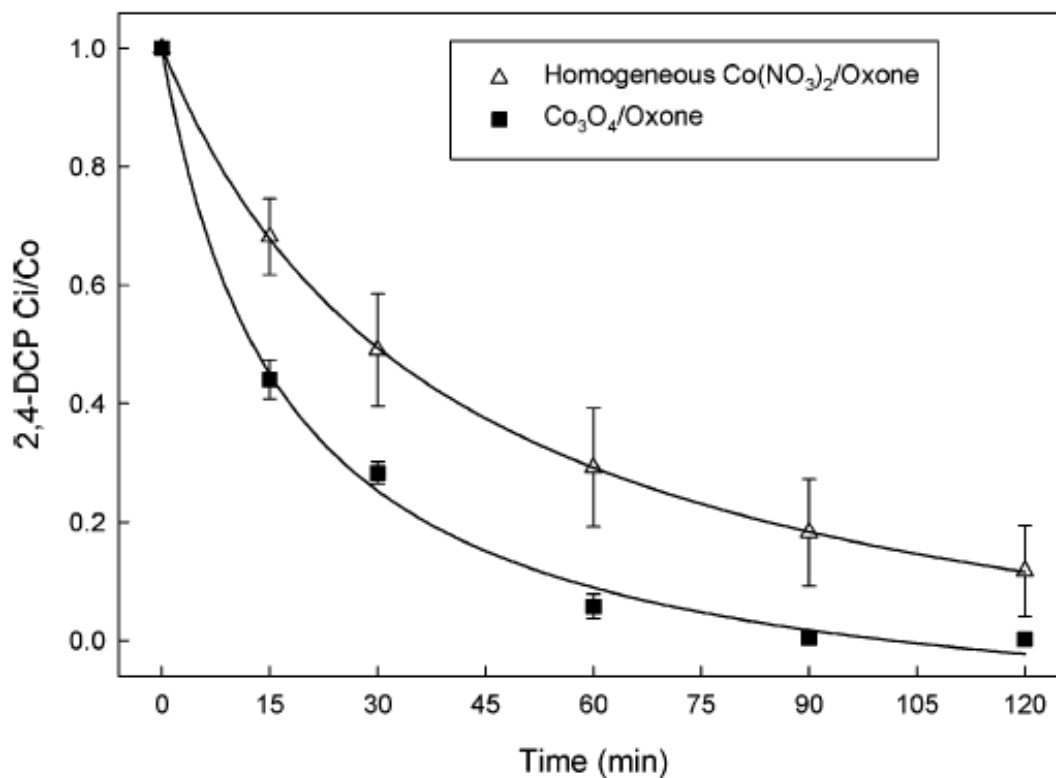


Figure 2.17: 2,4-DCP transformation with Co<sub>3</sub>O<sub>4</sub>/ Oxone® and homogeneous Co / Oxone® at acidic pH (taken from Anipsitakis et al., 2005)

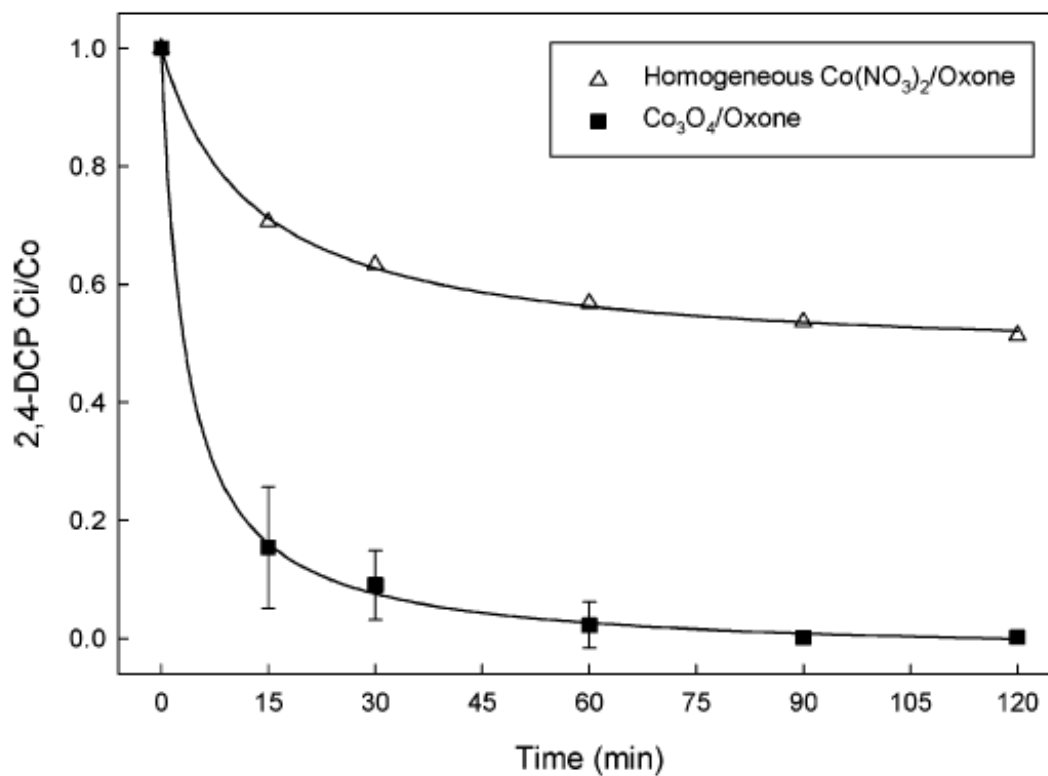


Figure 2.18: 2,4-DCP transformation with Co<sub>3</sub>O<sub>4</sub>/ Oxone® and homogeneous Co/ Oxone® at neutral pH (taken from Anipsitakis et al., 2005)

According to Hu & Long (2016) heterogeneous cobalt-based catalysts have two critical properties, reusability and stability thus making them beneficial for the breakdown of organic contaminants and gives them a competitive edge over other AOPs by being environmentally friendly and economically feasible. Saputra et al. (2013) and Wang et al. (2015) treated wastewater by using  $\text{Co}_3\text{O}_4$  that was produced by the hydrothermal synthesis process. Saputra et al. (2013) used a cobalt nitrate hexahydrate precursor during the hydrothermal synthesis process at a reaction temperature of  $120^\circ\text{C}$  and a residence time of 5 hours to produce  $\text{Co}_3\text{O}_4$  with a particle size between  $0.02\ \mu\text{m}$  and  $0.25\ \mu\text{m}$ . The catalytic efficiency was evaluated during the degradation of phenol with PMS as an oxidiser. A degradation percentage of 100% was achieved within 20 minutes using 2 g/L PMS, 20 mg/L phenol concentration and a catalyst loading of 0.2 g/L. Wang et al. (2015) produced  $\text{Co}_3\text{O}_4$  with a particle size of 40 nm via the hydrothermal synthesis process using a precursor solution of cobalt nitrate hexahydrate and urea. The catalytic efficiency was evaluated during the degradation of phenol with PMS as an oxidiser. A degradation percentage of 100% was achieved within 45 minutes using 6.5 mmol PMS, 25 mg/L phenol concentration and a catalyst loading of 0.6 g/L.

From the studies done by Saputra et al. (2013) and Wang et al. (2015) it can be seen that heterogeneous cobalt-based catalysts, produced by a hydrothermal synthesis, can successfully be used to break down organic contaminants using AOP in a batch slurry. There is a lack of understanding how the process parameters, such as reaction temperature, residence time, crystallite size, precursor type and concentration affect the degradation potential of the  $\text{Co}_3\text{O}_4$  nanocatalyst in an AOP.

## 2.5. Design of experiments

According to Montgomery (2017), efficient, balanced and economical experimental designs are developed by the design of experiments (DoE) methodology, which refers to the combination of statistical and mathematical techniques. DoE is applied to setups such as screening, factorial and split-plot designs, building of linear and response surface statistical models and the optimisation of the process (Morris, 2011). DoE is a powerful tool for managing process inputs for the optimisation process due to the different designs created with this methodology that allows inferences with high confidence levels (Antony et al., 2020).

## 2.5.1. Response surface methodology

The response surface methodology (RSM) approach develops an experimental design which integrates all of the independent variables and creates a set of equations based on input data that can propose theoretical value of an output (Said et al., 2015). RSM is a collection of several designs such as central composite (CCD) and Box-Behnken designs (BBD). In this work, a BBD design was employed (Hassanzadeh et al., 2017; Said et al., 2015). Optimization by means of the CCD method evaluates a single variable or the cumulative effect of the variables to the response. The CCD method is appropriate for fitting second order polynomial equations that have been frequently applied for optimising research problems (Said et al., 2015; Asghar et al., 2014). Figure 2.19 shows the steps that were followed by the CCD design.

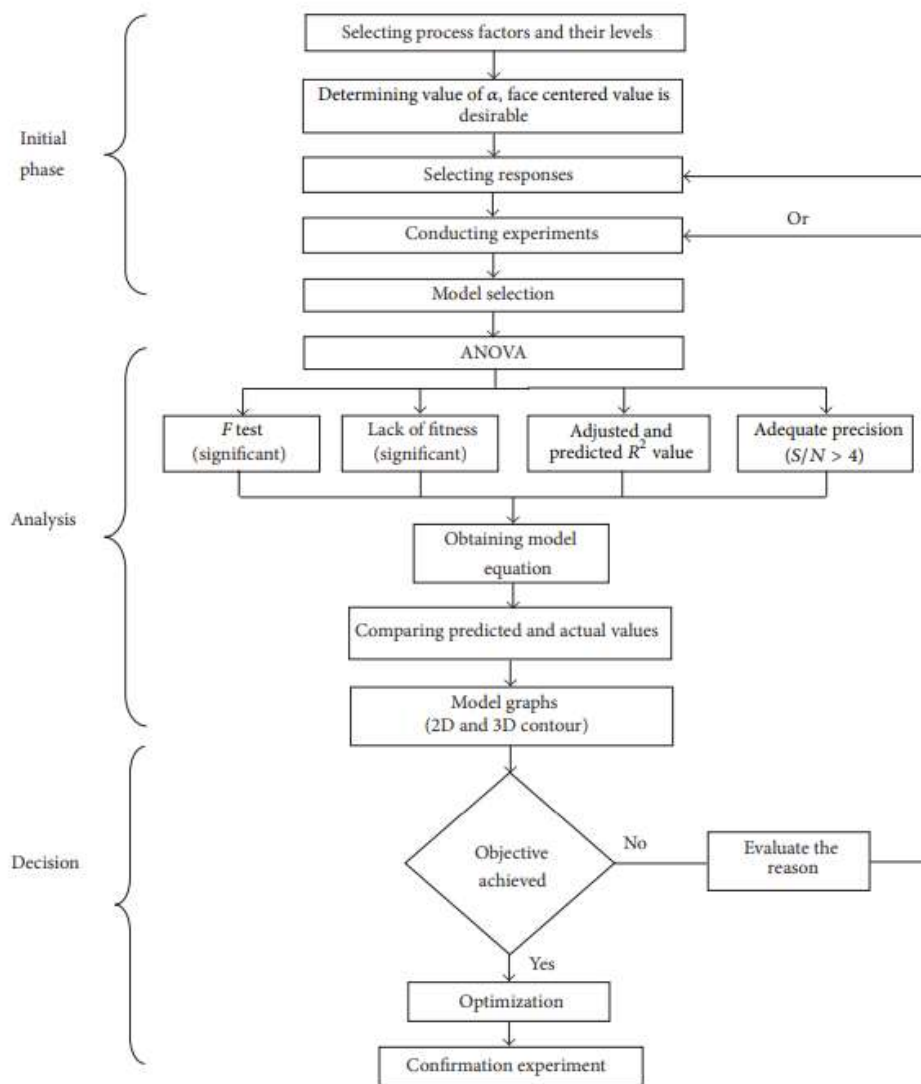


Figure 2.19: Flow diagram for the CCD method (taken from Asghar et al., 2014)

The design points for this method are divided in three groups (Asghar et al., 2014):

- Two-level factorial design points ( $2k$ ), consisting of possible combinations of +1 and -1 levels of factors.
- $2k$  axial points or points fixed axially at a distance  $\alpha$  from the centre and quadratic terms are generated. Alpha ( $\alpha$ ) is used to determine the location of axial points in the experimental domain. The alpha value determines if the design is spherical, orthogonal, rotatable, or face-centered.
- Replicate terms are represented by the centre points. The centre points provide estimate of the experimental error.

The number of experiments designed by the CCD can be seen in Equation 2-2 where N is the total number of experiments, k is the number of factors studied and n is the number of replicates.

$$N = k^2 + 2k + n \quad \text{Equation 2-2}$$

### 2.5.2. Analysis of variance

The analysis of variance (ANOVA) used evaluate the degree of accuracy held by the derived model is based on several responses. The significance of the model terms is determined using Fisher's F-test, sum of squares (SS), mean sum of squares (MS) and degrees of freedom (DF) (Box et al., 2005). CCD and Box-Behnken designs, etc., are generally approximated by a second order regression model equation that is developed to fit to the experimental data by application of Design-Expert software (Noordin et al., 2004; Dhawane et al., 2015). Equation 2-3 shows the regression mode; where the regression coefficients are represented by  $b_0$ ,  $b_i$ ,  $b_{ii}$ ,  $b_{ij}$  and  $X_i$  ( $i = 1, \dots, k$ ) are the coded independent variables. The significance of the regression coefficients are determined by the F-test and p-value. The significance of the model terms is determined by the p-values that are lower than 0.05, indicating the statistical significance at 95% confidence level (Noordin et al., 2004; Nautiyal & Shukla, 2018).

$$Y = b_0 + \sum_{i=1}^k b_i X_i + \sum_{i=1}^k b_{ii} X_i^2 + \sum_{i=1}^k b_i X_i + \sum_{i=1}^{k-1} \sum_{j=2}^k b_{ij} X_i X_j \quad \text{Equation 2-3}$$

According to Murray et al. (1990) the interaction effects between two factors while the third one is held constant are defined by two-dimensional and three-dimensional surface plots used to define the interaction effects of two factors as the third one is held constant.

## 2.6. Material characterisation techniques

### 2.6.1. X-ray diffraction

X-ray diffraction (XRD) analysis is used to provide the following information regarding nanostructured materials: surface area, crystal size and disorder, degree of isomorphous substitution and structural parameters (unit cell edge lengths) (Graef & Henry, 2012). The number of symmetrical elements are described by the ordered arrangement of a crystal atom. The intercepts that the plane makes with the system axes describe the position of any plane of atoms within the crystal. The reciprocal value (hkl) is used to describe the intercepts. Han (2001) stated that X-ray diffraction indicates the interaction between the electromagnetic waves with the atoms of the crystal. The X-ray monochromatic beam is directed towards the crystalline material; the X-rays are scattered into all directions as soon as the electrons surrounding the atoms interact with the incident X-ray photons.

The scattered X-rays, at certain angles ( $\theta$ ), have different wavelengths ( $\lambda$ ). The direction of the scattered X-ray is directly related to the d-values, distance between atomic planes and the angle at which the wave enters and exits the crystal. The diffraction in terms of reflection of an incident wave redrawn as described by Bragg's law (Williams & Carter, 1996) demonstrates the constructive interference of scattered waves and this relationship is described by means of the Bragg equation (Equation 2-4) (Graef & Henry, 2012); where  $d_{hkl}$  is the distance between the set of hkl plates,  $\theta$  is the angle at which the X-ray wave hits the crystal, n is the complete number of wavelengths and  $\lambda$  is the wavelength. According to Cullity & Stock (2001), the X-rays remain in phase and this is known as constructive interface. Bragg's equation is the relationship between the reflected X-rays at certain angles and the lattice planes of the crystals.

$$2d_{hkl}\sin\theta = n\lambda$$

Equation 2-4

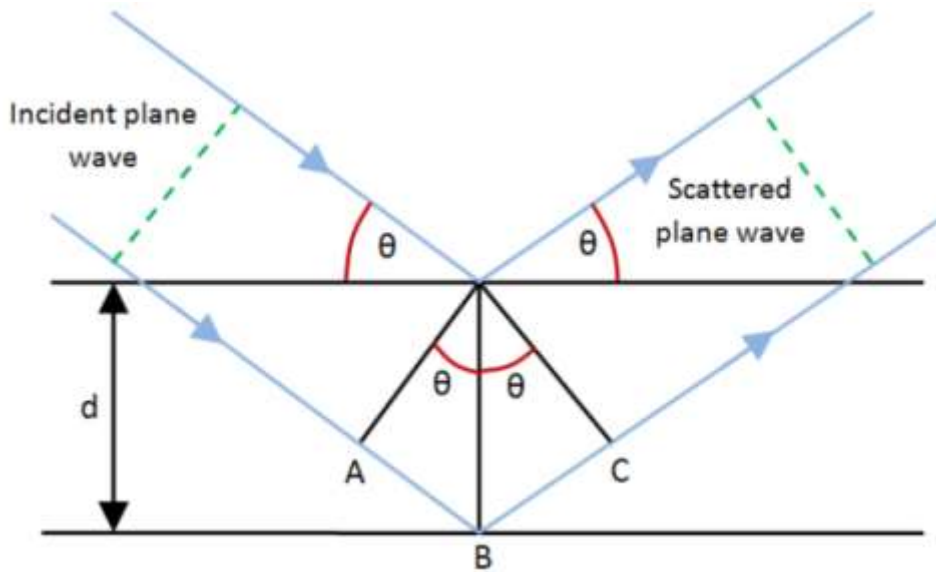


Figure 2.20: The diffraction in terms of reflection of an incident wave redrawn as described by Bragg's law (Williams & Carter, 1996)

### 2.6.2. Brubauer, Emmett and Teller (BET) surface area

According to Ahuja & Scypinski (2001), the surface area of a solid material provides invaluable information on the available void spaces on the surface. This characterisation method is dependent on the physical adsorption and desorption phenomena of gasses onto the pores and surface of the solid specimen. This analysis method provides information regarding the nature of the specific surface area of the porous nonofiber. Inert gasses such as argon or nitrogen are used to determine the surface area of the material. The BET equation for gas adsorption (as represented in Equation 2-5) is most commonly used to determine the monolayer and specific surface area.

$$v = (v_m c p) / ((p_0 - p) \left[ 1 + (c - 1) \left( \frac{p}{p_0} \right) \right]) \quad \text{Equation 2-5}$$

Where  $v$  is the adsorbed volume of gas,  $v_m$  is the adsorbed monolayer volume,  $p$  is the equilibrium gas pressure,  $p_0$  is the saturation pressure and  $c$  are the BET constant, which is exponentially related to the energy of the monolayer adsorption. The gas adsorption analysis works on the basis that: (1) the adsorption of the gas occurs on the well-defined surfaces, (2) at saturation pressure the quantity of layers absorbed goes into infinity; and (3) there is no interaction between the adsorbed layers. The BET surface area measurement takes into account the internal porosity of mineral grains and the microscopic irregularities (Drever, 2005). For example, the classification of the porosity of the material and the surface features are classified on the basis of the shape of the curve that is obtained from the adsorption-

desorption isotherm (Tran et al., 2017). This process is influenced by parameters such as pressure, temperature, material characteristics, etc.

This surface analysis tool is efficient for nanostructured and / or porous catalyst due to the fact that all the electrochemical reactions that are facilitated are known to be surface reactions (including oxygen evolution and oxygen reduction reactions) (Tran et al., 2017). Thommes et al. (2015) state that the characterisation of nanoporous materials requires the development of high resolution experimental protocols for the adsorption of various subcritical fluids, for example nitrogen at  $T = 77$  K, carbon dioxide at 273 K, argon at 87 K, organic vapours and supercritical gases.

The Brunauer–Emmett–Teller method continues to be the most widely used analysis method for evaluating the surface area of porous and finely-divided materials (Thommes et al., 2015). The BET method is used to accurately investigate and describe the surface of the catalyst to elucidate the effect of the nanostructured material design on the durability and activity of the produced catalyst (Tran et al., 2017).

## 2.5 Conclusions

This chapter provided an overview on metal oxide nanoparticle properties and how the properties of the particle are affected by the nanostructure. The toxicity of cobalt and how it affects the human body and the environment. The various methods for the synthesis of nanoparticles were discussed and how the produced nanocatalyst can be applied for the treatment of textile wastewater.

Studies done by Nassar (2013), Nassar and Ahmed (2011), Heuvel (2020) and Yarestani et al. (2014) showed that  $\text{Co}_3\text{O}_4$  could successfully be synthesised by the hydrothermal synthesis method.

For cobalt hydroxide powders, hydroxide exists as one of two polymorphs – alpha cobalt hydroxide ( $\alpha\text{-Co(OH)}_2$ ) and beta cobalt hydroxide ( $\beta\text{-Co(OH)}_2$ ) and is most commonly identified by their color.  $\alpha\text{-Co(OH)}_2$  exhibits a green-blue colour while  $\beta\text{-Co(OH)}_2$  is identified by its pink colour (Al-Ghoul et al., 2010; Heuvel, 2020).

Nassar (2013) synthesised  $\text{CoCO}_3$  and  $\text{Co}_3\text{O}_4$  nanoparticles by a surfactant-free hydrothermal method using a precursor made up of ammonium carbonate and cobalt acetate. It was found that a molar ratio ( $\text{Co}^{2+}:\text{CO}_3^{2-}$ )  $\geq 1:3$  produced pure phase of  $\text{CoCO}_3$  during the hydrothermal synthesis reaction.

CoCO<sub>3</sub> nanoparticles synthesised by Nassar and Ahmed (2011) by using different cobalt salts (cobalt acetate (Co(CH<sub>3</sub>COO)<sub>2</sub>·4H<sub>2</sub>O), cobalt chloride (CoCl<sub>2</sub>·6H<sub>2</sub>O), cobalt nitrate (Co(NO<sub>3</sub>)<sub>2</sub>·4H<sub>2</sub>O) showed that the CoCO<sub>3</sub> crystals produced by cobalt acetate and cobalt nitrate were uniform while cobalt chloride produced CoCO<sub>3</sub> crystals a different morphology. Comparing the average crystallite size of the produced Co<sub>3</sub>O<sub>4</sub> nanoparticles it was found that cobalt acetate precursor produced Co<sub>3</sub>O<sub>4</sub> nanoparticles with largest crystallite sizes while the smallest crystallite sizes were obtained from the cobalt nitrate precursor.

Lester et al. (2012) produced Co<sub>3</sub>O<sub>4</sub> nanoparticles by a controlled continuous hydrothermal synthesis process to evaluate the effect of the operating parameters on the Co<sub>3</sub>O<sub>4</sub> nanoparticles. The crystallite sizes of the Co<sub>3</sub>O<sub>4</sub> nanoparticles exhibited that as the reaction temperature increased the intensity of the peak increased thus showing a clear increase in crystallinity. Heuvel (2020) found that an increase in the calcination temperature resulted in an increase in the crystallite size. For the cobalt chloride hexahydrate precursor, the crystallite size increased from 7.09 nm to 34.89 nm while in the case of cobalt nitrate hexahydrate crystallite size increased from 17.08 nm to 27.91 nm (Heuvel, 2020). Lester et al. (2012) found that the smallest particle sizes were found at the highest precursor concentrations.

It was found that there is an increase in the conversion of cobalt acetate tetrahydrate to Co<sub>3</sub>O<sub>4</sub> nanoparticles as the reaction temperature and that the influence of the residence time was less significant at higher temperatures Lester et al. (2012).

Hu & Long (2016) stated that heterogeneous cobalt-based catalysts have two critical properties, reusability and stability that makes them beneficial for the breakdown of organic contaminants and gives them a competitive edge over other AOPs by being environmentally friendly and economically feasible. Saputra et al. (2013) and Wang et al. (2015) evaluated the catalytic efficiency of the heterogeneous cobalt-based catalysts, produced by a hydrothermal synthesis method using a cobalt nitrate hexahydrate precursor, during the degradation of phenol with PMS as an oxidiser. Saputra et al. (2013) achieved a degradation percentage of 100% within 20 minutes using Co<sub>3</sub>O<sub>4</sub> nanocatalyst with a particle size between 0.02 µm and 0.25 µm. Wang et al. (2015) used Co<sub>3</sub>O<sub>4</sub> nanocatalyst with a particle size of 40 nm and achieved degradation percentage of 100% within 45 minutes.

Therefore, this study focuses on the effect of the interactions between the operating parameters (reaction temperature, precursor concentration, residence time) and effect of the precursor anion on the Co<sub>3</sub>O<sub>4</sub> nanoparticle crystallite size and product yield. The catalytic ability of the produced Co<sub>3</sub>O<sub>4</sub> nanocatalyst is evaluated during the colour degradation of synthetic textile dye solutions.

## Chapter 3 Experimental Procedure

### 3.1. Introduction

In this chapter the hydrothermal synthesis technique that is applied for the synthesis of  $\text{Co}_3\text{O}_4$  nanoparticles using cobalt salt with different counter ions at various operating parameters is described.

These experiments firstly involve a two-step hydrothermal synthesis process that involves the hydrothermal synthesis of cobalt hydroxide nanoparticles using three different cobalt salts and the calcination of the produced structures to produce  $\text{Co}_3\text{O}_4$  nanocatalyst. Three different precursor salts were used during these experiments: cobalt acetate tetrahydrate, cobalt chloride hexahydrate and cobalt nitrate hexahydrate with a 1:3 ratio to ammonium hydroxide solution. Factorial trial experiments were set up in order to determine the operating parameters for each set of experiments. Secondly, the cobalt hydroxide nanoparticles were calcined at  $350^\circ\text{C}$  for 3 hours in a furnace. The catalytic efficiency of the produced  $\text{Co}_3\text{O}_4$  nano-catalyst was evaluated through the degradation of methyl orange. This was achieved through an advanced oxidation process carried out in a slurry system that consists of a methyl orange solution,  $\text{Co}_3\text{O}_4$  nanocatalyst and peroxymonosulphate (Oxone<sup>®</sup>). The degradation process was evaluated for 30 minutes and the colour were measured against deionised water by means of a handheld spectrophotometer with a sample taken every 2 minutes.

### 3.2. Research design

An investigation done by Nassar and Ahmed (2011) showed that a 1:3 ratio of  $[\text{Co}^{2+}]$ :  $[\text{CO}_3^{2-}]$  produced pure cobalt carbonate nanoparticles, with good crystallinity. Therefore, it was decided to also use a 1:3 ratio of  $[\text{Co}^{2+}]$ :  $[\text{OH}^-]$  ratio for this study. Heuvel (2020) showed that  $\text{Co}_3\text{O}_4$  nanoparticles can be obtained at calcination temperatures between  $300^\circ\text{C}$  and  $500^\circ\text{C}$  at 3 hours. Thus, was a calcination temperature of  $350^\circ\text{C}$  and 3 hours chosen, instead of the  $500^\circ\text{C}$  used by Nassar and Ahmed (2011). Heuvel (2020) used a molar concentration of 0.23 M to produce  $\text{Co}_3\text{O}_4$  nanoparticles; this study wanted to investigate the effect of precursor concentration on the yield and crystallite size thus was a precursor concentration range of 0.1 M – 0.5 M selected. Nassar (2013) produced  $\text{Co}_3\text{O}_4$  nanoparticles between  $80^\circ\text{C}$  and  $160^\circ\text{C}$ , Heuvel (2020) produced  $\text{Co}_3\text{O}_4$  nanoparticles at  $105^\circ\text{C}$  and Yarestani et al. (2014) produced  $\text{Co}_3\text{O}_4$  nanoparticles at  $180^\circ\text{C}$ . A temperature range of  $90^\circ\text{C}$  –  $180^\circ\text{C}$  was selected to investigate the effect of temperature on the yield and crystallite size. Nassar (2012)

produced  $\text{Co}_3\text{O}_4$  nanoparticles in 30 minutes while Heuvel (2020) produced  $\text{Co}_3\text{O}_4$  nanoparticles in 6 hours. To study the effect of the residence time on the yield and crystallite size a residence time range between 30 minutes and 6 hours were selected.

The interaction between the operational process parameters was evaluated by means of a three factor, three level face-centred composite design (CCD) using Design-Expert® software with six center-points. Three factors were varied during the experimental producer: reaction temperature (A), concentration of the metal salt (B) and residence time (C). The software was applied to determine the design and the number of experiments and to evaluate the interactions between the independent factors. The CCD method is commonly used for building a second-order polynomial model for the response variables in the response surface methodology.

This experimental set-up was repeated for each precursor so that the effect of each base salt could be evaluated as well as the effect of the process conditions on the product yield and crystallite size. Table 3.1 shows the layout of the FCCD experimental design.

**Table 3.1: Three level three factor experimental design**

Sample name	Temperature (°C)	Residence time (h)	Concentration (M)
1	180	3.25	0.3
2	90	6	0.1
3	135	6	0.3
4	135	3.25	0.3
5	90	0.5	0.5
6	135	3.25	0.3
7	90	3.25	0.3
8	135	3.25	0.3
9	135	3.25	0.3
10	135	3.25	0.3
11	135	3.25	0.1
12	180	0.5	0.5
13	135	3.25	0.3
14	180	6	0.1
15	90	0.5	0.1
16	90	6	0.5
17	135	3.25	0.5
18	180	6	0.5
19	135	0.5	0.3
20	180	0.5	0.1

### 3.3. Experimental methods

This section describes the chemicals, equipment and methodology that were used for the synthesis of  $\text{Co}_3\text{O}_4$  and the testing of the produced catalyst through advanced oxidation process.

Analytical grade cobalt salt (cobalt chloride, cobalt acetate tetrahydrate and cobalt nitrate) and ammonia water (32%  $\text{NH}_3$  basis) were used without any further purification and were sourced from Sigma-Aldrich. All of the preparations were conducted in a fume hood at ambient conditions. Each counter ion was evaluated individually; cobalt acetate tetrahydrate was first evaluated, then cobalt chloride hexahydrate and lastly cobalt nitrate hexahydrate. The concentration of the metal salt varied between 0.1 M and 0.5 M. The cobalt salt (measured in grams) was weighed on a balance in a 200 mL glass beaker. The cobalt salt was dissolved in deionised water and placed on a magnetic stirrer for 10 minutes to dissolve the salt. An ammonium hydroxide solution was prepared in a 100 mL beaker and added to the metal salt solution in a dropwise manner using a 100 mL pipet (see Figure 3.1). This solution, now called the precursor, was then stirred for a further 10 minutes. The use of ammonium hydroxide allowed the hydroxyl ions to be utilised (Huang et al., 2014 A 1:3 ratio of  $[\text{Co}^{2+}]:[\text{OH}^-]$  ratio was used for this study (Nassar and Ahmed, 2011). The quantity of cobalt salt dissolved in 40 mL of deionised water and the percentage of ammonium hydroxide in the ammonium hydroxide solution was calculated according to the ratio of 1:3. Table 3.2 shows the quantity of chemicals used under each precursor concentration condition.

**Table 3.2: Chemical quantity used**

Product Description	Precursor concentration		
	0.1 M	0.3 M	0.5 M
Cobalt nitrate hexahydrate ( $\text{Co}(\text{NO}_3)_2 \cdot 6\text{H}_2\text{O}$ )	0.732 g	2.195 g	3.659 g
Cobalt chloride hexahydrate ( $\text{CoCl}_2 \cdot 6\text{H}_2\text{O}$ )	0.952 g	2.853 g	5.622 g
Cobalt acetate tetrahydrate ( $\text{Co}(\text{C}_2\text{H}_3\text{O}_2)_2$ )	0.708 g	2.125 g	3.340 g
Ammonium hydroxide solution ( $\text{NH}_4\text{OH}$ )	1.490 mL	5,090 mL	8.486 mL



**Figure 3.1: Preparation of the cobalt salt precursor**

The precursor solution was then transferred to the 200 mL Teflon-lined pressure vessel and placed inside the oven, as shown in Figure 3.2 . The reaction temperature was varied between 90°C and 180°C with a reaction time varying between 0.5 hours and 6 hours according to the factorial runs presented in Table 3.1 .



**Figure 3.2: 200 mL pressure vessel inside oven**

The oven was switched off after the selected time had been completed and the pressure vessel was left to cool down naturally to room temperature overnight. The cobalt hydroxide solution produced was then transferred from the pressure vessel into a glass beaker. The reaction product was centrifuged twice and then washed three times with deionised water to ensure that pure cobalt hydroxide was obtained. The powders obtained were then dried for 24 hours in the oven at 60°C. The dried black crystallite cobalt oxide (Co<sub>3</sub>O<sub>4</sub>) powders were transferred to porcelain crucibles that were then annealed in a LABOFURN furnace at 350°C for 3 hours; these conditions were kept constant for all the samples. The samples were removed from the furnace and stored in upright sample vials for evaluation as catalysts in the AOP process and for further analysis.

### 3.4. Evaluation of the catalytic efficiency of the produced catalyst

The efficiency of the produced catalyst was assessed by evaluating the degradation of methyl orange over 30 minutes. The methyl orange solution was prepared individually for each experiment by dissolving 0.02 g of methyl orange powder in 500 mL of deionised water. This solution was stirred for 15 minutes on the magnetic stirrer to ensure that the powder was dissolved. The colour was measured against deionised water by means of a handheld Lovibond<sup>®</sup> spectrophotometer. The colour variance of the sample against the selected standard (in this case deionised water) was quantified by the numerical output ( $\Delta E$ ) of the spectrophotometer. Once the original sample was taken, 0.28 g of peroxymonosulphate (Oxone<sup>®</sup>) was added to the solution and 4 mL aliquots samples were taken every 2 minutes. An amount of 0.015 g of Co<sub>3</sub>O<sub>4</sub> nanocatalyst was added to the prepared methyl orange solution. The decision on the quantity of methyl orange, Co<sub>3</sub>O<sub>4</sub> nanocatalyst and Oxone<sup>®</sup> required for the degradation study was based on a study done by Slavova et al. (2014) and Nassar & Ahmed (2012). Equation 3-1 shows the calculation of the percentage degradation of methyl orange. In order not to harm the environment or endanger the health of the other students that is working in the laboratory; once the experiment was done the solution was transferred to a container that was collected by a contracted licensed professional waste disposal service to dispose of the material.

$$\% \text{ Degradation} = (1 - ((\Delta E_{\text{(sample)}})/\Delta E_{\text{(deionised water)}})) * 100 \quad \text{Equation 3-1}$$

### 3.5. Characterisation methods

XRD analysis was conducted to determine the composition of the nanostructures that were synthesised. Samples were taken after calcination to determine if  $\text{Co}_3\text{O}_4$  was produced. For this study a multipurpose X-ray diffractometer D8-Advance from Bruker (Figure 3.3) was used to perform the measurements. It was operated in a continuous  $\theta - \theta$  scan in locked coupled mode with  $\text{Cu-K}\alpha$  radiation. The sample is mounted in the centre of the sample holder on a glass slide and levelled up to the desired height. The measurements run within a range in  $2\theta$  defined by the user with a characteristic step size of  $0.034^\circ$  in  $2\theta$ . A Lyn-Eye (position sensitive detector) is used to record diffraction data at a typical speed of 0.5 sec/step which is equivalent to an effective time of 92 sec/step for a scintillation counter. Data are background subtracted so that the phase analysis is carried out for diffraction pattern with zero background after the selection of a set of possible elements from the periodic table. Phases are identified from the match of the calculated peaks with the measured ones until all phases have been identified within the limits of the resolution of the results.

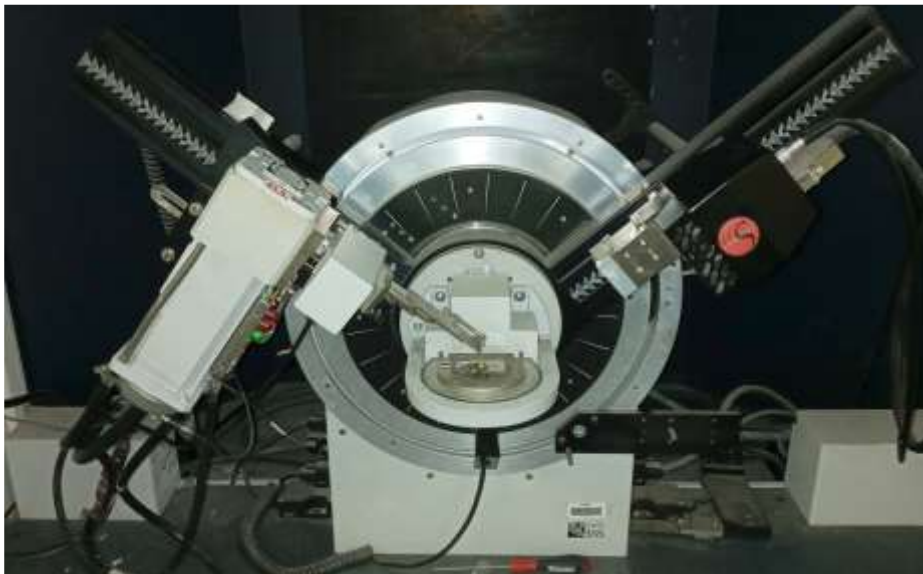


Figure 3.3: Multipurpose X-ray diffractometer D8-Advance (photo provided by Dr R. Bucher)

From the XRD the crystallite size was determined using the Debye-Scherrer formation (Equation 3-2).

$$D = (k\lambda)/(\beta\cos\theta) \quad \text{Equation 3-2}$$

Where  $k = 0.9$ ,  $\lambda$  is the wavelength of the X-ray radiation and  $\beta$  the full width at half of the diffraction peak.

BET analysis was performed to determine the surface area of the produced catalyst. For this study only the best and worst performing catalyst for each cobalt salt precursor were tested for BET.

### **3.6. Conclusions**

The hydrothermal synthesis method was applied for the production of cobalt hydroxide nanostructures and the  $\text{Co}_3\text{O}_4$  was obtained through the calcination method. The catalytic efficiency of the nanocatalyst produced was evaluated by the degradation of methyl orange in an advanced oxidation process. XRD and BET characterisation techniques were used to analyse the produced nanoparticles.

## **Chapter 4      Effect of the process conditions on the product yield and crystallite size**

### **4.1 Introduction**

This chapter discusses how the interaction between the operational process parameters affect the product yield and crystallite size of the produced nanocatalyst. This was evaluated by means of a three level, three factor face-centred central composite design experiment that was set up in Design-Expert™ software. The factorial experimental design was used to statistically identify the degree of interactions between the process parameters. Three parameters were varied during the experimental procedure: reaction temperature, residence time and the concentration of the metal salt. This experimental set-up was repeated for each counter ion. Synthesis of crystalline particles of cobalt hydroxide was achieved hydrothermally using three different types of cobalt salts (cobalt acetate tetrahydrate, cobalt chloride hexahydrate and cobalt nitrate hexahydrate), ammonium hydroxide and water as the solvent, with a molar ratio of 1:3 (cobalt salt: ammonium hydroxide) in an aqueous solution. Table 4.1 shows the yield, crystallite size and the degradation percentage of produced nanocatalyst as a function of the operating parameters.

**Table 4.1: Cobalt oxide nanoparticles produced by means of a cobalt salt precursor**

Run	Temperature	Concentration	Residence Time	Precursor	Yield mass Actual	Yield	Crystallite size	Degradation
	°C	M	h		g	%	nm	%
D1	180	0.3	3.25	Co(NO <sub>3</sub> ) <sub>2</sub> ·6H <sub>2</sub> O	0.59	83.69	13.83	92.95
D2	90	0.1	6	Co(NO <sub>3</sub> ) <sub>2</sub> ·6H <sub>2</sub> O	0.18	89.18	8.5	96.03
D3	135	0.3	6	Co(NO <sub>3</sub> ) <sub>2</sub> ·6H <sub>2</sub> O	1.01	*143.26	amorphous	85.64
D4	135	0.3	3.25	Co(NO <sub>3</sub> ) <sub>2</sub> ·6H <sub>2</sub> O	0.54	76.60	8.72	91.79
D5	90	0.5	0.5	Co(NO <sub>3</sub> ) <sub>2</sub> ·6H <sub>2</sub> O	1.26	*113.62	amorphous	82.44
D6	135	0.3	3.25	Co(NO <sub>3</sub> ) <sub>2</sub> ·6H <sub>2</sub> O	0.54	76.60	8.72	91.79
D7	90	0.3	3.25	Co(NO <sub>3</sub> ) <sub>2</sub> ·6H <sub>2</sub> O	0.26	36.88	7.89	78.85
D8	135	0.3	3.25	Co(NO <sub>3</sub> ) <sub>2</sub> ·6H <sub>2</sub> O	0.50	70.92	8.71	91.79
D9	135	0.3	3.25	Co(NO <sub>3</sub> ) <sub>2</sub> ·6H <sub>2</sub> O	0.68	96.45	8.53	91.79
D10	135	0.3	3.25	Co(NO <sub>3</sub> ) <sub>2</sub> ·6H <sub>2</sub> O	0.69	97.87	amorphous	91.79
D11	135	0.1	3.25	Co(NO <sub>3</sub> ) <sub>2</sub> ·6H <sub>2</sub> O	0.14	69.36	amorphous	82.18
D12	180	0.5	0.5	Co(NO <sub>3</sub> ) <sub>2</sub> ·6H <sub>2</sub> O	1.02	91.97	11.99	92.95
D13	135	0.3	3.25	Co(NO <sub>3</sub> ) <sub>2</sub> ·6H <sub>2</sub> O	0.51	71.91	8.87	91.79
D14	180	0.1	6	Co(NO <sub>3</sub> ) <sub>2</sub> ·6H <sub>2</sub> O	0.18	89.18	8.38	87.31
D15	90	0.1	0.5	Co(NO <sub>3</sub> ) <sub>2</sub> ·6H <sub>2</sub> O	0.17	81.74	12.33	96.15
D16	90	0.5	6	Co(NO <sub>3</sub> ) <sub>2</sub> ·6H <sub>2</sub> O	0.88	79.35	6.85	87.18
D17	135	0.5	3.25	Co(NO <sub>3</sub> ) <sub>2</sub> ·6H <sub>2</sub> O	1.04	93.78	6.35	93.33
D18	180	0.5	6	Co(NO <sub>3</sub> ) <sub>2</sub> ·6H <sub>2</sub> O	0.98	88.37	10.94	90.9
D19	135	0.3	0.5	Co(NO <sub>3</sub> ) <sub>2</sub> ·6H <sub>2</sub> O	0.65	92.20	7.9	81.47
D20	180	0.1	0.5	Co(NO <sub>3</sub> ) <sub>2</sub> ·6H <sub>2</sub> O	0.18	89.18	21.22	94.74
C21	180	0.3	3.25	CoCl <sub>12</sub> ·6H <sub>6</sub> O	0.22	22.92	14.703	75.64
C22	90	0.1	6	CoCl <sub>12</sub> ·6H <sub>6</sub> O	0.01	2.68	10.56	91.67
C23	135	0.3	6	CoCl <sub>12</sub> ·6H <sub>6</sub> O	0.42	43.75	8.137	80.26

C24	135	0.3	3.25	CoCl <sub>12</sub> 6H <sub>6</sub> O	0.21	21.88	3.06	80.26
C25	90	0.5	0.5	CoCl <sub>12</sub> 6H <sub>6</sub> O	0.91	48.05	17.97	66.92
C26	135	0.3	3.25	CoCl <sub>12</sub> 6H <sub>6</sub> O	0.98	*102.08	17.148	80.26
C27	90	0.3	3.25	CoCl <sub>12</sub> 6H <sub>6</sub> O	0.10	10.42	4.01	88.46
C28	135	0.3	3.25	CoCl <sub>12</sub> 6H <sub>6</sub> O	0.94	97.92	4.007	80.26
C29	135	0.3	3.25	CoCl <sub>12</sub> 6H <sub>6</sub> O	0.21	21.88	4.013	80.26
C30	135	0.3	3.25	CoCl <sub>12</sub> 6H <sub>6</sub> O	0.35	36.46	4.046	80.26
C31	135	0.1	3.25	CoCl <sub>12</sub> 6H <sub>6</sub> O	0.00	1.07	4.98	85.26
C32	180	0.5	0.5	CoCl <sub>12</sub> 6H <sub>6</sub> O	1.59	83.95	9.195	80.13
C33	135	0.3	3.25	CoCl <sub>12</sub> 6H <sub>6</sub> O	0.19	19.79	4.01	80.26
C34	180	0.1	6	CoCl <sub>12</sub> 6H <sub>6</sub> O	1.86	*180.00	17.148	76.79
C35	90	0.1	0.5	CoCl <sub>12</sub> 6H <sub>6</sub> O	0.18	48.32	14.049	88.97
C36	90	0.5	6	CoCl <sub>12</sub> 6H <sub>6</sub> O	0.42	22.18	17.145	69.62
C37	135	0.5	3.25	CoCl <sub>12</sub> 6H <sub>6</sub> O	0.23	12.14	11.7	64.49
C38	180	0.5	6	CoCl <sub>12</sub> 6H <sub>6</sub> O	1.45	76.56	11.12	74.87
C39	135	0.3	0.5	CoCl <sub>12</sub> 6H <sub>6</sub> O	0.63	65.63	10.5	65.51
C40	180	0.1	0.5	CoCl <sub>12</sub> 6H <sub>6</sub> O	0.20	53.69	17.149	74.23
A41	180	0.3	3.25	Co(C <sub>2</sub> H <sub>3</sub> O <sub>2</sub> ) <sub>2</sub>	0.48	69.34	13.826	54.62
A42	90	0.1	6	Co(C <sub>2</sub> H <sub>3</sub> O <sub>2</sub> ) <sub>2</sub>	0.15	64.50	6.998	65.51
A43	135	0.3	6	Co(C <sub>2</sub> H <sub>3</sub> O <sub>2</sub> ) <sub>2</sub>	0.43	62.04	13.2826	71.28
A44	135	0.3	3.25	Co(C <sub>2</sub> H <sub>3</sub> O <sub>2</sub> ) <sub>2</sub>	0.35	50.66	8.7147	55.13
A45	90	0.5	0.5	Co(C <sub>2</sub> H <sub>3</sub> O <sub>2</sub> ) <sub>2</sub>	0.41	38.03	4.156	69.1
A46	135	0.3	3.25	Co(C <sub>2</sub> H <sub>3</sub> O <sub>2</sub> ) <sub>2</sub>	0.35	50.66	8.7147	55.13
A47	90	0.3	3.25	Co(C <sub>2</sub> H <sub>3</sub> O <sub>2</sub> ) <sub>2</sub>	0.25	36.64	7.895	63.33
A48	135	0.3	3.25	Co(C <sub>2</sub> H <sub>3</sub> O <sub>2</sub> ) <sub>2</sub>	0.43	62.04	8.7147	55.13
A49	135	0.3	3.25	Co(C <sub>2</sub> H <sub>3</sub> O <sub>2</sub> ) <sub>2</sub>	0.26	37.96	8.7147	55.13
A50	135	0.3	3.25	Co(C <sub>2</sub> H <sub>3</sub> O <sub>2</sub> ) <sub>2</sub>	0.35	50.66	8.7147	55.13
A51	135	0.1	3.25	Co(C <sub>2</sub> H <sub>3</sub> O <sub>2</sub> ) <sub>2</sub>	0.05	20.62	9.3289	55.64
A52	180	0.5	0.5	Co(C <sub>2</sub> H <sub>3</sub> O <sub>2</sub> ) <sub>2</sub>	0.41	38.03	11.999	59.36

A53	135	0.3	3.25	Co(C <sub>2</sub> H <sub>3</sub> O <sub>2</sub> ) <sub>2</sub>	0.35	50.66	8.7147	55.13
A54	180	0.1	6	Co(C <sub>2</sub> H <sub>3</sub> O <sub>2</sub> ) <sub>2</sub>	0.11	49.58	8.377	58.72
A55	90	0.1	0.5	Co(C <sub>2</sub> H <sub>3</sub> O <sub>2</sub> ) <sub>2</sub>	0.12	51.34	12.325	75.87
A56	90	0.5	6	Co(C <sub>2</sub> H <sub>3</sub> O <sub>2</sub> ) <sub>2</sub>	0.16	14.41	6.8451	69.1
A57	135	0.5	3.25	Co(C <sub>2</sub> H <sub>3</sub> O <sub>2</sub> ) <sub>2</sub>	0.06	5.86	6.3489	64.1
A58	180	0.5	6	Co(C <sub>2</sub> H <sub>3</sub> O <sub>2</sub> ) <sub>2</sub>	0.13	11.72	10.935	71.15
A59	135	0.3	0.5	Co(C <sub>2</sub> H <sub>3</sub> O <sub>2</sub> ) <sub>2</sub>	0.26	37.96	7.1831	73.85
A60	180	0.1	0.5	Co(C <sub>2</sub> H <sub>3</sub> O <sub>2</sub> ) <sub>2</sub>	0.16	69.33	21.22	71.03

## 4.2 Effect of process conditions on precursor complex solution, cobalt hydroxide and cobalt oxide

Samples were produced under various process conditions, as specified by the factorial trial. Only calcined samples were analysed using X-ray diffraction to ascertain the type of cobalt oxide formed by plotting the angular positions ( $2\theta$ ) against their resulting intensities. The XRD patterns for salt 1, salt 2 and salt 3 for all the process conditions are presented in Figures 4.1 to 4.3 for the calcined powders produced.

A precursor made up of cobalt acetate tetrahydrate and ammonium hydroxide were red before the hydrothermal synthesis process while a precursor made up of cobalt chloride hexahydrate with ammonium hydroxide and cobalt nitrate hexahydrate with ammonium hydroxide both were green.

### 4.2.1 Samples obtained after hydrothermal synthesis

A precursor made up of cobalt acetate tetrahydrate and ammonium hydroxide were red before the hydrothermal synthesis process while a precursor made up of cobalt chloride hexahydrate with ammonium hydroxide and cobalt nitrate hexahydrate with ammonium hydroxide both were green. During the hydrothermal synthesis process the reactions stipulated in Equation 4-1 to Equation 4-3 takes place for each precursor respectively.



After hydrothermal synthesis, samples produced with cobalt acetate precursor before calcination had a pink/brown colour. It was found that for both cobalt chloride hexahydrate and cobalt nitrate hexahydrate precursors produced samples with a green/blue colour. El-Batlouni et al. (2008) and Al-Ghoul et al. (2010) stated that cobaltous hydroxide crystallises into two polymorphs with hexagonal layered structures that are denoted as alpha ( $\alpha$ )- and beta ( $\beta$ )- $\text{Co}(\text{OH})_2$  that are recognised by their blue/green and pink colours respectively. Considering the hydrothermal synthesis using cobalt acetate tetrahydrate – this concurs with similar experiments done by Folkman et al. (2018) and Stadnik et al. (2017) using a cobalt acetate tetrahydrate precursor. It was found that  $\beta$ - $\text{Co}(\text{OH})_2$  hydroxide was produced using this

precursor. According to El-Batlouni, et al. (2008), pink colored  $\beta$ -Co(OH)<sub>2</sub> has a brucite-like structure where the divalent cobalt and hydroxide ions (that are coordinated in octahedral sites) form charge-neutral layers stacked one over the other. A crystallographic study on this polymorph showed that there are no intercalated species present between the charge-neutral layers and it has an interlayer spacing of 4.6Å.

The blue/green  $\alpha$ -Co(OH)<sub>2</sub> was found to exhibit a hydrotalcite-like structure that consists of positively charged layers that are separated by charge-balancing anions and water molecules. The positive charge of  $\alpha$ -Co(OH)<sub>2</sub> is acquired by partial protonation of the hydroxyl ions. It was found that there is a substantial increase in the interlayer spacing (greater than 7 Å depending on the intercalated anion species) due to the intercalation of anions (El-Batlouni et al., 2008). This phenomenon was confirmed by a study by Heuvel (2020) on the effect of precursor anions in alcohol/water solutions during hydro/solvothermal synthesis on cobalt oxide morphology and catalytic ability.

#### 4.2.2 Samples obtained after calcination

The cobalt hydroxide was subsequently calcined at 350°C for 3 hours and the resulting powders were analysed using high-energy synchrotron x-ray diffraction technique to firstly establish the purity, and secondly the estimation of the crystallite size using the Debye-Scherrer formula. The reaction that occurs during the calcination process can be seen in Equation 4-4 (Huang et al., 2014).

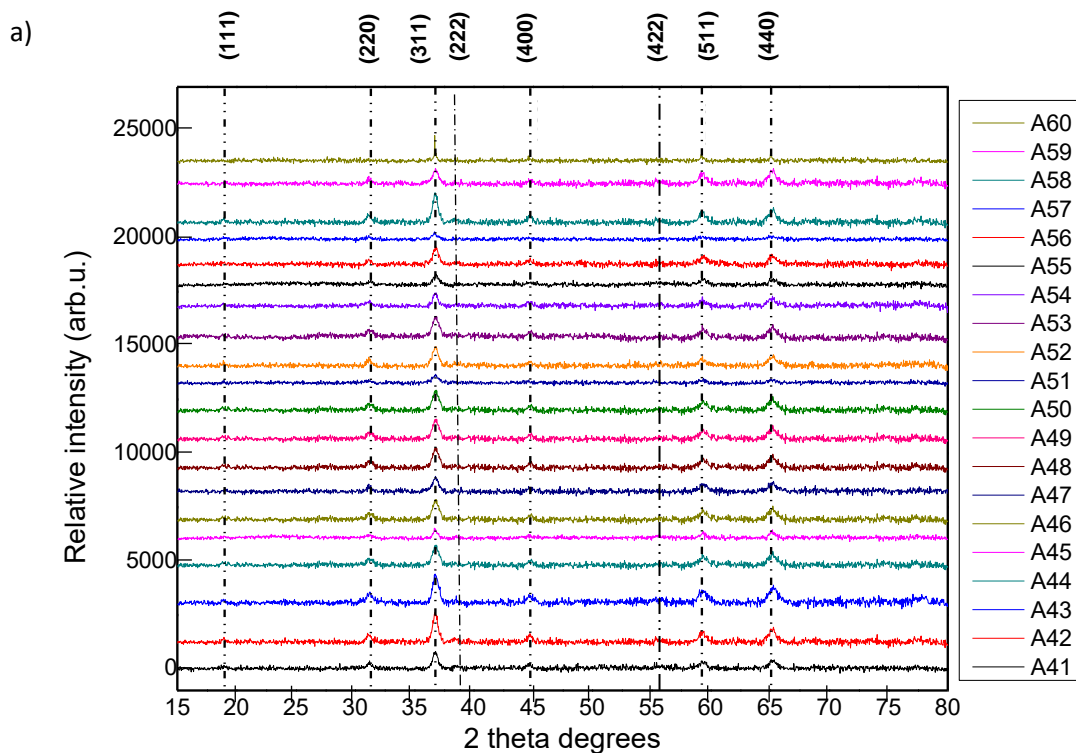


The percentage yield was calculated using Equation 4-5 where the actual yield refers to the yield that was measured after every physical experiment that was done and the theoretical yield was calculated using chemistry principals. From Table 4.1 it can be seen that some experimental runs have yield percentages that is higher than 100%, this is due to experimental error.

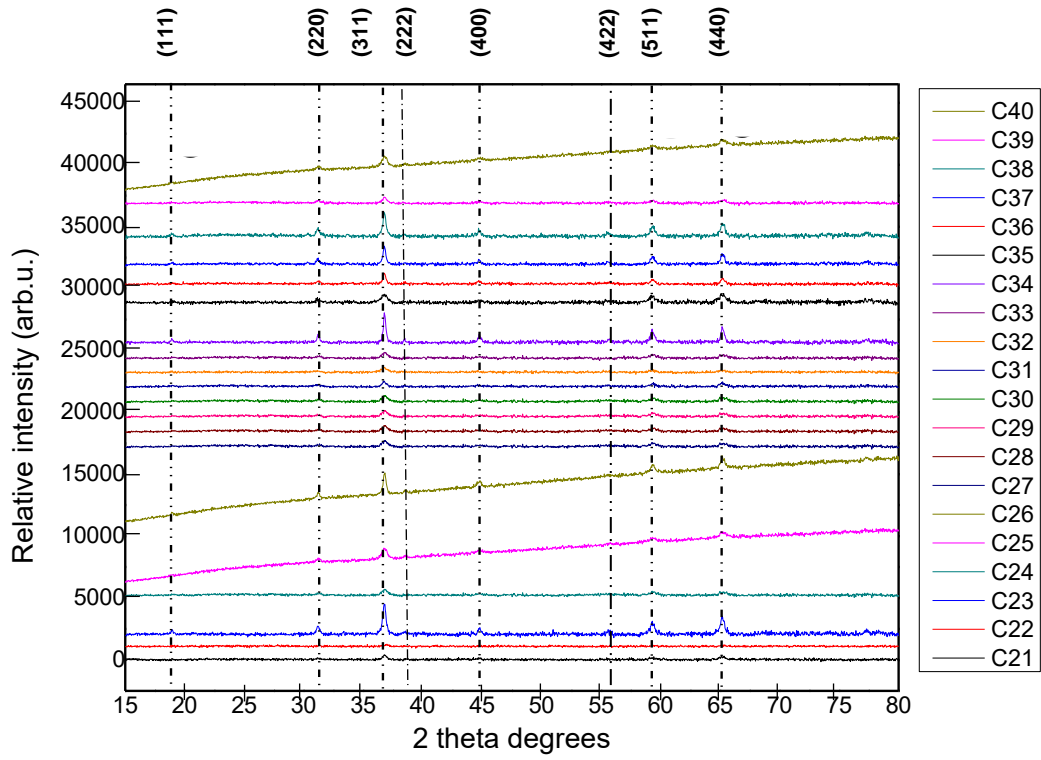
$$\% \text{ Yield} = \left( \frac{\text{Actual yield}}{\text{Theoretical yield}} \right) * 100 \quad \text{Equation 4-5}$$

The X-ray diffraction (XRD) patterns for powders produced by cobalt acetate tetrahydrate, cobalt chloride hexahydrate and cobalt nitrate hexahydrate precursor salts can be seen below, respectively.

Figure 4.1 shows that the peaks represented are in accordance with the JCPDS card 42-1467 for  $\text{Co}_3\text{O}_4$ , which exhibits diffraction peaks at  $19^\circ$ ,  $31.3^\circ$ ,  $36.9^\circ$ ,  $38.6^\circ$ ,  $44.8^\circ$ ,  $55.7^\circ$ ,  $59.4^\circ$  and  $65.2^\circ$ , indexed to (111), (220), (311), (222), (400), (422), (511) and (440). The X-ray diffraction (XRD) patterns for powders produced by cobalt acetate tetrahydrate (Figure 4.1 a), cobalt chloride hexahydrate (Figure 4.1 b) and cobalt nitrate hexahydrate (Figure 4.1 c) precursor salts can be seen below, respectively. Samples produced by cobalt chloride hexahydrate additional peaks were observed on the XRD pattern (Figure 4.1 b). These unidentified peaks match Cobalt Hydroxide Chloride ( $\text{Co}_2(\text{OH})_3\text{Cl}$ ). For samples produced by cobalt nitrate hexahydrate precursor salt it was found that the following samples for cobalt nitrate hexahydrate precursor were amorphous: D3, D5, D10 and D11. The lack of the diffraction peaks implies that these are non-crystalline materials.



b)



c)

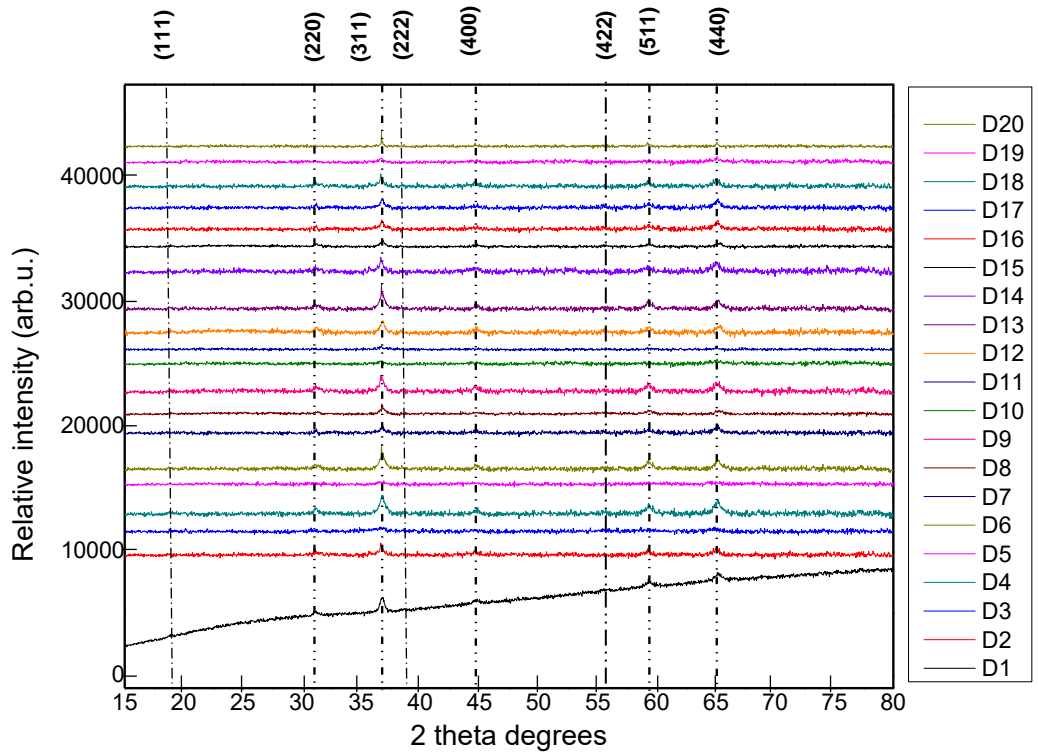


Figure 4.1: XRD patterns results for  $\text{Co}_3\text{O}_4$  nanoparticles produced by a) cobalt acetate tetrahydrate, b) cobalt chloride hexahydrate and c) cobalt nitrate hexahydrate precursors

### 4.3 The effect of operating parameters on the yield and crystallite size of the produced nanocatalyst

Design-Expert software was used for the experimental planning, to analyse the effect of the operating parameters on the  $\text{Co}_3\text{O}_4$  nanostructures produced and to derive the yield and grain size prediction models. For both the yield prediction model and the grain size prediction model a backward stepwise regression procedure (with Alpha = 0.15) was selected to determine which factors are significant and should be included in the quadratic model.

Using a cobalt acetate tetrahydrate ( $\text{Co}(\text{C}_2\text{H}_3\text{O}_2)_2$ ) precursor salt the highest yield (66%) was obtained from the following conditions: 180°C, 0.2 M and 6 h; cobalt chloride hexahydrate ( $\text{CoCl}_{12}\cdot 6\text{H}_2\text{O}$ ) produced the highest yield (82%) at the following conditions: 180°C, 0.3 M and 30 minutes; and cobalt nitrate hexahydrate ( $\text{Co}(\text{NO}_3)_2\cdot 6\text{H}_2\text{O}$ ) precursor salt obtained the highest yield (100%) from the following conditions: 132.3°C, 0.3 M and 30 minutes.

The most desirable model was found by using a quadratic model and selecting the significant factors by using the p-method. The non-hierarchical model found the following active factors: A, D, AD, BD,  $B^2$ ,  $C^2$  where A is the temperature, B is the concentration, C is the residence time and D is the precursor salt, respectively. The ANOVA results for the product yield is given in Table 4.2.

The probability for significance of the model was found to be smaller than 0.0001, thus making the model significant at a 5% significance level (Hassanzadeh et al., 2017; Nautiyal & Shukla, 2018; Noordin et al., 2004; Nautiyal & Shukla, 2018). The p-value is the probability of seeing the observed F-value or larger if the null-hypothesis is true. Small p-values reject the hypothesis of zero effect. The F-value for significance of the model is 8.69 with  $p < 0.0001$ , which shows a good fit. The adjusted coefficient of determination ( $\text{Adj.}R^2$ ), which is the correlation between the observed and predicted values, in this case 0.5399 indicates a reasonable model fit.

Table 4.2: Analysis of variance table for product yield

Source	Sum of Squares	Degrees of freedom	Mean Square	F-value	p-value
<b>Model</b>	36336.42	9	4037.38	8.69	< 0.0001
<b>A-Temperature</b>	2616.34	1	2616.34	5.63	0.0215
<b>D-Precursor</b>	24115.41	2	12057.70	25.96	< 0.0001
<b>AD</b>	1888.03	2	944.01	2.03	0.1417
<b>BD</b>	2415.71	2	1207.86	2.60	0.0843
<b>B<sup>2</sup></b>	2842.26	1	2842.26	6.12	0.0168
<b>C<sup>2</sup></b>	5134.54	1	5134.54	11.05	0.0017
<b>Residual</b>	23223.68	50	464.47		
<b>Lack of Fit</b>	14503.13	35	414.38	0.7128	0.8001
<b>Pure Error</b>	8720.55	15	581.37		
<b>Cor Total</b>	59560.10	59			

The diagnostic analysis was conducted to investigate the validity of the fit of the proposed model. Figure 4.2 shows the normal plot of the residuals. The normal probability plot is approximately linear and supports the condition that the error terms are normally distributed. The observed outliers are due to the samples with a yield percentage higher than 100%. This supports significance of the model.

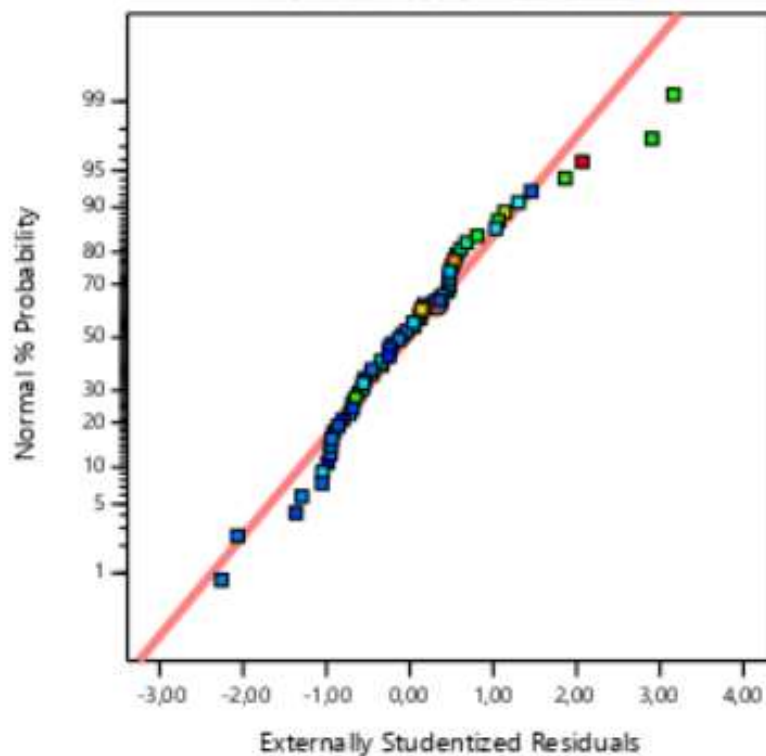


Figure 4.2: Normal plot of residuals

The prediction models for product yield and crystallite size can be seen in Equation 4-6 - Equation 4-8, respectively where A is the temperature, B is the concentration and C is the residence time.

*Yield Cobalt nitrate hexahydrate (%)* Equation 4-6

$$= 65,60788 + 0,092480 A + 34,52358 B - 20,82098 B^2 + 0,031061 C^2$$

*Yield Cobalt chloride hexahydrate (%)* Equation 4-7

$$= -23,88167 + 0,456599 A + 28,84390 B - 20,82098 B^2 + 0,031061 C^2$$

*Yield Cobalt acetate tetrahydrate (%)* Equation 4-8

$$= 54,53441 + 0,073501 A - 63,36748 B - 20,82098 B^2 + 0,031061 C^2$$

The prediction models (hierarchically corrected) for crystallite size can be seen in Equation 4-9 - Equation 4-11. The ANOVA results for the crystallite size that was obtained from the CCD design analysis can be found in Table 4.3. The F-value for significance of the model is 35.69 with  $p < 0.0001$ , which shows a good fit. The adjusted coefficient of determination ( $Adj.R^2$ ), which is the correlation between the observed and predicted values, in this case 0.574 indicates a reasonable model fit.

Table 4.3: Analysis of variance table for crystallite size

Source	Sum of Squares	Degrees of freedom	Mean Square	F-value	p-value
<b>Model</b>	784.01	23	34.09	4.46	< 0.0001
<b>A-Temperature</b>	121.44	1	121.44	15.88	0.0003
<b>B-Concentration</b>	38.99	1	38.99	5.1	0.0301
<b>C-Residence Time</b>	22.25	1	22.25	2.91	0.0967
<b>D-Precursor</b>	4.31	2	2.15	0.2815	0.7563
<b>AB</b>	16.12	1	16.12	2.11	0.1552
<b>AC</b>	13.19	1	13.19	1.72	0.1975
<b>AD</b>	31.82	2	15.91	2.08	0.1397
<b>BC</b>	75.99	1	75.99	9.93	0.0033
<b>BD</b>	32.28	2	16.14	2.11	0.1359
<b>A<sup>2</sup></b>	41	1	41	5.36	0.0264
<b>B<sup>2</sup></b>	0.1256	1	0.1256	0.0164	0.8988
<b>C<sup>2</sup></b>	25.29	1	25.29	3.31	0.0773
<b>ABD</b>	60.43	2	30.22	3.95	0.0281
<b>A<sup>2</sup>C</b>	36.76	1	36.76	4.81	0.0349
<b>AB<sup>2</sup></b>	22.93	1	22.93	3	0.0919
<b>B<sup>2</sup>D</b>	90.64	2	45.32	5.93	0.006
<b>AB<sup>2</sup>D</b>	34.68	2	17.34	2.27	0.1182
<b>Residual</b>	275.35	36	7.65		
<b>Lack of Fit</b>	126.37	21	6.02	0.6059	0.8576
<b>Pure Error</b>	148.99	15	9.93		
<b>Cor Total</b>	1059.36	59			

The prediction models (hierarchically corrected) for product yield and crystallite size can be seen in Equation 4-9 – Equation 4-11, respectively where A: Temperature, B: Concentration and C: Residence time:

Equation 4-9

$$\begin{aligned} & \text{Crystallite size nitrate hexahydrate} \\ & = 51.89184 - 0.680162A - 17.32126B - 10.23216C + 0.171389AB \\ & + 0.128193AC + 3.23523BC + 0.002716A^2 - 14.76375B^2 + 0.231506C^2 \\ & - 0.000497A^2C - 0.212500AB^2 \end{aligned}$$

Equation 4-10

$$\begin{aligned} & \text{Crystallite size cobalt chloride hexahydrate} \\ & = 75.07984 - 0.792301A - 282.57726B - 10.23216C + 1.65506AB \\ & + 0.128193AC + 3.2353BC + 0.002716A^2 + 532.66625B^2 + 0.231506C^2 \\ & - 0.000497A^2C - 3.32528AB^2 \end{aligned}$$

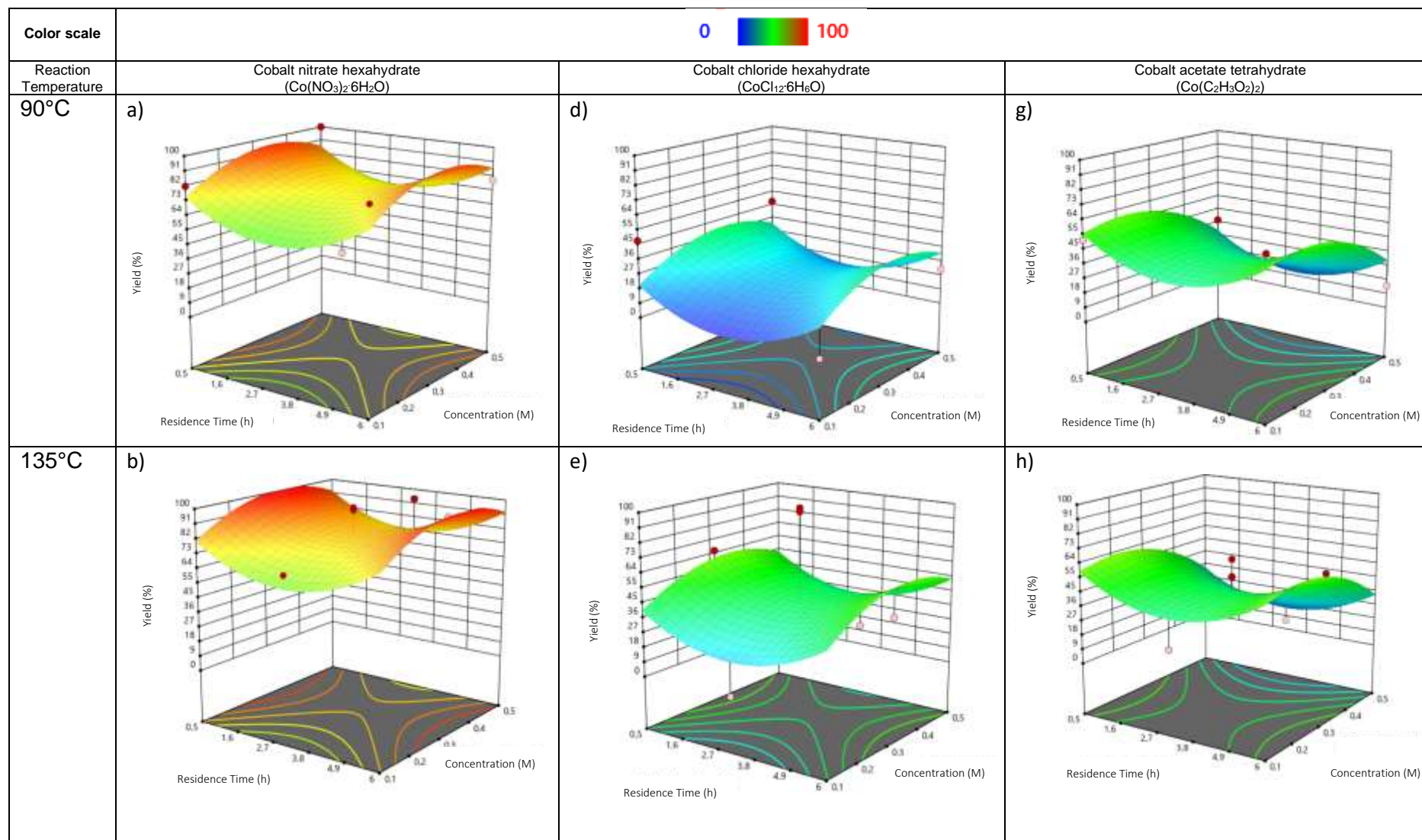
Equation 4-11

$$\begin{aligned} & \text{Crystallite size cobalt acetate tetrahydrate} \\ & = 51.07592 - 0.66465A - 1.40734B - 10.23216C + 0.086253AB \\ & + 0.128193AC + 3.23523BC + 0.002716A^2 - 35.33344B^2 + 0.231506C^2 \\ & - 0.000497A^2C - 0.105354AB^2 \end{aligned}$$

### 4.3.1 Effect of process parameters on the yield of produced nanocatalyst

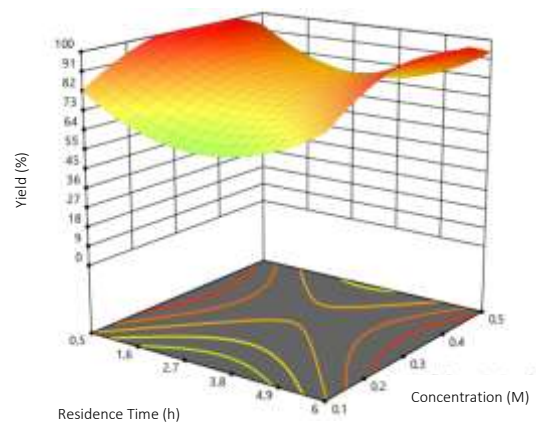
The effect of temperature was evaluated by observing the effect on the reaction yield in a temperature range of 90°C – 180°C, with the precursor concentration ranging between 0.1 M and 0.5 M and a residence time between 30 minutes and 6 hours. The Co<sub>3</sub>O<sub>4</sub> nanoparticle product yield as a response to changes in the reaction temperature for precursor salts: cobalt nitrate hexahydrate (Co(NO<sub>3</sub>)<sub>2</sub>·6H<sub>2</sub>O), cobalt chloride hexahydrate (CoCl<sub>2</sub>·6H<sub>2</sub>O) and cobalt acetate tetrahydrate (Co(C<sub>2</sub>H<sub>3</sub>O<sub>2</sub>)<sub>2</sub>) can be seen in Table 4.4.

**Table 4.4: The product yield as a response of the interaction between residence time and precursor concentration at a reaction temperature of a) 90°C, b) 135°C and c) 180°C.**

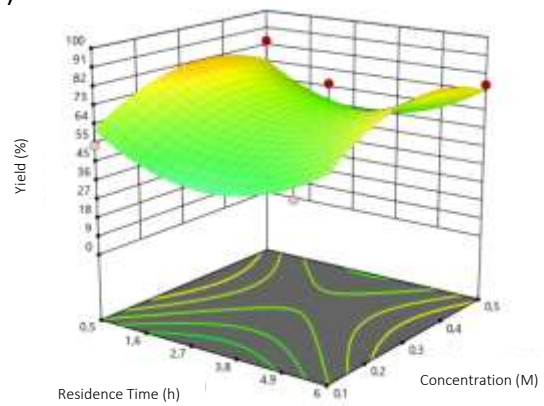


180°C

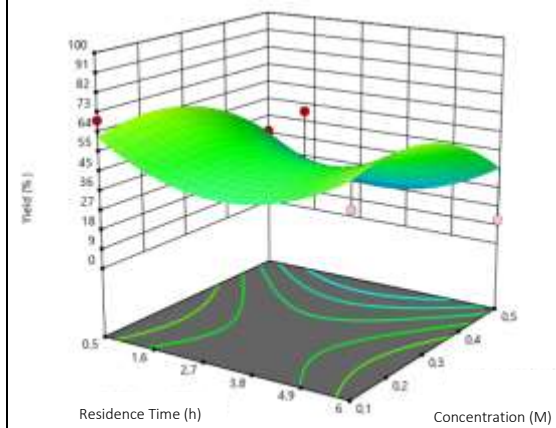
c)



f)



i)



The effect of the reaction temperature on the product yield of  $\text{Co}(\text{NO}_3)_2 \cdot 6\text{H}_2\text{O}$ -derived  $\text{Co}_3\text{O}_4$  nanoparticles is given in Table 4.4 a - c. The product yield of  $\text{Co}(\text{NO}_3)_2 \cdot 6\text{H}_2\text{O}$ -derived  $\text{Co}_3\text{O}_4$  nanoparticles increased with an increase in the reaction temperature. An increase in the product yield is observed as the precursor concentration increased from 0.1 M to 0.3 M and decreased between 0.3 M and 0.5 M. At a precursor concentration of 0.3 M there is a maximum in the yield percentage; this is found across the reaction temperature and residence time range. Across the reaction temperature there is a maximum found at a precursor concentration of 0.5 M and residence time of 30 minutes. There is an overall increase in the product yield as the precursor concentration increases from 0.1 M to 0.5 M at the lowest residence time. A minimum is found at 3.25 hours over the residence time range. Across the temperature range the product yield has been found to increase as the residence time increases from 30 minutes to 6 hours. As a result of the interaction between the reaction temperature, precursor concentration and residence time, the highest product yield was obtained at the following conditions: 132.3°C, 0.3 M and 30 minutes, while the lowest product yield was found at 90°C, 0.1 M and 3.4 hours. The yield ranged between 56.00% and 100.00%.

The effect of the reaction temperature on the product yield of  $\text{CoCl}_2 \cdot 6\text{H}_2\text{O}$ -derived  $\text{Co}_3\text{O}_4$  nanoparticles is given in Table 4.4 d - f. For  $\text{CoCl}_2 \cdot 6\text{H}_2\text{O}$ -derived  $\text{Co}_3\text{O}_4$  nanoparticles, a similar trend was observed as in the case of the  $\text{Co}(\text{NO}_3)_2 \cdot 6\text{H}_2\text{O}$ -derived  $\text{Co}_3\text{O}_4$ . It was found that the yield increased with increasing reaction temperature. An increase in the product yield is observed as the precursor concentration form 0.1 M to 0.3 M and decreased between 0.3 M and 0.5 M. At a precursor concentration of 0.3 M there is a maximum in the yield percentage. Across the reaction temperature there is a maximum seen at a precursor concentration of 0.5 M and residence time of 30 minutes. An increase in the precursor concentration from 0.1 M to 0.5 M resulted in an increase in the product yield. As the residence time is increased from 30 minutes to 3.25 hours a decrease in the product yield and an increase is observed in the product yield as the residence time increases from 3.25 hours to 6 hours. Across the temperature range the product yield has been found to increase as the residence time increases from 30 minutes to 6 hours. At a residence time of 3.25 a minimum is observed. This phenomenon is observed across the reaction temperature – and precursor concentration range. In terms of production, it is good to know that the high yields can be obtained at the low residence times. This is the advantage of understanding the process parameter interactions. The highest product yield was obtained at the following conditions: 180°C, 0.3 M and 30 minutes, while the lowest product yield was found at 90°C, 0.1 M and 3.5 hours. The yield ranged between 1.00% and 82.00%.

The effect of the reaction temperature on the product yield of  $\text{Co}(\text{C}_2\text{H}_3\text{O}_2)_2$ -derived  $\text{Co}_3\text{O}_4$  nanoparticles is given in Table 4.4 g - i. For the  $\text{Co}(\text{C}_2\text{H}_3\text{O}_2)_2$ -derived  $\text{Co}_3\text{O}_4$  product yield it was found that the reaction temperature and residence time has the same effect as for the product yield for  $\text{Co}(\text{NO}_3)_2 \cdot 6\text{H}_2\text{O}$ - and  $\text{CoCl}_{12} \cdot 6\text{H}_6\text{O}$ -derived  $\text{Co}_3\text{O}_4$  nanoparticles. The product yield of  $\text{Co}(\text{C}_2\text{H}_3\text{O}_2)_2$ -derived  $\text{Co}_3\text{O}_4$  nanoparticles increased with an increase in the reaction temperature. As precursor concentration from 0.1 M to 0.3 M an increase in the product yield is observed while there is a decrease between 0.3 M and 0.5 M. The increase in the precursor concentration from 0.1 M to 0.5 M resulted in a decrease in the product yield. This contradicts the response of the  $\text{Co}_3\text{O}_4$  yield obtained from the  $\text{Cl}_2\text{CoH}_{12}\text{O}_6$  and  $\text{Co}(\text{NO}_3)_2 \cdot 6\text{H}_2\text{O}$  precursor salts. At a precursor concentration of 0.3 M there is a maximum in the yield percentage. As the residence time is increased from 30 minutes to 3.25 hours, there is a decrease in the product yield and an increase is observed in the product yield as the residence time increases from 3.25 hours to 6 hours; this is seen at higher precursor concentrations. At low precursor concentrations there is a decrease in the product yield as the residence time increases from 30 minutes to 6 hours. The highest product yield was obtained at the following conditions:  $180^\circ\text{C}$ , 0.2 M and 6 hours, while the lowest product yield was found at  $94^\circ\text{C}$ , 0.5 M and 3.5 hours. The yield ranged between 12.00% and 66.00%.

A comparison of the optimum operating parameters to obtain the maximum yield for each precursor is presented in Table 4.5. The product yield for  $\text{Co}(\text{NO}_3)_2 \cdot 6\text{H}_2\text{O}$  -,  $\text{CoCl}_{12} \cdot 6\text{H}_6\text{O}$  - and  $\text{Co}(\text{C}_2\text{H}_3\text{O}_2)_2$  - derived  $\text{Co}_3\text{O}_4$  was found to increase as the reaction temperature and residence time is increased.  $\text{Co}(\text{NO}_3)_2 \cdot 6\text{H}_2\text{O}$  - and  $\text{CoCl}_{12} \cdot 6\text{H}_6\text{O}$ - derived  $\text{Co}_3\text{O}_4$  product yield increased with an increase in the precursor concentration while the product yield for  $\text{Co}(\text{C}_2\text{H}_3\text{O}_2)_2$  - derived  $\text{Co}_3\text{O}_4$  decreased.  $\text{CoCl}_{12} \cdot 6\text{H}_6\text{O}$  - and  $\text{Co}(\text{C}_2\text{H}_3\text{O}_2)_2$  - derived  $\text{Co}_3\text{O}_4$  requires the highest reaction temperature to achieve the maximum product yield. The maximum product yield for  $\text{Co}(\text{NO}_3)_2 \cdot 6\text{H}_2\text{O}$  -derived  $\text{Co}_3\text{O}_4$  requires intermediate reaction temperature.  $\text{Co}(\text{NO}_3)_2 \cdot 6\text{H}_2\text{O}$  - and  $\text{CoCl}_{12} \cdot 6\text{H}_6\text{O}$  -derived  $\text{Co}_3\text{O}_4$  require intermediate precursor concentration and minimum residence time to achieve the highest product yield, while  $\text{Co}(\text{C}_2\text{H}_3\text{O}_2)_2$  - derived  $\text{Co}_3\text{O}_4$  require a low precursor concentration and high residence time. It was found that the residence time had a smaller contribution to the product yield in comparison with the other two precursors. The product yield for all three precursor salts increased as the reaction temperature increased from  $90^\circ\text{C}$  to  $180^\circ\text{C}$ . For  $\text{Co}(\text{NO}_3)_2 \cdot 6\text{H}_2\text{O}$ - and  $\text{CoCl}_{12} \cdot 6\text{H}_6\text{O}$  -derived  $\text{Co}_3\text{O}_4$  there is an increase in the product yield as the precursor concentration increases from 0.1 M to 0.5M while the increase in precursor concentration resulted in a decrease of the product yield for  $\text{Co}(\text{C}_2\text{H}_3\text{O}_2)_2$  -derived  $\text{Co}_3\text{O}_4$  nanoparticles.

Co(C<sub>2</sub>H<sub>3</sub>O<sub>2</sub>)<sub>2</sub> precursor resulted in the lowest product yield, while the highest product yield was obtained by using the Co(NO<sub>3</sub>)<sub>2</sub>·6H<sub>2</sub>O precursor.

Co(NO<sub>3</sub>)<sub>2</sub>·6H<sub>2</sub>O precursor achieved a 18.00% higher product yield than CoCl<sub>12</sub>·6H<sub>6</sub>O. Co(NO<sub>3</sub>)<sub>2</sub>·6H<sub>2</sub>O precursor achieved a 34.00% higher product yield than Co(C<sub>2</sub>H<sub>3</sub>O<sub>2</sub>)<sub>2</sub>-derived Co<sub>3</sub>O<sub>4</sub> at a 0.1 M higher precursor concentration requirement. CoCl<sub>12</sub>·6H<sub>6</sub>O -derived Co<sub>3</sub>O<sub>4</sub> had a 16.00% higher product yield than Co(C<sub>2</sub>H<sub>3</sub>O<sub>2</sub>)<sub>2</sub> - derived Co<sub>3</sub>O<sub>4</sub> with a 0.1 M higher precursor concentration and a 5.5 hours shorter residence time. In evaluating the product yield for all three precursors, Co(NO<sub>3</sub>)<sub>2</sub>·6H<sub>2</sub>O precursor performed the best. Comparing the quantity of cobalt that was present in the precursor salt it was found that cobalt chloride hexahydrate contained the highest percentage of cobalt in the compound (25%) while cobalt nitrate hexahydrate had 20% and cobalt acetate tetrahydrate had 24%. The amount of cobalt that was present in the cobalt salt was not directly related to the final yield of Co<sub>3</sub>O<sub>4</sub>.

**Table 4.5: Operating parameters for maximum Co(OH)<sub>2</sub> to Co<sub>3</sub>O<sub>4</sub> production yield**

Precursor Salt	Reaction Temperature (°C)	Precursor Concentration (M)	Residence time (h)	Yield (%)
Cobalt nitrate hexahydrate (Co(NO <sub>3</sub> ) <sub>2</sub> ·6H <sub>2</sub> O)	132.3	0.3	0.5	100
Cobalt chloride hexahydrate (CoCl <sub>12</sub> ·6H <sub>6</sub> O)	180	0.3	0.5	82
Cobalt acetate tetrahydrate(Co(C <sub>2</sub> H <sub>3</sub> O <sub>2</sub> ) <sub>2</sub> )	180	0.2	6	66

It was found that as the reaction temperature increased the solubility of cobalt hydroxide in the solution decreased, promoting the precipitation of the particles. This concurs with the behaviour observed with Co(NO<sub>3</sub>)<sub>2</sub>·6H<sub>2</sub>O-, CoCl<sub>12</sub>·6H<sub>6</sub>O - and Co(C<sub>2</sub>H<sub>3</sub>O<sub>2</sub>)<sub>2</sub>-derived Co<sub>3</sub>O<sub>4</sub>. Very little research has been done on the product yield of Co<sub>3</sub>O<sub>4</sub>. A study was conducted on the effect of process parameters on the product yield of transition metals by Kriedemann & Fester (2015) on the production of α-Fe<sub>2</sub>O<sub>3</sub> within a reaction temperature range of 250°C - 350°C and precursor concentration range of 0.1 M to 0.4 M. They found that the interaction between reaction temperature and precursor concentration was less significant on the α-Fe<sub>2</sub>O<sub>3</sub> product yield than the independent effect of the process parameters. Kriedeman & Fester (2015) stated there was an increase in the product yield as reaction temperature and residence time increased. Lester et al. (2012) found that an increase in the reaction temperature from 200°C to 430°C resulted in a higher Co<sub>3</sub>O<sub>4</sub> yield for cobalt (II) acetate tetrahydrate and the response of the yield concurs with the findings of this study. Table 4.5 shows that the maximum yield for Co(NO<sub>3</sub>)<sub>2</sub>·6H<sub>2</sub>O- and CoCl<sub>12</sub>·6H<sub>6</sub>O -derived Co<sub>3</sub>O<sub>4</sub> was

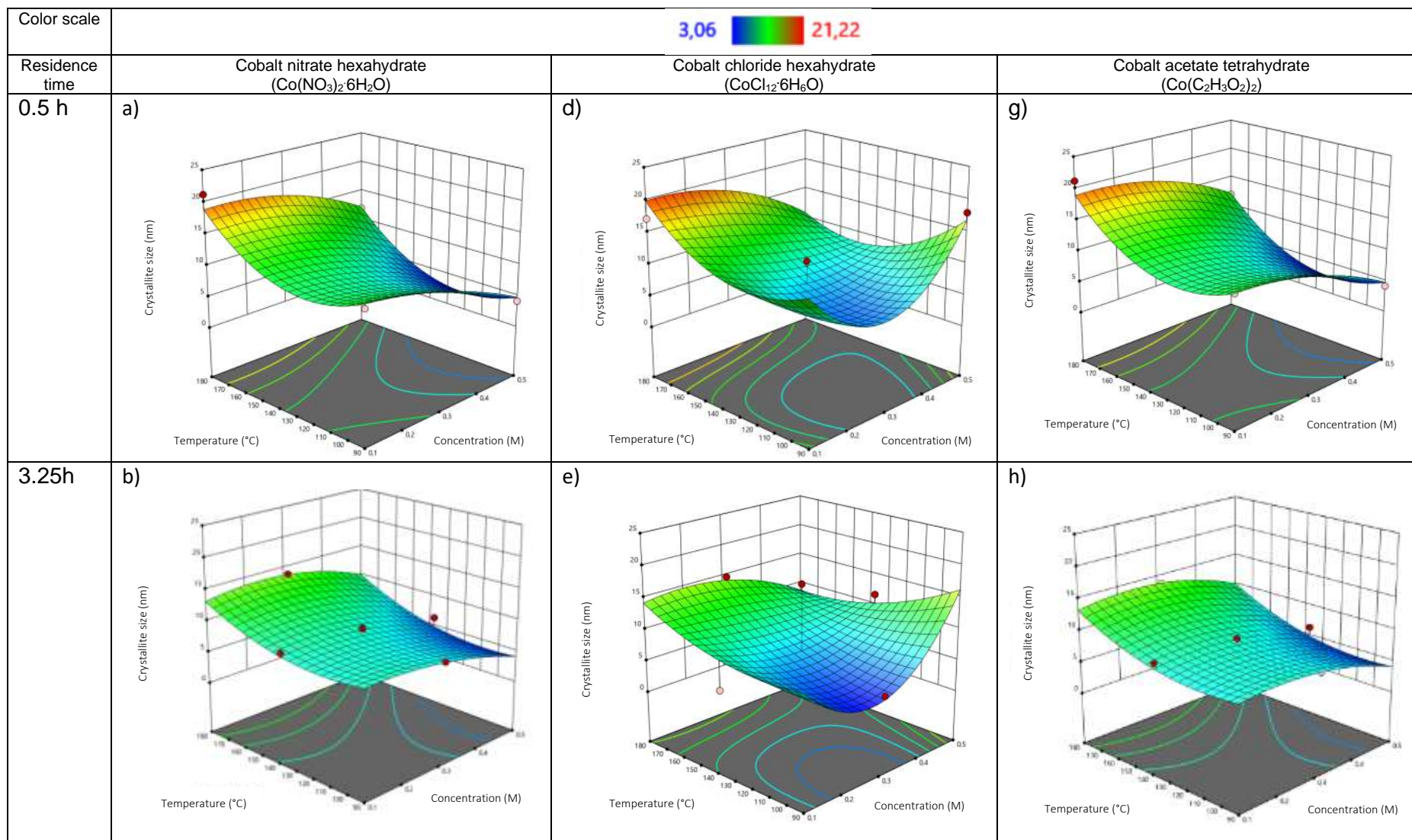
obtained at the lowest residence time while Lester et al. (2012) found the lowest product yield at the lowest residence time. The residence time for the maximum yield for  $\text{Co}(\text{C}_2\text{H}_3\text{O}_2)_2$ -derived  $\text{Co}_3\text{O}_4$  concurs with the finding of Lester et al. (2012), who also used the same precursor salt.

Comparing the results of the influence of precursor concentration that was found in this study to an investigation done by Kriedemann & Fester (2015) on the production of  $\alpha\text{-Fe}_2\text{O}_3$  nanopowders, the interaction between high precursor concentration and increased flow rates resulted in the maximum yield. At higher concentrations, the available growth species at the interface of the nuclei is similar to that of the bulk solution and thus the diffusion distance for the growth species is shorter. This behaviour results in a higher mass transfer and thereby a higher growth rate (Dehsari et al., 2017). The results found in this study showed that  $\text{Co}(\text{NO}_3)_2 \cdot 6\text{H}_2\text{O}$ - and  $\text{CoCl}_{12} \cdot 6\text{H}_2\text{O}$ -derived  $\text{Co}_3\text{O}_4$  nanoparticles conformed with their results while  $\text{Co}(\text{C}_2\text{H}_3\text{O}_2)_2$ -derived  $\text{Co}_3\text{O}_4$  contradicted the results found by Kriedemann & Fester (2015). The  $\text{Co}(\text{C}_2\text{H}_3\text{O}_2)_2$  precursor concentration negatively affects the product yield as the reaction temperature increases. This work therefore highlights the important role of the precursor in the product yield and that more fundamental studies should be done to understand its role.

#### **4.3.2 Effect of process parameters on the crystallite size of produced nanocatalyst**

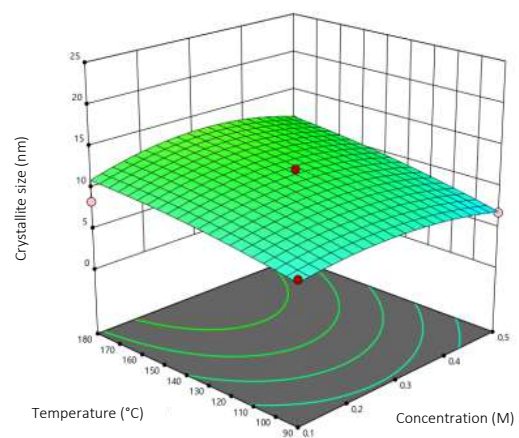
Table 4.6 shows the effect of residence time between 30 minutes and 6 hours on the crystallite size of  $\text{Co}(\text{NO}_3)_2 \cdot 6\text{H}_2\text{O}$ -,  $\text{CoCl}_{12} \cdot 6\text{H}_2\text{O}$ - and  $\text{Co}(\text{C}_2\text{H}_3\text{O}_2)_2$ -derived  $\text{Co}_3\text{O}_4$ . The temperature ranged at  $90^\circ\text{C} - 180^\circ\text{C}$  and the precursor concentration ranging between 0.1 M and 0.5 M.

**Table 4.6: The crystallite size as a response of the interaction between precursor concentration and reaction temperature at a residence time a) 0.5 hours, b) 3.25 hours and c) 6 hours.**

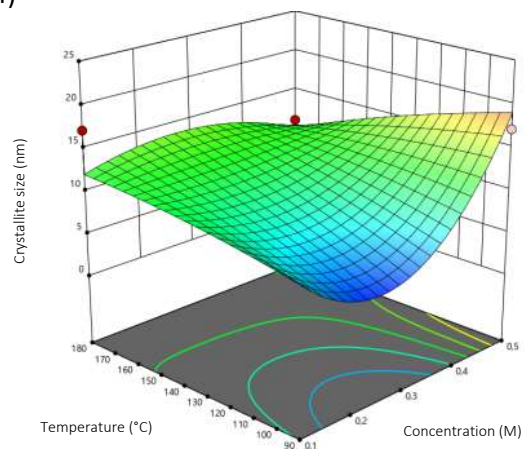


6h

c)



f)



i)

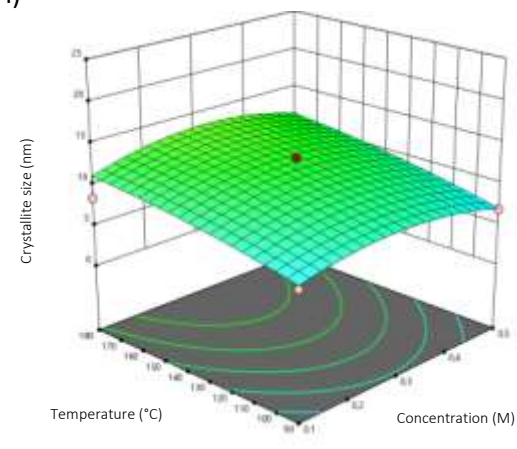
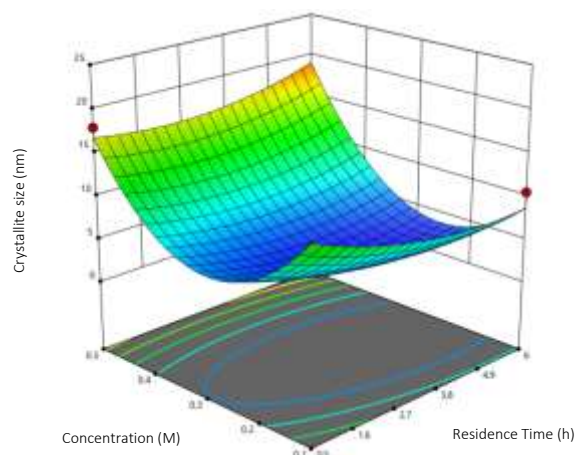


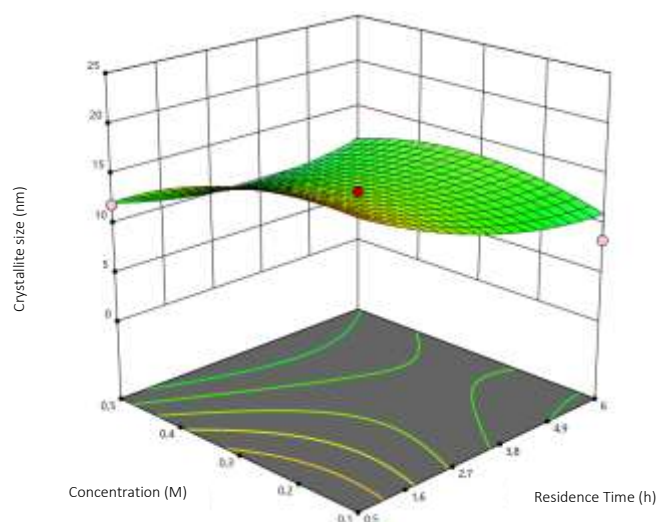
Table 4.6 a-c shows the crystallite size of  $\text{Co}(\text{NO}_3)_2 \cdot 6\text{H}_2\text{O}$ -derived  $\text{Co}_3\text{O}_4$  nanoparticles. The crystallite size of  $\text{Co}(\text{NO}_3)_2 \cdot 6\text{H}_2\text{O}$ -derived  $\text{Co}_3\text{O}_4$  nanoparticles decreased as the residence time increased from 30 minutes to 6 hours. At the highest residence time, the interaction of the precursor concentration was less significant in comparison with the significance of the interaction at the lowest residence time. It can be seen that at the lowest reaction temperature and highest precursor concentration there was an increase in the crystallite size as the residence time increased. The crystallite size increased as the reaction temperature increased and decrease as the precursor concentration increased. It can be seen that at the lowest residence time and highest reaction temperature there was a decrease as the precursor concentration increased from 0.1 M to 0.5 M. The largest crystallite size was obtained at the highest reaction temperature and residence time while the lowest precursor concentration was significant. The crystallite size ranged between 4.15 nm and 21.22 nm.

Table 4.6 d-f shows the crystallite size of  $\text{CoC}_{12}\text{H}_6\text{O}$ -derived  $\text{Co}_3\text{O}_4$  nanoparticles. For  $\text{CoC}_{12}\text{H}_6\text{O}$  -derived  $\text{Co}_3\text{O}_4$  nanoparticles, it was observed that as the residence time increases the crystallite size increases at the lowest reaction temperature and highest precursor concentration while a decrease is observed at the highest reaction temperature and lowest precursor concentration. The interaction between the residence time and precursor concentration, at the lowest reaction temperature, is more pronounced at the highest residence time. Figure 4.3 shows at the lowest reaction temperature and precursor concentration the effect of the residence time is redundant but at the highest precursor concentration the effect becomes more significant. Across the residence time range, there is a decrease in the crystallite size between a precursor concentration of 0.1 M and 0.3 M and a significant increase between a precursor concentration of 0.3 M and 0.5 M. For both  $\text{Co}(\text{NO}_3)_2 \cdot 6\text{H}_2\text{O}$ - and  $\text{CoC}_{12}\text{H}_6\text{O}$ -derived  $\text{Co}_3\text{O}_4$ , the highest reaction temperature and residence time is at the lowest precursor concentration and results in the largest crystallite sizes. At a high reaction temperature and residence time, there is a decrease in crystallite size as the precursor concentration increases from 0.3 M to 0.5 M. At the highest reaction temperature, the crystallite size behaves in a similar manner to the interaction of the operation parameters as the other two precursor salts. The crystallite size ranges between 3.06 nm and 17.97 nm.



**Figure 4.3: The crystallite size as a response of the interaction between residence time and precursor concentration at a reaction temperature of 90 °C**

Table 4.6 g-i shows the crystallite size of  $\text{Co}(\text{C}_2\text{H}_3\text{O}_2)_2$ -derived  $\text{Co}_3\text{O}_4$  nanoparticles. For the  $\text{Co}(\text{C}_2\text{H}_3\text{O}_2)_2$ - precursor, it can be seen that the crystallite size responds in the same manner to changes in the residence time as  $\text{Co}(\text{NO}_3)_2 \cdot 6\text{H}_2\text{O}$ -derived  $\text{Co}_3\text{O}_4$  nanoparticles. There is a decrease in the crystallite size as the residence time and precursor concentration increase and an increase in the crystallite size as the reaction temperature increases. At the lowest residence time, the interaction of the precursor concentration is more significant in comparison with the significance of the interaction at the highest residence time. It can be seen that at the lowest reaction temperature and highest precursor concentration there is an increase in the crystallite size as the residence time increases. At the lowest residence time and the highest reaction temperature there is an increase in the crystallite size as the precursor concentration increases from 0.1 M to 0.3 M and a decrease as the precursor concentration increases from 0.3 M to 0.5 M – this can clearly be seen in Figure 4.4. The largest crystallite sizes are found at the highest reaction temperature and the lowest residence time and precursor concentration. The crystallite size ranges between 4.16 nm and 21.22 nm.



**Figure 4.4: The crystallite size as a response of the interaction between residence time and precursor concentration at a reaction temperature 180°C**

Table 4.7 and Table 4.8 show the minimum and maximum crystallite sizes for  $\text{Co}(\text{NO}_3)_2 \cdot 6\text{H}_2\text{O}$ -,  $\text{CoCl}_{12} \cdot 6\text{H}_2\text{O}$ - and  $\text{Co}(\text{C}_2\text{H}_3\text{O}_2)_2$ -derived  $\text{Co}_3\text{O}_4$  nanoparticles. It can be seen that crystallite sizes for  $\text{Co}(\text{NO}_3)_2 \cdot 6\text{H}_2\text{O}$  and  $\text{Co}(\text{C}_2\text{H}_3\text{O}_2)_2$  precursors respond in the same manner. The minimum crystallite sizes are produced at the lowest reaction temperature and residence time and highest precursor concentration.  $\text{CoCl}_{12} \cdot 6\text{H}_2\text{O}$  precursor produces the smallest  $\text{Co}_3\text{O}_4$  nanoparticles in comparison with the other precursor salts. It can be seen that  $\text{CoCl}_{12} \cdot 6\text{H}_2\text{O}$ -derived  $\text{Co}_3\text{O}_4$  nanoparticles produce the smallest crystallite size at a higher reaction temperature and residence time and lower precursor concentration. The maximum crystallite sizes are all found at residence time of 30 minutes.  $\text{CoCl}_{12} \cdot 6\text{H}_2\text{O}$  precursor produces the smallest crystallite size particles, compared to the other precursor salts, at the lowest reaction temperature and highest precursor concentration.  $\text{Co}(\text{NO}_3)_2 \cdot 6\text{H}_2\text{O}$ - and  $\text{Co}(\text{C}_2\text{H}_3\text{O}_2)_2$ -derived  $\text{Co}_3\text{O}_4$  nanoparticle crystallite size are produced at the highest reaction temperature and the lowest precursor concentration and residence time. The crystallite size for  $\text{Co}(\text{NO}_3)_2 \cdot 6\text{H}_2\text{O}$ - and  $\text{Co}(\text{C}_2\text{H}_3\text{O}_2)_2$  precursor salts are 15.32% larger than that of  $\text{CoCl}_{12} \cdot 6\text{H}_2\text{O}$  crystallite sizes.

**Table 4.7: Operating parameters for minimum  $\text{Co}_3\text{O}_4$  crystallite size**

Precursor Salt	Reaction Temperature (°C)	Precursor Concentration (M)	Residence time (h)	Minimum Crystallite size (nm)
Cobalt nitrate hexahydrate ( $\text{Co}(\text{NO}_3)_2 \cdot 6\text{H}_2\text{O}$ )	90	0.5	0.5	4.15
Cobalt chloride hexahydrate ( $\text{CoCl}_{12} \cdot 6\text{H}_2\text{O}$ )	135	0.3	3.25	3.06
Cobaltacetate tetrahydrate ( $\text{Co}(\text{C}_2\text{H}_3\text{O}_2)_2$ )	90	0.5	0.5	4.16

**Table 4.8: Operating parameters for maximum Co<sub>3</sub>O<sub>4</sub> crystallite size**

Precursor Salt	Reaction Temperature (°C)	Precursor Concentration (M)	Residence time (h)	Maximum Crystallite size (nm)
Cobalt nitrate hexahydrate (Co(NO <sub>3</sub> ) <sub>2</sub> ·6H <sub>2</sub> O)	180	0.1	0.5	21.22
Cobalt chloride hexahydrate (CoCl <sub>2</sub> ·6H <sub>2</sub> O)	90	0.5	0.5	17.97
Cobaltacetate tetrahydrate (Co(C <sub>2</sub> H <sub>3</sub> O <sub>2</sub> ) <sub>2</sub> )	180	0.1	0.5	21.22

Generally, it is expected that as that the crystallite size will increase as a response to the increase in reaction temperature as the over-potential decreases with increasing temperature and the energy of nucleus formation increases consequently (Yadav et al., 2007). This concurs with the results found for the crystallite sizes for Co(NO<sub>3</sub>)<sub>2</sub>·6H<sub>2</sub>O- and Co(C<sub>2</sub>H<sub>3</sub>O<sub>2</sub>)<sub>2</sub>-derived Co<sub>3</sub>O<sub>4</sub>. Yadav et al. (2007) stated that it is generally accepted that the growth of nanoparticles proceeds due to diffusion that is controlled by the Ostwald ripening process. The reaction temperature influences Ostwald ripening through its effect on the equilibrium solubility, interfacial energy and growth rate coefficients. The effect of reaction temperature has been widely researched and it has been found that the crystallite size of the nanoparticles is favoured by an increase in the reaction temperature. The XRD patterns of the synthesised silver nanoparticles, by Reduan et al. (2016), showed a decrease in the wavelength at the maximum peak as the precursor concentration was increased. Kriedemann & Fester (2015) found in their study for the production of iron oxide nanoparticles that the relative crystallinity of the nanopowders is strongly affected by the precursor salt concentration. It was found that an increase in precursor concentration resulted in a decrease in crystallite size as for Co(NO<sub>3</sub>)<sub>2</sub>·6H<sub>2</sub>O - and Co(C<sub>2</sub>H<sub>3</sub>O<sub>2</sub>)<sub>2</sub>-derived Co<sub>3</sub>O<sub>4</sub> nanoparticles. The behaviour of Co(NO<sub>3</sub>)<sub>2</sub>·6H<sub>2</sub>O - and Co(C<sub>2</sub>H<sub>3</sub>O<sub>2</sub>)<sub>2</sub>-derived Co<sub>3</sub>O<sub>4</sub> crystallite sizes towards the interaction between the reaction temperature and precursor concentration agrees with the finding of Kriedemann & Fester (2015), who stated that this interaction has a very low significance. From Table 4.5, it can be seen that the crystallite sizes of the CoC<sub>12</sub>6H<sub>6</sub>O-derived Co<sub>3</sub>O<sub>4</sub> is strongly affected by the interaction between reaction temperature and precursor concentration. Lester et al. (2012) also found that in the production of Co<sub>3</sub>O<sub>4</sub> nanoparticles the increase in reaction temperature from 200 °C to 450 °C and increase in the concentration of cobalt acetate tetrahydrate precursor from 0.1 M to 0.5 M resulted in a reduction of crystallite size. As for Co(C<sub>2</sub>H<sub>3</sub>O<sub>2</sub>)<sub>2</sub>- and Co(NO<sub>3</sub>)<sub>2</sub>·6H<sub>2</sub>O-derived Co<sub>3</sub>O<sub>4</sub>, Lester et al. (2012) found that the largest crystallite sizes were found at the lowest precursor concentration. The response of the crystallite size may be explained by increased rates of nucleation at increased reaction

temperatures or a change in particle kinetics may occur where growth kinetics are dominated by nucleation kinetics and thus nanoparticles with larger crystallite sizes are obtained when insufficient concentrations of the ions are available to form a new discrete particle. An increase in the residence time from 30 minutes to 6 hours resulted in an increase of crystallite size at the lowest reaction temperature and highest precursor concentration of  $\text{Co}(\text{NO}_3)_2 \cdot 6\text{H}_2\text{O}$ -,  $\text{CoCl}_{12} \cdot 6\text{H}_2\text{O}$  - and  $\text{Co}(\text{C}_2\text{H}_3\text{O}_2)_2$ -derived  $\text{Co}_3\text{O}_4$  nanopowders. This behaviour is consistent with the results of Lester et al. (2012) and Kriedemann & Fester (2015) that show there is an increase in crystallite size as the residence time increases. The results found in the studies mentioned above were contradicted by the following: a decrease in the crystallite size was observed as the residence time increased from 30 minutes to 6 hours at the highest reaction temperature and lowest precursor concentration of  $\text{Co}(\text{NO}_3)_2 \cdot 6\text{H}_2\text{O}$ -,  $\text{CoCl}_{12} \cdot 6\text{H}_2\text{O}$  - and  $\text{Co}(\text{C}_2\text{H}_3\text{O}_2)_2$ -derived  $\text{Co}_3\text{O}_4$  nanopowders.

### 4.3.3 Final summary based on the findings

From this chapter the effect of reaction temperature, precursor concentration, precursor salt and reaction temperature, as well as their interactions, on the product yield and crystallite size are summarised below:

$\text{Co}(\text{NO}_3)_2 \cdot 6\text{H}_2\text{O}$ -,  $\text{CoCl}_{12} \cdot 6\text{H}_2\text{O}$  and  $\text{Co}(\text{C}_2\text{H}_3\text{O}_2)_2$ -derived  $\text{Co}_3\text{O}_4$  nanoparticles showed that the product yield increased as the reaction temperature increased. A maximum was obtained for the product yield at intermediate precursor concentration while a minimum was found at the intermediate residence time for  $\text{Co}(\text{NO}_3)_2 \cdot 6\text{H}_2\text{O}$ - and  $\text{CoCl}_{12} \cdot 6\text{H}_2\text{O}$ -derived  $\text{Co}_3\text{O}_4$ . The product yield for  $\text{Co}(\text{C}_2\text{H}_3\text{O}_2)_2$ -derived  $\text{Co}_3\text{O}_4$  nanoparticles decreased with increasing precursor concentration and reaction temperature.

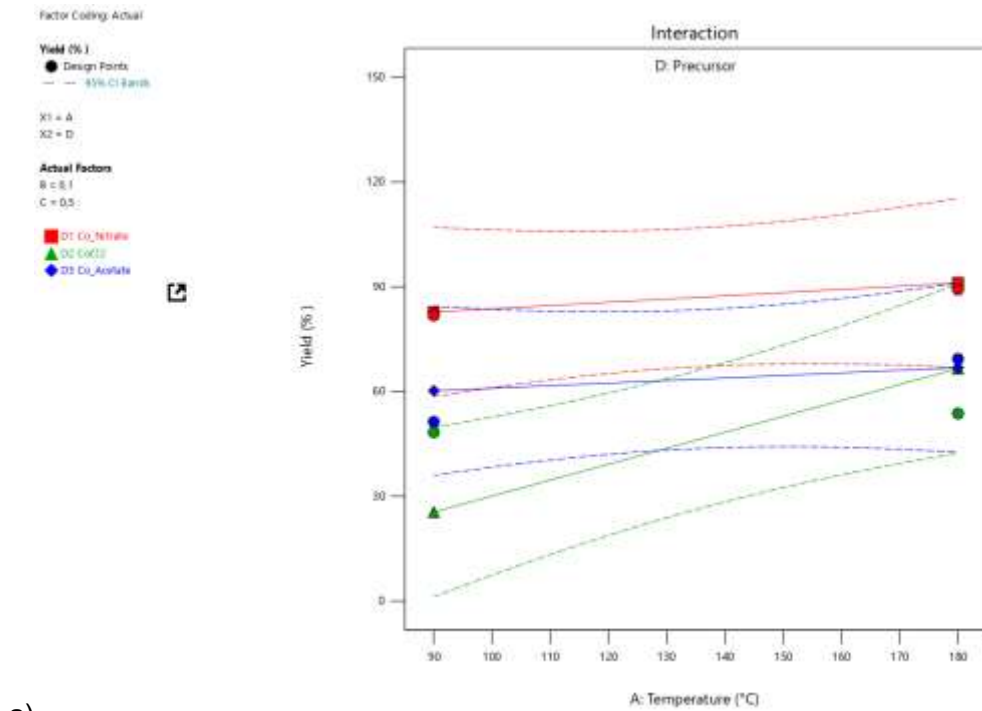
For  $\text{Co}(\text{NO}_3)_2 \cdot 6\text{H}_2\text{O}$ -derived  $\text{Co}_3\text{O}_4$  nanoparticles, it was found that the highest yield was found at intermediate temperature and precursor concentration and minimum residence time. The lowest product yield for  $\text{Co}(\text{NO}_3)_2 \cdot 6\text{H}_2\text{O}$ -derived  $\text{Co}_3\text{O}_4$  was found at the lowest reaction temperature and precursor concentration and intermediate residence time. The yields obtained ranged from 56.00% to 100.00%. Using  $\text{Co}(\text{NO}_3)_2 \cdot 6\text{H}_2\text{O}$  precursor salt resulted in the highest product yield in comparison with the other precursor salts.

For  $\text{CoCl}_{12} \cdot 6\text{H}_2\text{O}$  -derived  $\text{Co}_3\text{O}_4$  the yields obtained ranged from 1.00% and 82.00%. The highest product yield for  $\text{CoCl}_{12} \cdot 6\text{H}_2\text{O}$  -derived  $\text{Co}_3\text{O}_4$  was found at the highest reaction temperature, lowest residence time and the intermediate precursor concentration. The lowest yield was found at the lowest reaction temperature and precursor concentration at intermediate residence time.

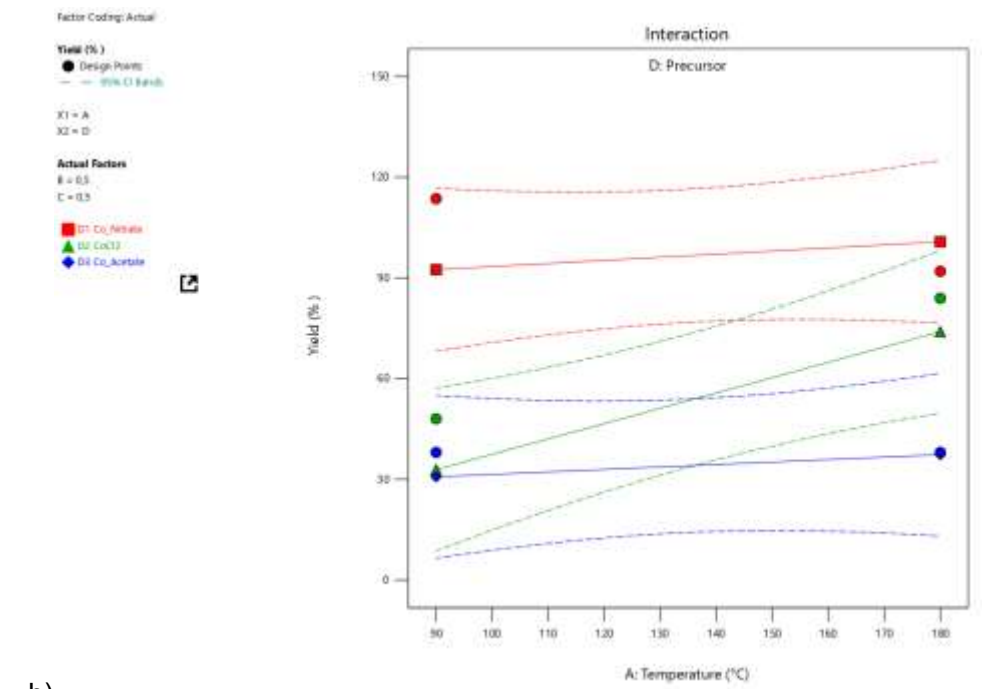
For the  $\text{Co}(\text{C}_2\text{H}_3\text{O}_2)_2$ -derived  $\text{Co}_3\text{O}_4$  the effect of the reaction temperature and residence time was found to be the same as for  $\text{Co}(\text{NO}_3)_2 \cdot 6\text{H}_2\text{O}$ -,  $\text{CoCl}_{12} \cdot 6\text{H}_2\text{O}$ -derived  $\text{Co}_3\text{O}_4$  while the effect of the precursor concentration differed. The highest yield was obtained at a low precursor concentration and the highest reaction temperature and residence time. The lowest product yield for  $\text{Co}(\text{C}_2\text{H}_3\text{O}_2)_2$ -derived  $\text{Co}_3\text{O}_4$  was found at the lowest reaction temperature, intermediate residence time and the highest precursor concentration. The yields obtained ranged from 12.00% and 66.00%. In comparison with the other two precursors, the product yield for  $\text{Co}(\text{C}_2\text{H}_3\text{O}_2)_2$ -derived  $\text{Co}_3\text{O}_4$  is the lowest.

For  $\text{Co}(\text{NO}_3)_2 \cdot 6\text{H}_2\text{O}$ - and  $\text{CoCl}_{12} \cdot 6\text{H}_2\text{O}$  - derived  $\text{Co}_3\text{O}_4$  nanoparticle it was found that the maximum product yield was found at the lowest residence time while Lester et al. (2012) found the lowest product yield at the lowest residence time. The residence time for the maximum yield for  $\text{Co}(\text{C}_2\text{H}_3\text{O}_2)_2$ -derived  $\text{Co}_3\text{O}_4$  concurs with the finding of Lester et al. (2012). Lester et al. (2012) and Kriedemann & Fester (2015) found that an increase in the reaction temperature resulted in a higher product yield, this response of the yield concurs with the findings of this study. The results found in this study showed that the product yield for  $\text{Co}(\text{NO}_3)_2 \cdot 6\text{H}_2\text{O}$ - and  $\text{CoCl}_{12} \cdot 6\text{H}_2\text{O}$  -derived  $\text{Co}_3\text{O}_4$  nanoparticles increased as the precursor concentration increased and conformed with the results found by Kriedemann & Fester (2015) while the product yield for  $\text{Co}(\text{C}_2\text{H}_3\text{O}_2)_2$  -derived  $\text{Co}_3\text{O}_4$  contradicted the results by decreasing as the precursor concentration increased.

A summary of the effect of the precursor salt is provided in Figure 4.5. Figure 4.5 a) shows the effect of the reaction temperature on the product yield at a low precursor concentration for each of the precursor salts. The product yield for  $\text{Co}(\text{NO}_3)_2 \cdot 6\text{H}_2\text{O}$  and  $\text{Co}(\text{C}_2\text{H}_3\text{O}_2)_2$  precursor salts are not sensitive for the changes in the reaction temperature. The steep gradient for the product yield of  $\text{Co}(\text{NO}_3)_2 \cdot 6\text{H}_2\text{O}$ -derived  $\text{Co}_3\text{O}_4$  nanoparticles as the reaction temperature increases shows that the product yield is highly sensitive to changes in the reaction temperature. At low precursor concentrations it is found that the product yield is higher using a  $\text{Co}(\text{C}_2\text{H}_3\text{O}_2)_2$  precursor salt than that of  $\text{CoCl}_{12} \cdot 6\text{H}_2\text{O}$  precursor salt. As the precursor concentration increases it the product yield for  $\text{Co}(\text{C}_2\text{H}_3\text{O}_2)_2$  precursor salt decreases and is surpassed by the yield of  $\text{CoCl}_{12} \cdot 6\text{H}_2\text{O}$  precursor salt. This can be seen in Figure 4.5 b).



a)



b)

**Figure 4.5: Effect of the reaction temperature and precursor concentration interaction on product yield (a) low precursor concentration and (b) high precursor concentration**

The crystallite size of  $\text{Co}(\text{NO}_3)_2 \cdot 6\text{H}_2\text{O}$ - and  $\text{Co}(\text{C}_2\text{H}_3\text{O}_2)_2$ -precursor derived  $\text{Co}_3\text{O}_4$  presented the same trends. The crystallite size decreased as the residence time was increased from 30 minutes to 6 hours. These findings concur with results found by Kriedemann & Fester (2015), Yadav et al. (2007) and Lester et al. (2012). At the lowest reaction temperature and highest precursor concentration there is an increase in the crystallite size as the residence

time increases. For  $\text{Co}(\text{NO}_3)_2 \cdot 6\text{H}_2\text{O}$ - and  $\text{Co}(\text{C}_2\text{H}_3\text{O}_2)_2$ -derived  $\text{Co}_3\text{O}_4$  the largest crystallite sizes are found at the highest reaction temperature and the lowest residence time and precursor concentration. The crystallite sizes for both precursor salts range between 4.15 nm and 21.22 nm.

For  $\text{CoCl}_2 \cdot 6\text{H}_2\text{O}$  -derived  $\text{Co}_3\text{O}_4$  nanoparticles it was observed that as the residence time increased the crystallite size increased at the lowest reaction temperature and highest precursor concentration while a decrease was observed at the highest reaction temperature and lowest precursor concentration. The interaction between the residence time and precursor concentration, at the lowest reaction temperature, was more significant at the highest residence time. The crystallite sizes ranged between 3.06 nm and 17.97 nm.

In the case of the product yield the chloride and acetate behaved similarly while in the case of the crystallite size the nitrate and acetate responded in a similar manner.

## **Chapter 5 Evaluation of the synthesised $\text{Co}_3\text{O}_4$ nanoparticles during colour degradation**

### **5.1 Introduction**

The objective of this chapter was to evaluate the synthesised  $\text{Co}_3\text{O}_4$  nanoparticles that were produced using  $\text{Co}(\text{C}_2\text{H}_3\text{O}_2)_2^-$ ,  $\text{CoCl}_{12}\cdot 6\text{H}_2\text{O}$ - and  $\text{Co}(\text{NO}_3)_2\cdot 6\text{H}_2\text{O}$  precursor salts under various process conditions (reaction temperature, precursor concentration and residence time) as a catalyst for the degradation of methyl orange dye. The percentage degradation was included as a response in the factorial trial matrix. The degradation curves for each precursor salt will first be presented, followed by the analysis of variance to obtain a prediction for percentage degradation as a function of process conditions.

The degradation process makes use of an AOP, where  $\text{Co}_3\text{O}_4$  was used as the catalyst and peroxymonosulphate (Oxone<sup>®</sup>) as the oxidiser. The  $\text{Co}_3\text{O}_4$  nanocatalyst were used in conjunction with Oxone<sup>®</sup> in order to generate sulphate radicals in the solution. The concentration of the MO and amount of  $\text{Co}_3\text{O}_4$  nanocatalyst was kept constant.

### **5.2 Degradation studies using $\text{Co}_3\text{O}_4$ nanocatalyst to treat MO dye water**

The degradation of the MO dye using the synthesised  $\text{Co}(\text{C}_2\text{H}_3\text{O}_2)_2^-$ -derived  $\text{Co}_3\text{O}_4$  particles was observed over period of 30 minutes. The percentage of MO dye that was removed as the contact time increased can be seen in Figure 5.1

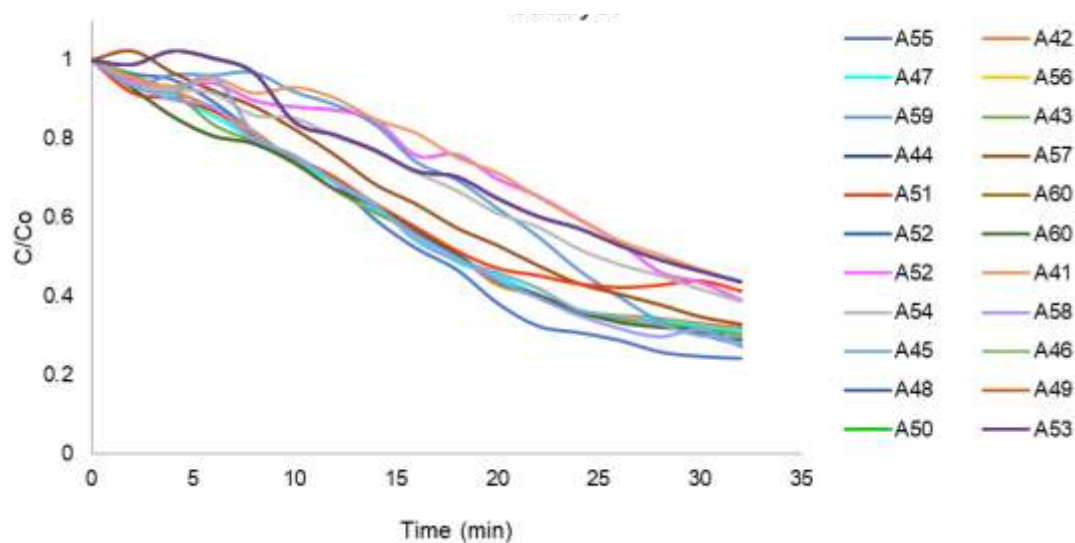


**Figure 5.1: Degradation of the MO dye using  $\text{Co}_3\text{O}_4$  derived by  $\text{Co}(\text{C}_2\text{H}_3\text{O}_2)_2$ - precursor**

It was found that the catalyst that was produced at a temperature of  $180^\circ\text{C}$ , concentration of 0.1 M and a reaction time of 3.2 hours performed the worst by only removing 56.31% of dye in the solution after 30 minutes of contact time. The catalyst that was produced at a temperature of  $90^\circ\text{C}$ , concentration of 0.1 M and a reaction time of 6 hours performed the best by removing 67.93% of the dye in the solution after 30 minutes. From the degradation curve it can be seen that for a majority of the samples the curves start to flatten at 25 minutes.

Secondly, the degradation of the MO dye using the  $\text{Co}_3\text{O}_4$  nanocatalyst that was produced using  $\text{CoCl}_{12}\cdot 6\text{H}_2\text{O}$  precursor is shown in Figure 5.2.

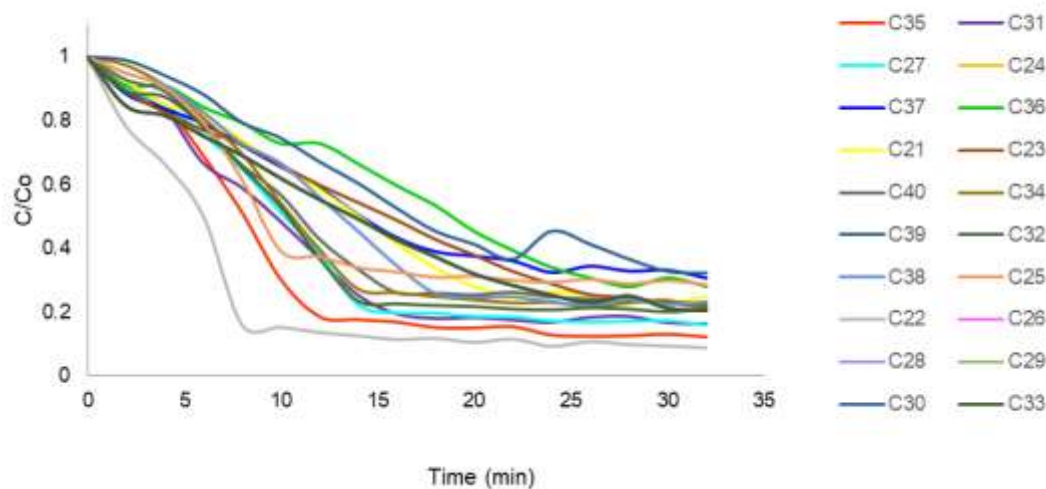


**Figure 5.2: Degradation of the MO dye using  $\text{Co}_3\text{O}_4$  derived by  $\text{CoCl}_{12}\cdot 6\text{H}_2\text{O}$ - precursor**

It was found that the catalyst that was produced at a temperature of 90°C, concentration of 0.5 M and a reaction time of 3.2 hours performed the worst by only removing 68.62% of dye in the solution after 30 minutes. The catalyst that was produced at a temperature of 90°C, concentration of 0.1 M and a reaction time of 6 hours performed the best, removing 90.17% of the dye in the solution after 30 minutes. From the degradation curve it can be seen that for a majority of the samples the degradation peak was achieved in under 15 minutes.

Lastly the degradation of the MO dye using the  $\text{Co}_3\text{O}_4$  nanocatalyst that was produced using  $\text{Co}(\text{NO}_3)_2 \cdot 6\text{H}_2\text{O}$  precursor is shown in Figure 5.3.

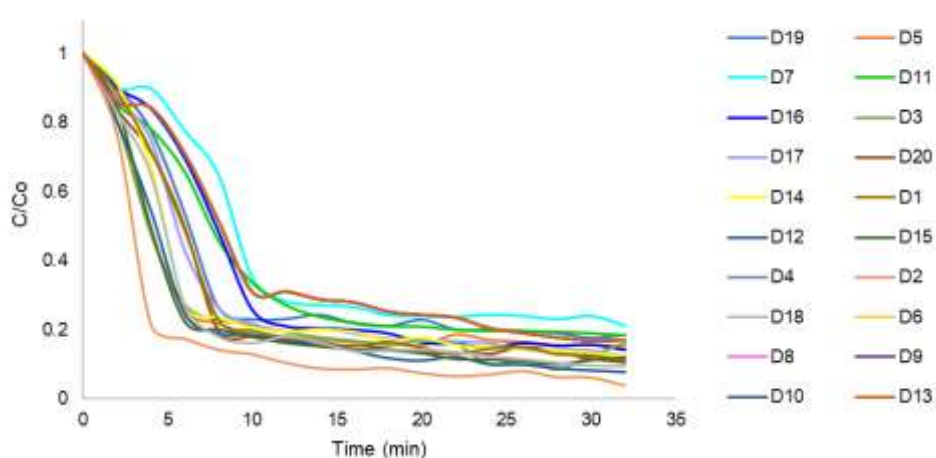


**Figure 5.3: Degradation of the MO dye using  $\text{Co}_3\text{O}_4$  derived by  $\text{Co}(\text{NO}_3)_2 \cdot 6\text{H}_2\text{O}$ - precursor**

It was found that the catalyst that was produced at a temperature of 180°C, concentration of 0.1 M and a reaction time of 3.2 hours performed the worst, removing 84.85% of dye in the solution after 30 minutes. The catalyst that was produced at a temperature of 90°C, concentration of 0.1 M and a reaction time of 0.5 hours performed the best, removing 96.18% of the dye in the solution after 30 minutes. From the degradation curve it can be seen that for a majority of the samples the degradation peak was achieved in under 10 minutes. Comparing the efficiency of the  $\text{Co}(\text{NO}_3)_2 \cdot 6\text{H}_2\text{O}$ -derived  $\text{Co}_3\text{O}_4$  nanocatalyst to that of the  $\text{CoCl}_{12} \cdot 6\text{H}_2\text{O}$ - and  $\text{Co}(\text{C}_2\text{H}_3\text{O}_2)_2$ -derived  $\text{Co}_3\text{O}_4$  nanocatalyst it can be seen that the  $\text{Co}(\text{NO}_3)_2 \cdot 6\text{H}_2\text{O}$ -derived  $\text{Co}_3\text{O}_4$  nanocatalyst has a shorter required degradation period and is the most efficient.

The final degradation result obtained for each catalyst at the end of 30 minutes was included as a response in the Design-Expert factorial trial to obtain a correlation to determine the optimal degradation as a function of process parameters. The analysis of variance is presented in the next section.

### 5.3 Effect of process parameters for the production of the produced Co<sub>3</sub>O<sub>4</sub> nanocatalyst on the degradation of methyl orange

The ANOVA results for the degradation of MO solution that were obtained from the CCD design analysis are presented Table 5.1. The probability for significance of the model was found to be less than 0.0001, thus making the model significant, at a 5% significance level (Hassanzadeh et al., 2017; Nautiyal & Shukla, 2018; Noordin et al., 2004; Nautiyal & Shukla, 2018). The p-value is the probability of seeing the observed of F-value or larger if the null hypothesis is true. Small p-values reject the hypothesis of zero effect. The F-value for significance of the model is 24.22 with  $p < 0.0001$ , which shows a good fit. The adjusted coefficient of determination (Adj. R<sup>2</sup>), which is the correlation between the observed and predicted values, in this case 0.7798, indicates a good model fit.

A: Temperature, B: Concentration, C: Residence time, D: Precursor salt, AB: Interaction between reaction temperature and precursor concentration, BD: Interaction between precursor concentration and precursor salt, C<sup>2</sup> are the quadratic effects of the residence time respectively.

Table 5.1: Analysis of variance table for degradation

Source	Sum of Squares	Degrees of freedom	Mean Square	F-value	p-value
<b>Model</b>	8122.64	9	902.52	24.22	< 0.0001
A-Temperature	38.12	1	38.12	1.02	0.3167
B-Concentration	138.5	1	138.5	3.72	0.0596
C-Residence Time	0.3635	1	0.3635	0.0098	0.9217
D-Precursor	7331.65	2	3665.8	98.37	< 0.0001
AB	243.1	1	243.1	6.52	0.0137
BD	245.25	2	122.63	3.29	0.0454
C <sup>2</sup>	125.65	1	125.65	3.37	0.0723
<b>Residual</b>	1863.25	50	37.26		
Lack of Fit	1863.25	35	53.24		
Pure Error	0	15	0		
<b>Cor Total</b>	9985.89	59			

The prediction models (hierarchically corrected) for degradation of MO solution using  $\text{Co}_3\text{O}_4$  catalyst produced with cobalt nitrate hexahydrate ( $\text{Co}(\text{NO}_3)_2 \cdot 6\text{H}_2\text{O}$ ), cobalt chloride hexahydrate ( $\text{CoCl}_2 \cdot 6\text{H}_2\text{O}$ ) and cobalt acetate tetrahydrate ( $\text{Co}(\text{C}_2\text{H}_3\text{O}_2)_2$ ) precursor can be seen in Equation 5-1 - Equation 5-3 respectively where A is the temperature, B the concentration and C the residence time. The models below represent the degradation as a function of the operating parameters for the production of the  $\text{Co}_3\text{O}_4$  nano-catalyst. From the degradation models (Equation 5-1- Equation 5-3) it can be seen that except for the precursor concentration term there is no significant difference in the models.

Degradation(%) Cobalt nitrate hexahydrate Equation 5-1

$$= 111,25 - 0,13A - 52,55B - 2,45C + 0,35AB + 0,38C^2$$

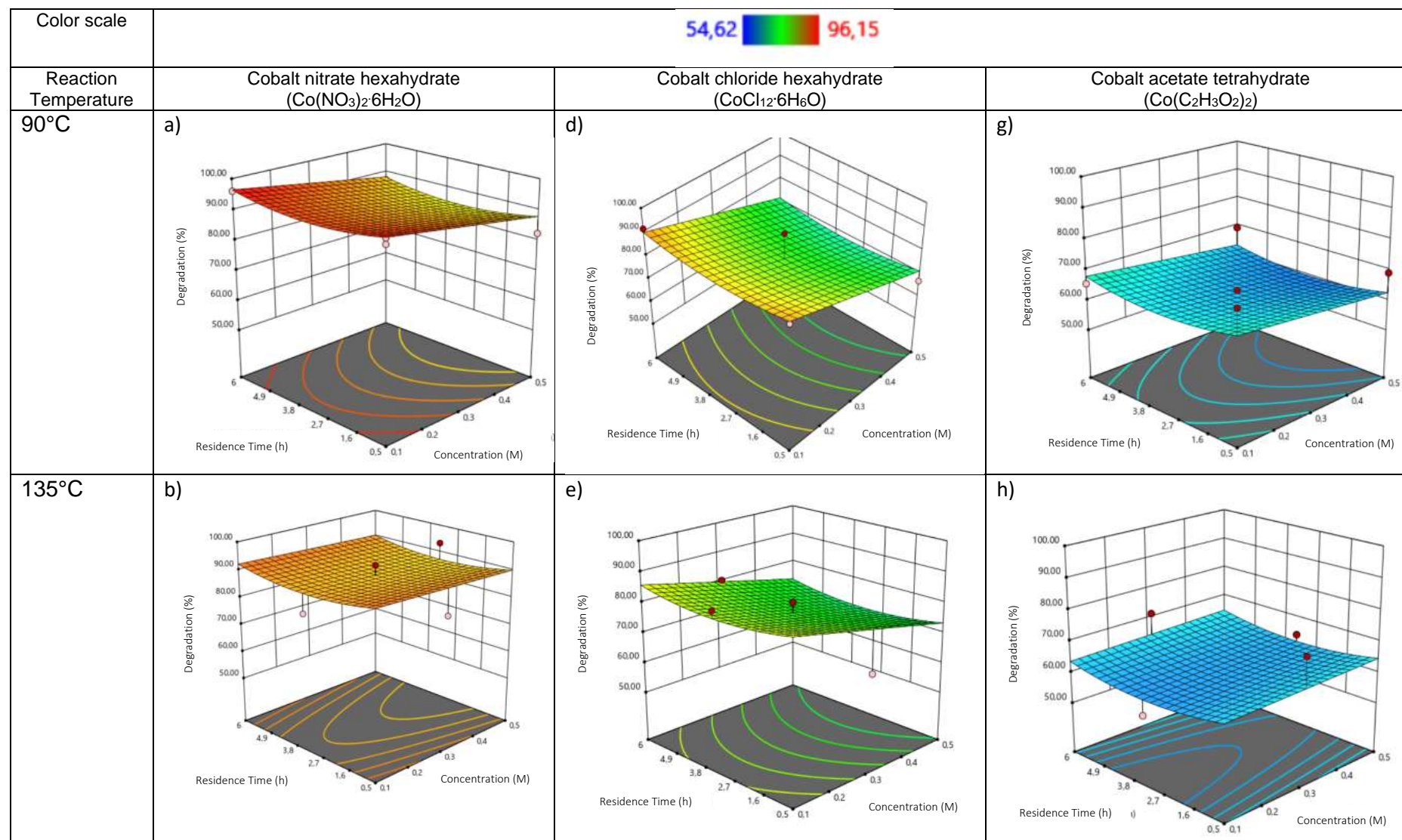
Degradation(%) Cobalt chloride hexahydrate Equation 5-2

$$= 107,52 - 0,13A - 78,19B - 2,45C + 0,35AB + 0,38C^2$$

Degradation (%) Cobalt acetate tetrahydrate Equation 5-3

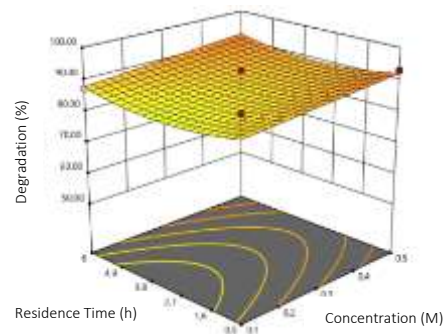
$$= 81,93 - 0,13A - 44,71B - 2,45C + 0,35AB + 0,38C^2$$

**Table 5.2: The degradation as a response of the interaction between residence time and precursor concentration at a reaction temperature of a) 90°C b) 135°C and c) 180°C**

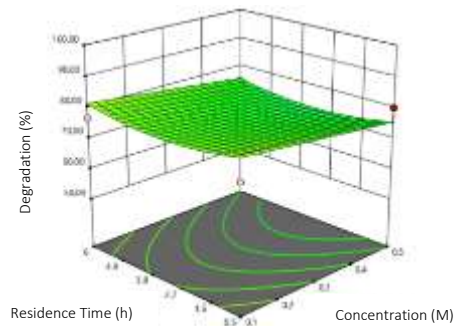


180°C

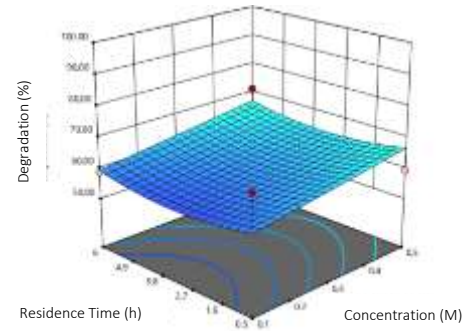
c)



f)



i)



The degradation for  $\text{Co}(\text{NO}_3)_2 \cdot 6\text{H}_2\text{O}$ -derived  $\text{Co}_3\text{O}_4$  nanocatalyst can be seen Table 5.2 a-c, for  $\text{CoCl}_{12} \cdot 6\text{H}_2\text{O}$ -derived  $\text{Co}_3\text{O}_4$  in Table 5.2 d-e, and for  $\text{Co}(\text{C}_2\text{H}_3\text{O}_2)_2$ -derived  $\text{Co}_3\text{O}_4$  in Table 5.2 g- i. It can be seen that at a low precursor concentration there is a decrease in the degradation percentage as the reaction temperature increases from  $90^\circ\text{C}$  to  $180^\circ\text{C}$ . However, at high precursor concentration there is an increase in the degradation percentage as the reaction temperature increases. The degradation of the methyl orange using the  $\text{Co}(\text{NO}_3)_2 \cdot 6\text{H}_2\text{O}$ -derived  $\text{Co}_3\text{O}_4$  nanocatalyst varied between 84.85% and 96.18%. For  $\text{CoCl}_{12} \cdot 6\text{H}_2\text{O}$ -derived  $\text{Co}_3\text{O}_4$  nanocatalyst it varied from 68.62% to 90.17% and for  $\text{Co}(\text{C}_2\text{H}_3\text{O}_2)_2$ -derived  $\text{Co}_3\text{O}_4$  nanocatalyst it varied between 54.31% and 67.93%. Equation 5-1 – Equation 5-3 were used to determine the process parameters for the produced catalyst that achieved the minimum and maximum degradations of MO solution.

A comparison of the minimum degradation percentages for each of the precursor salts is presented in Table 5.3. It can be seen that the minimum degradation is obtained for  $\text{Co}(\text{NO}_3)_2 \cdot 6\text{H}_2\text{O}$ - and  $\text{Co}(\text{C}_2\text{H}_3\text{O}_2)_2$ -derived  $\text{Co}_3\text{O}_4$  nanocatalyst produced at the highest reaction temperatures and lowest precursor concentration, while for  $\text{CoCl}_{12} \cdot 6\text{H}_2\text{O}$ -derived  $\text{Co}_3\text{O}_4$  it is at a lower reaction temperature and highest precursor concentration.

From Table 5.4 it can be seen that for all the precursor salts the maximum degradation percentages were achieved at the lowest reaction temperature and precursor concentration.  $\text{Co}(\text{NO}_3)_2 \cdot 6\text{H}_2\text{O}$ -derived  $\text{Co}_3\text{O}_4$  required the lowest reaction time while  $\text{CoCl}_{12} \cdot 6\text{H}_2\text{O}$ - and  $\text{Co}(\text{C}_2\text{H}_3\text{O}_2)_2$ -derived  $\text{Co}_3\text{O}_4$  required the highest residence time.  $\text{Co}(\text{NO}_3)_2 \cdot 6\text{H}_2\text{O}$ -derived  $\text{Co}_3\text{O}_4$  nanocatalyst had a 6.01% higher efficiency than  $\text{CoCl}_{12} \cdot 6\text{H}_2\text{O}$ -derived  $\text{Co}_3\text{O}_4$  and had a 28.25% higher efficiency than  $\text{Co}(\text{C}_2\text{H}_3\text{O}_2)_2$ -derived  $\text{Co}_3\text{O}_4$ .  $\text{CoCl}_{12} \cdot 6\text{H}_2\text{O}$ -derived  $\text{Co}_3\text{O}_4$  had a 22.24% higher efficiency than  $\text{Co}(\text{C}_2\text{H}_3\text{O}_2)_2$ -derived  $\text{Co}_3\text{O}_4$  nanocatalyst. From here it can be seen that  $\text{Co}(\text{C}_2\text{H}_3\text{O}_2)_2$ -derived  $\text{Co}_3\text{O}_4$  performed the worst while  $\text{Co}(\text{NO}_3)_2 \cdot 6\text{H}_2\text{O}$ -derived  $\text{Co}_3\text{O}_4$  performed the best.

**Table 5.3: Operating parameters for minimum degradation of methyl orange**

Precursor Salt	Reaction Temperature ( $^\circ\text{C}$ )	Precursor Concentration (M)	Residence time (h)	Degradation (%)
Cobalt nitrate hexahydrate ( $\text{Co}(\text{NO}_3)_2 \cdot 6\text{H}_2\text{O}$ )	180	0.1	3.20	84.85
Cobalt chloride hexahydrate ( $\text{CoCl}_{12} \cdot 6\text{H}_2\text{O}$ )	90	0.5	3.20	68.62
Cobaltacetate tetrahydrate ( $\text{Co}(\text{C}_2\text{H}_3\text{O}_2)_2$ )	180	0,1	3.20	56.31

**Table 5.4: Operating parameters for maximum degradation of methyl orange**

Precursor Salt	Reaction Temperature (°C)	Precursor Concentration (M)	Residence time (h)	Degradation (%)
Cobalt nitrate hexahydrate (Co(NO <sub>3</sub> ) <sub>2</sub> ·6H <sub>2</sub> O)	90	0.1	0.5	96.18
Cobalt chloride hexahydrate (CoCl <sub>12</sub> ·6H <sub>6</sub> O)	90	0.1	6	90.17
Cobaltacetate tetrahydrate (Co(C <sub>2</sub> H <sub>3</sub> O <sub>2</sub> ) <sub>2</sub> )	90	0.1	6	67.93

## 5.4 Effect of Co<sub>3</sub>O<sub>4</sub> crystallite size and surface area on the degradation percentage

It was shown in Chapter 4.3 that the crystallite size was affected by the process conditions. Table 5.5 shows the maximum and minimum degradation as a function of the crystallite size of the Co(C<sub>2</sub>H<sub>3</sub>O<sub>2</sub>)<sub>2</sub>- CoCl<sub>12</sub>·6H<sub>6</sub>O - and Co(NO<sub>3</sub>)<sub>2</sub>·6H<sub>2</sub>O-derived Co<sub>3</sub>O<sub>4</sub> nanocatalyst. The effect of the surface area of the best and worst performing Co<sub>3</sub>O<sub>4</sub> nanocatalyst is shown in Table 5.6

**Table 5.5: Degradation percentage vs crystallite size**

Precursor Salt	Maximum Degradation (%)	Crystallite size for Maximum Degradation (nm)	Minimum Degradation (%)	Crystallite size for Minimum Degradation (nm)
Cobalt nitrate hexahydrate (Co(NO <sub>3</sub> ) <sub>2</sub> ·6H <sub>2</sub> O)	96.16	12.92	84.85	13.26
Cobalt chloride hexahydrate (CoCl <sub>12</sub> ·6H <sub>6</sub> O)	90.17	8.69	68.62	16.15
Cobalt acetate tetrahydrate (Co(C <sub>2</sub> H <sub>3</sub> O <sub>2</sub> ) <sub>2</sub> )	67.93	7.42	56.31	13.34

A comparison between the crystallite size at the maximum and minimum degradation percentage showed that for:

- Co(NO<sub>3</sub>)<sub>2</sub>·6H<sub>2</sub>O-derived Co<sub>3</sub>O<sub>4</sub> the crystallite size for maximum degradation was 2.64% lower than that for the Co<sub>3</sub>O<sub>4</sub> crystallite size obtained at the minimum degradation, but the degradation was 11.31% higher.
- CoCl<sub>12</sub>·6H<sub>6</sub>O -derived Co<sub>3</sub>O<sub>4</sub> the crystallite size for maximum degradation was 46.19% lower than that for the Co<sub>3</sub>O<sub>4</sub> crystallite size obtained at the minimum degradation but the degradation was 21.55% higher.
- Co(C<sub>2</sub>H<sub>3</sub>O<sub>2</sub>)<sub>2</sub>-derived Co<sub>3</sub>O<sub>4</sub> the crystallite size for maximum degradation was 30.61% lower than that for the Co<sub>3</sub>O<sub>4</sub> crystallite size obtained at the minimum degradation but the degradation was 13.62% higher.

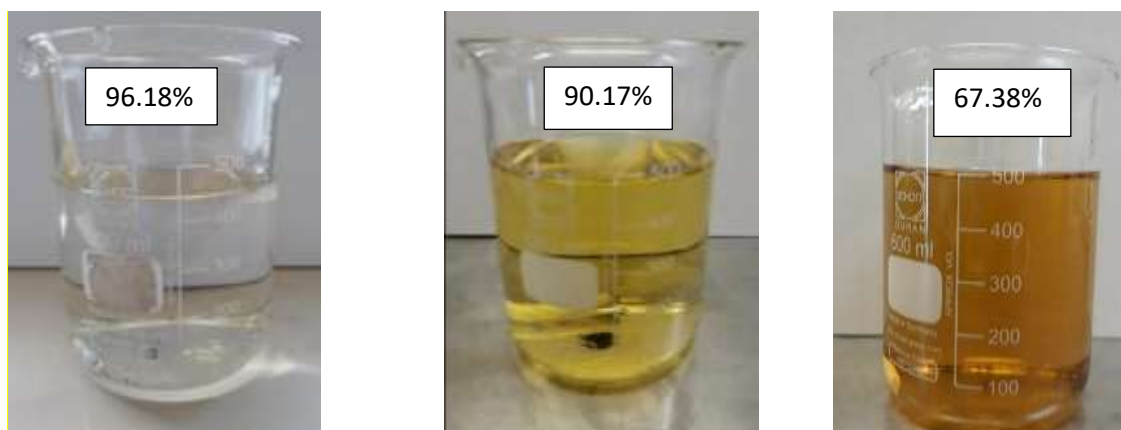
BET analysis was done on the worst and best performing synthesised  $\text{Co}_3\text{O}_4$  nanoparticles in order to investigate the relationship between the active surface area and its degradation potential. Table 5.6 shows comparisons between the degradation percentage, produced yield and surface area of the best and worst  $\text{Co}(\text{C}_2\text{H}_3\text{O}_2)_2^-$ ,  $\text{CoCl}_{12}\cdot 6\text{H}_2\text{O}$  - and  $\text{Co}(\text{NO}_3)_2\cdot 6\text{H}_2\text{O}$ -derived  $\text{Co}_3\text{O}_4$  nanocatalyst.

**Table 5.6: Degradation percentage vs the surface area of the best and worst  $\text{Co}_3\text{O}_4$  nanocatalyst**

Precursor Salt	Degradation of maximum performing sample (%)	Crystallite size for Maximum Degradation (nm)	Surface area ( $\text{m}^2/\text{g}$ )	Degradation of worst performing sample (%)	Crystallite size for Minimum Degradation (nm)	Surface area ( $\text{m}^2/\text{g}$ )
Cobalt nitrate hexahydrate ( $\text{Co}(\text{NO}_3)_2\cdot 6\text{H}_2\text{O}$ )	96.16	12.92	106.35	84.85	13.26	30.72
Cobalt chloride hexahydrate ( $\text{CoCl}_{12}\cdot 6\text{H}_2\text{O}$ )	90.17	8.69	41.06	68.62	16.15	13.27
Cobalt acetate tetrahydrate ( $\text{Co}(\text{C}_2\text{H}_3\text{O}_2)_2$ )	67.93	7.42	43.16	56.31	13.34	5.1

- For  $\text{Co}(\text{NO}_3)_2\cdot 6\text{H}_2\text{O}$ -derived  $\text{Co}_3\text{O}_4$  the surface area was 71.10% higher in surface area and it had a 10.93% higher degradation percentage.
- For  $\text{CoCl}_{12}\cdot 6\text{H}_2\text{O}$  -derived  $\text{Co}_3\text{O}_4$  the surface area was 69.19% higher in surface area and it had a 27,18% higher degradation percentage.
- For  $\text{Co}(\text{C}_2\text{H}_3\text{O}_2)_2$ -derived  $\text{Co}_3\text{O}_4$  the surface area was 91.29% higher in surface area and it had a 21,25% higher degradation percentage.

A clear relationship between the surface area of the  $\text{Co}_3\text{O}_4$  nanocatalyst and its degradation potential is observed. The treated samples of MO solution can be seen in Figure 5.4.



Cobalt nitrate hexahydrate  
( $\text{Co}(\text{NO}_3)_2 \cdot 6\text{H}_2\text{O}$ )

Cobalt chloride hexahydrate  
( $\text{CoCl}_2 \cdot 6\text{H}_2\text{O}$ )

Cobalt acetate tetrahydrate  
( $\text{Co}(\text{C}_2\text{H}_3\text{O}_2)_2$ )

**Figure 5.4 Degradation of MO using  $\text{Co}(\text{NO}_3)_2 \cdot 6\text{H}_2\text{O}$  -,  $\text{CoCl}_2 \cdot 6\text{H}_2\text{O}$  – and  $\text{Co}(\text{C}_2\text{H}_3\text{O}_2)_2$  derived  $\text{Co}_3\text{O}_4$**

## 5.5 Final summary based on the findings

The degradation percentage was always higher in the following order of precursor salt used:  $\text{Co}(\text{NO}_3)_2 \cdot 6\text{H}_2\text{O} > \text{CoCl}_2 \cdot 6\text{H}_2\text{O} > \text{Co}(\text{C}_2\text{H}_3\text{O}_2)_2$ .  $\text{Co}(\text{NO}_3)_2 \cdot 6\text{H}_2\text{O}$  -derived  $\text{Co}_3\text{O}_4$  nanocatalyst had the highest degradation rates in comparison with the degradation rates that was found for the  $\text{Co}_3\text{O}_4$  nanocatalyst produced by the other two precursor salts. A comparison of the crystallite size of the minimum and maximum degradation showed that regardless of the precursor salt, a lower crystallite size resulted in higher degradation.

At higher surface areas, the degradation of MO is higher. During the degradation of methyl orange dye solution it was found that the  $\text{Co}_3\text{O}_4$  nanoparticles calcined from  $\beta\text{-Co}(\text{OH})_2$  performed worst and had slower reaction rates in comparison with degradation and reaction rates that was observed from  $\text{Co}_3\text{O}_4$  nanoparticles calcined from  $\alpha\text{-Co}(\text{OH})_2$ . This contradicts the findings from Heuvel (2020) where during the degradation of methylene blue dye solution the  $\text{Co}_3\text{O}_4$  nanoparticles calcined from  $\beta\text{-Co}(\text{OH})_2$  had higher reaction rates in comparison than what was observed from  $\text{Co}_3\text{O}_4$  nanoparticles calcined from  $\alpha\text{-Co}(\text{OH})_2$ . The amorphous samples as shown in the Figure 4.1 c) all performed as well as the crystalline samples, all had a degradation percentage higher than 78%. The additional diffraction peaks for  $\text{CoCl}_2 \cdot 6\text{H}_2\text{O}$  precursor salt indicated in the XRD pattern is a possible explanation to why the  $\text{CoCl}_2 \cdot 6\text{H}_2\text{O}$  -derived  $\text{Co}_3\text{O}_4$  nanocatalyst performed worse than the  $\text{Co}(\text{NO}_3)_2 \cdot 6\text{H}_2\text{O}$  -derived  $\text{Co}_3\text{O}_4$  nanocatalyst.

Study done by Saputra et al. (2017) on the production of  $\text{Co}_3\text{O}_4$  with different morphologies namely cubic, spherical and truncated cube. The BET analysis showed that the surface and pore volume of the produced particles increases in the order of sphere, truncated cube and cube. However, it was found during the degradation of phenol, the activity of the  $\text{Co}_3\text{O}_4$  particles increased in the order of truncated cube, sphere and cube. This concurs with the findings for this study where  $\text{Co}(\text{C}_2\text{H}_3\text{O}_2)_2$ - derived  $\text{Co}_3\text{O}_4$  nanocatalyst had a higher surface area than  $\text{CoCl}_{12}\cdot 6\text{H}_2\text{O}$  -derived  $\text{Co}_3\text{O}_4$  nanocatalyst but performed worst during the degradation of MO. The difference in the behaviour for  $\text{CoCl}_{12}\cdot 6\text{H}_2\text{O}$  -derived  $\text{Co}_3\text{O}_4$  in comparison to that of  $\text{Co}(\text{NO}_3)_2\cdot 6\text{H}_2\text{O}$  - and  $\text{Co}(\text{C}_2\text{H}_3\text{O}_2)_2$ - derived  $\text{Co}_3\text{O}_4$  during the degradation of MO shows that a possible other mechanism affects the performance of the nanocatalyst and this phenomena requires further investigation.

## Chapter 6 Cost comparison analysis on the production cost of $\text{Co}_3\text{O}_4$ via various precursors

The aim of this chapter is to evaluate the cost that is involved in the production of  $\text{Co}_3\text{O}_4$  nanocatalyst and the treatment of wastewater using the produced nanocatalyst. The synthesis cost of the catalyst is determined by taking the following into account: (1) the type of precursor salt used, (2) the quantity of precursor salt used in each experimental run and (3) the reaction temperature and residence time. The process parameters for the production of each sample can be found in Table 4.1. The cost for the treatment of 500 mL of MO (methyl orange) solution was determined by taking the catalyst cost and Oxone<sup>®</sup> cost into account.

In order to gain a fundamental understanding of the cost that is involved in the synthesis of  $\text{Co}_3\text{O}_4$  nanocatalyst and the treatment of methyl orange solution using the produced nanocatalyst, the cost of laboratory grade chemicals was used. The synthesis and treatment cost were calculated according to the Sigma-Aldrich<sup>®</sup> 2021 prices. Table 6.1 shows the price for each chemical that was used in this study.

**Table 6.1: Chemical product cost**

Product Description	Pricing	Price per gram
Cobalt nitrate hexahydrate ( $\text{Co}(\text{NO}_3)_2 \cdot 6\text{H}_2\text{O}$ )	R 6404/ 500 g	R 12.81/g
Cobalt chloride hexahydrate ( $\text{CoCl}_2 \cdot 6\text{H}_2\text{O}$ )	R 3638/100 g	R 36.38/g
Cobalt acetate tetrahydrate ( $\text{Co}(\text{C}_2\text{H}_3\text{O}_2)_2$ )	R 6426/500 g	R 12.85/g
Ammonium hydroxide solution ( $\text{NH}_4\text{OH}$ )	R 1261/L	R 1.26/mL
Permonopersulfate Oxone <sup>®</sup> ( $\text{KHSO}_5 \cdot 0.5 \text{KHSO}_4 \cdot 0.5 \text{K}_2\text{SO}_4$ )	R 666/100 g	R 6.66/g

### 6.1 Calculation of cost

Equation 6-1 was used to calculate the synthesis cost per unit  $\text{Co}_3\text{O}_4$  produced from each batch experiment. The synthesis cost is equal to the cost of the precursor salt, the ammonium nitrate, electricity cost during hydrothermal synthesis and the electricity cost for calcination divided by the total yield obtained per run. This calculation takes the precursor concentration into account. The quantity of each chemical substance required for the given precursor concentration is given in Table 3.2. The electricity cost was taken as the electricity cost for the synthesis time and calcination time and can be seen in Equation 6-2. The calculation takes the following into account (1) current City of Cape Town power rate of R 2.72/kWh was used,

(2) the reaction temperature as a percentage of the oven capacity, (3) power of the oven and (4) the residence time.

Equation 6-1

$$\text{Synthesis cost} \left( \frac{R}{g} \right) = \frac{(\text{Precursor salt} + \text{Ammonium hydroxide solution}) + (\text{Electricity usage}_{\text{Production}} + \text{Electricity usage}_{\text{Calcination}})}{\text{Produced yield}}$$

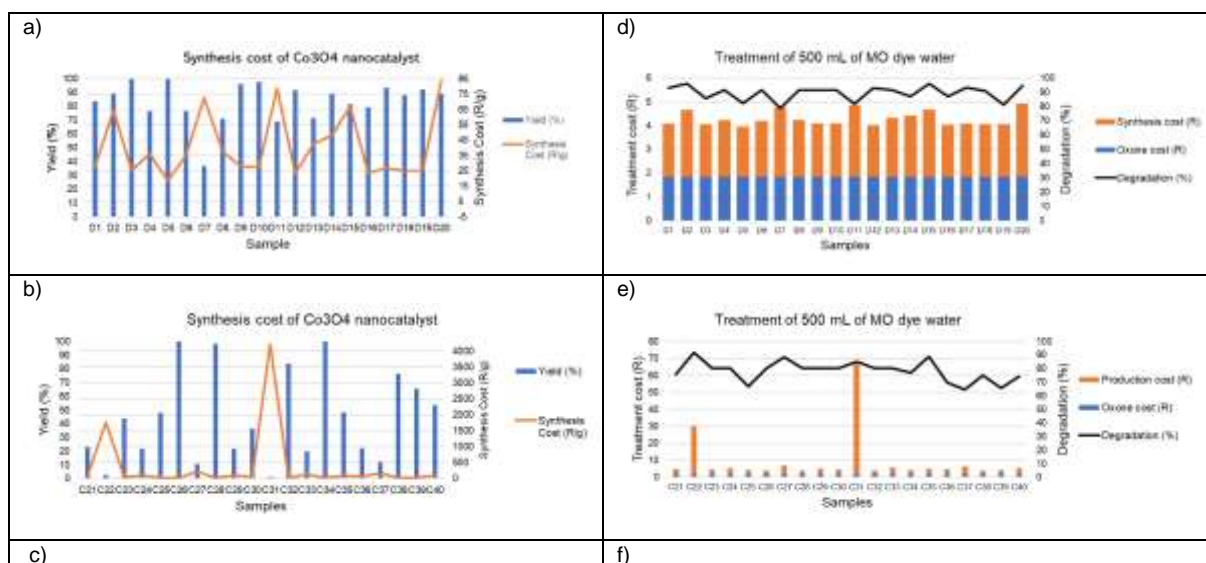
$$\text{Electricity usage (R)} = \text{Power rate} + (\text{capacity usage}) * (\text{Power}) * (\text{Residence time}) \quad \text{Equation 6-2}$$

The costing calculation for the treatment process 500 mL of MO solution is given in Equation 6-3. The synthesis cost that is calculated in Equation 6-1 for each experimental run is multiplied by the 0.015 g of produced  $\text{Co}_3\text{O}_4$  nanocatalyst used and the cost for 0.28 g of Oxone® is added.

$$\text{Treatment cost (R)} = (\text{synthesis cost} * 0.015) + \text{Oxone}^{\circledR} \text{ cost} \quad \text{Equation 6-3}$$

Table 6.2 a – c shows  $\text{Co}_3\text{O}_4$  produced yield versus the synthesis cost of the nanocatalyst. Table 6.2 d – f shows the treatment cost of 500 mL of MO solution versus the degradation percentage. In Table 6.2 d – f the treatment cost consists out of the synthesis cost of 0.015 g produced  $\text{Co}_3\text{O}_4$  nanocatalyst (indicated in orange in the graphs) and the cost of 0.28 g of Oxone® (indicated in blue in the graphs).

**Table 6.2: Production and treatment cost of  $\text{Co}_3\text{O}_4$  nanocatalyst**



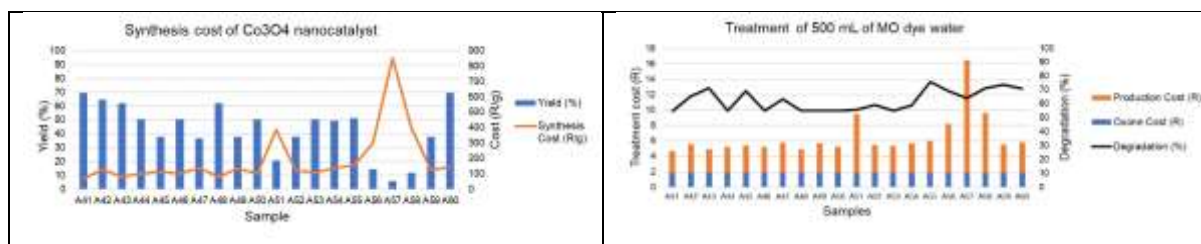


Table 6.2 a) shows the  $\text{Co}(\text{NO}_3)_2 \cdot 6\text{H}_2\text{O}$ -derived  $\text{Co}_3\text{O}_4$  yield versus the synthesis cost. All samples from  $\text{Co}(\text{NO}_3)_2 \cdot 6\text{H}_2\text{O}$  precursor are represented by D. Sample D5 has the lowest synthesis cost in this batch while sample D20 has the highest cost. Sample D5 has a 10.82% higher  $\text{Co}_3\text{O}_4$  yield with a 63.47% lower synthesis cost, in comparison with sample D20. Both sample D5 and D3 has a 100% yield; sample C3 has a 14.84% higher synthesis cost.

From Table 6.2 b) the yield versus the synthesis cost for  $\text{CoCl}_{12} \cdot 6\text{H}_2\text{O}$ -derived  $\text{Co}_3\text{O}_4$  can be seen. All samples from  $\text{CoCl}_{12} \cdot 6\text{H}_2\text{O}$  precursor are represented by C. Sample C32 has the lowest synthesis cost in this batch while sample C31 has the highest. Sample C32 has an 82.88% higher yield  $\text{Co}_3\text{O}_4$  with a 98.96% lower synthesis cost, in comparison with sample C31. Both sample C34 and C26 has a 100% yield; sample C34 has a 20.94% higher synthesis cost.

The yield versus the synthesis cost for  $\text{Co}(\text{C}_2\text{H}_3\text{O}_2)_2$ -derived  $\text{Co}_3\text{O}_4$  can be found in Table 6.2 c). All samples from  $\text{Co}(\text{C}_2\text{H}_3\text{O}_2)_2$  precursor are represented by A. Sample A41 has the lowest synthesis cost in this batch while sample A57 has the highest. Sample A41 has an 63.48% higher  $\text{Co}_3\text{O}_4$  yield with an 85.40% lower synthesis cost, in comparison with sample A5. Both samples A41 and A60 has a yield of 69% with sample A41 having a 36.33% lower synthesis cost.

A comparison of the synthesis costs of the produced nanocatalyst via the three different precursors can be seen in Figure 6.1 and Figure 6.2. Figure 6.1 shows a comparison of the synthesis cost involves the catalyst produced at the same operating parameters. The catalyst produced using  $\text{CoCl}_{12} \cdot 6\text{H}_2\text{O}$  - precursor salt had the overall highest synthesis cost. Sample C31 has the overall highest synthesis cost while sample D5 has the lowest cost. Figure 6.2 shows the highest yield produced for each precursor as a function of the synthesis cost. The yield for both  $\text{CoCl}_{12} \cdot 6\text{H}_2\text{O}$  and  $\text{Co}(\text{NO}_3)_2 \cdot 6\text{H}_2\text{O}$  precursors resulted in a 100% while yield for  $\text{Co}(\text{C}_2\text{H}_3\text{O}_2)_2$  precursor was 69.63%.  $\text{Co}(\text{C}_2\text{H}_3\text{O}_2)_2$  precursor had the highest synthesis cost with a 30.37% lower product yield. Samples produced by  $\text{Co}(\text{NO}_3)_2 \cdot 6\text{H}_2\text{O}$  precursor had a lower synthesis cost in comparison with the other two precursors. Sample D5 had the lowest operating parameter requirements to achieve maximum yield in comparison to the other samples that had higher requirements, as illustrated in Table 6.3.

Table 6.3: Process conditions for highest yield producing samples for synthesis cost

Run	Reaction Temperature (°C)	Precursor Concentration (M)	Residence time (h)	Precursor	Yield (%)	Degradation (%)
D3	135	0.3	6	Co(NO <sub>3</sub> ) <sub>2</sub> ·6H <sub>2</sub> O	100	85.64
D5	90	0.5	0.5	Co(NO <sub>3</sub> ) <sub>2</sub> ·6H <sub>2</sub> O	100	82.44
C26	135	0.3	3.25	CoCl <sub>12</sub> ·6H <sub>6</sub> O	100	80.26
C34	180	0.1	6	CoCl <sub>12</sub> ·6H <sub>6</sub> O	100	76.79
A41	180	0.3	3.25	Co(C <sub>2</sub> H <sub>3</sub> O <sub>2</sub> ) <sub>2</sub>	69.34	54.62

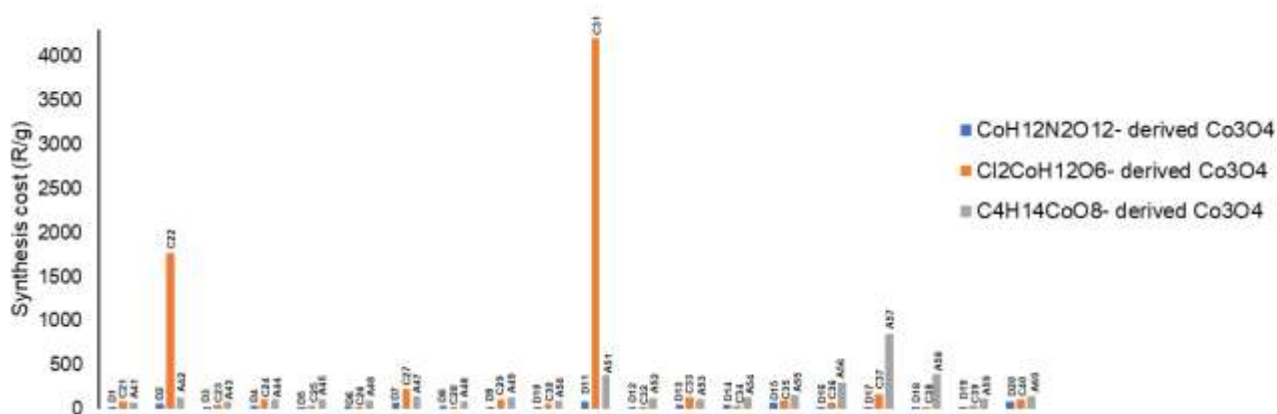


Figure 6.1: Comparison of the synthesis cost of cobalt precursors

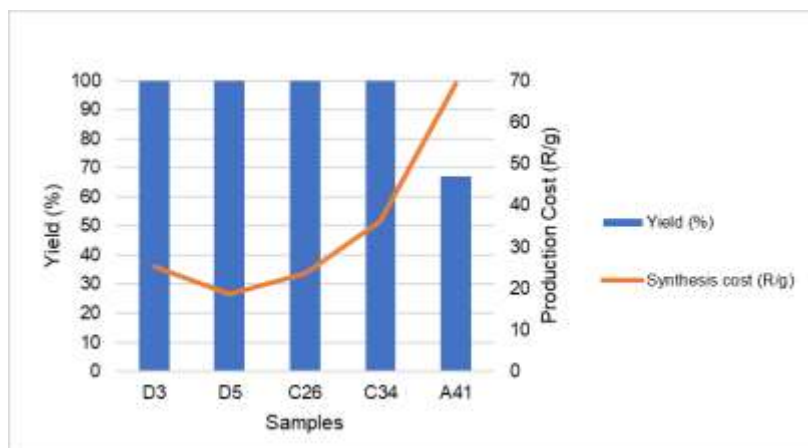


Figure 6.2: Comparison of production cost for different precursor salts at the highest produced yield

The treatment cost for 500 mL of MO solution for each precursor salt is found in Table 6.2 d – f. For Co(NO<sub>3</sub>)<sub>2</sub>·6H<sub>2</sub>O-derived Co<sub>3</sub>O<sub>4</sub> the treatment cost vs the degradation percentage can be found in Table 6.2 d. Sample D20 had the highest treatment cost while sample D5 had the lowest treatment cost. Sample D5 had a 12.30% lower degradation percentage than sample

D20 while the treatment cost for D5 was 10.96% lower. Sample D15 (best performing sample) had a 13.71% higher degradation and a 8.36% higher treatment cost than sample D5.

For  $\text{CoCl}_{12}\cdot 6\text{H}_2\text{O}$  -derived  $\text{Co}_3\text{O}_4$  the treatment cost vs the degradation percentage can be seen in Table 6.2 e). Comparing the samples that had the highest and lowest degradation percentages it was found that sample C22 (best performing sample) had a 42.82% higher degradation than sample C37 (worst performing sample) while the treatment cost was 65.67% higher than C37. Sample C32 had the lowest treatment cost while sample C31 had the highest. Sample C31 had an 5.13% higher degradation percentage with an 88.68% higher treatment cost in comparison to that of sample C32.

$\text{Co}(\text{C}_2\text{H}_3\text{O}_2)_2$ -derived  $\text{Co}_3\text{O}_4$  treatment cost vs the degradation percentage can be seen in Table 6.2 f). Comparing the samples that had the highest and lowest degradation percentages it was found that sample A55 (best performing sample) had a 21.25% higher degradation than sample A41 (worst performing sample). The treatment cost for A41 was 12.35% lower than that for A55. Sample A41 had the lowest treatment cost while sample C57 had the highest. Sample A57 had a 9.48% higher degradation percentage with an 55.67% higher treatment cost in comparison to that of sample A41.

A comparison of the treatment costs of the produced nanocatalyst via the three different precursors can be seen in Figure 6.3 and Figure 6.4. The comparison of the treatment cost for each catalyst produced under the same operating parameters is found in Figure 6.3.  $\text{Co}(\text{NO}_3)_2\cdot 6\text{H}_2\text{O}$ -derived  $\text{Co}_3\text{O}_4$  nanocatalyst had the overall highest degradation percentage with the lowest synthesis cost.  $\text{CoCl}_{12}\cdot 6\text{H}_2\text{O}$  - and  $\text{Co}(\text{C}_2\text{H}_3\text{O}_2)_2$ -derived precursor salts had the highest treatment cost due to the high synthesis cost. The comparison between the treatment cost for the best performing samples and the samples that had the lowest treatment cost from each precursor salt can be seen in Figure 6.4 and the process conditions for these samples can be seen in Table 6.4.

Sample D5 had the lowest treatment cost for 500 mL of MO with a degradation percentage of 82.44% while the best performing sample (D15) had a 26.50% higher treatment cost with 13.71% higher degradation percentage. The sample with the highest treatment cost (C22) had a 4.48% lower degradation percentage than D15 with an 73.16% higher treatment cost.

**Table 6.4: Process conditions for the best performing samples and the samples that had the lowest treatment cost**

Run	Reaction Temperature (°C)	Precursor Concentration (M)	Residence time (h)	Precursor	Degradation (%)	
D5	90	0.5	0.5	Co(NO <sub>3</sub> ) <sub>2</sub> ·6H <sub>2</sub> O	82.44	Lowest treatment cost
D15	90	0.1	0,5	Co(NO <sub>3</sub> ) <sub>2</sub> ·6H <sub>2</sub> O	96.15	Highest degradation
C32	180	0.5	0.5	CoCl <sub>12</sub> ·6H <sub>6</sub> O	80.13	Lowest treatment cost
C22	90	0.1	6	CoCl <sub>12</sub> ·6H <sub>6</sub> O	91.67	Highest degradation
A41	180	0.3	3.25	Co(C <sub>2</sub> H <sub>3</sub> O <sub>2</sub> ) <sub>2</sub>	54.62	Lowest treatment cost
A55	90	0.1	0.5	Co(C <sub>2</sub> H <sub>3</sub> O <sub>2</sub> ) <sub>2</sub>	75.87	Highest degradation

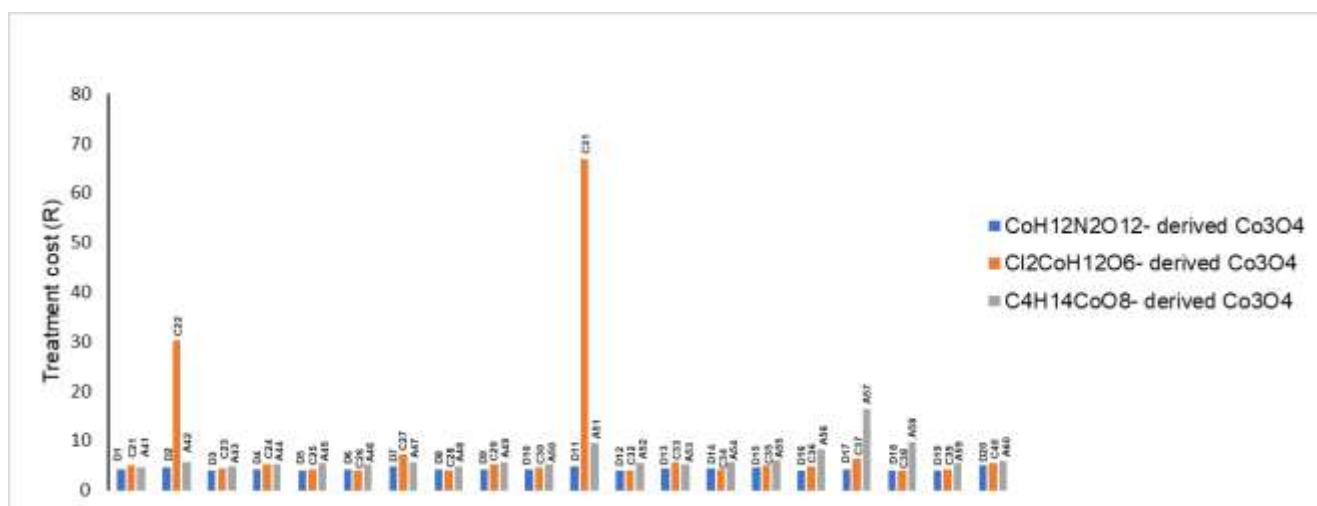


**Figure 6.3: Comparison of the treatment cost**

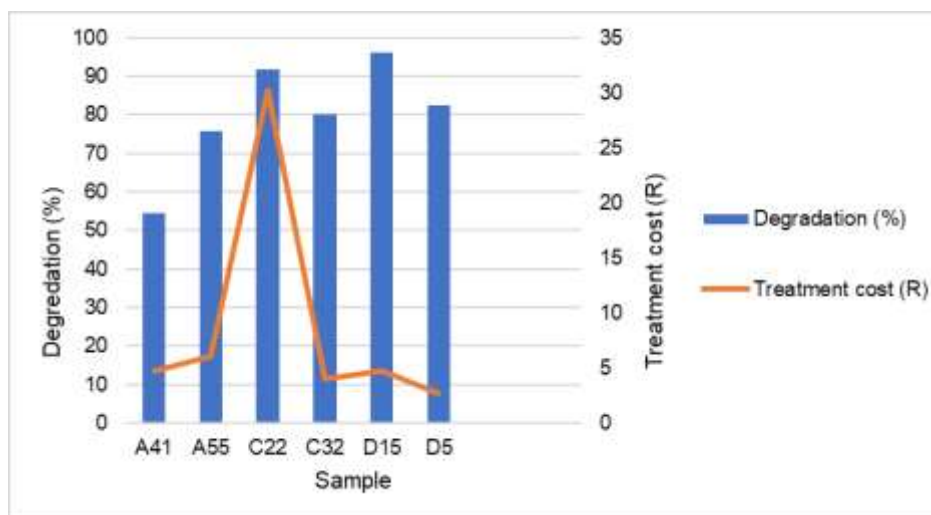


**Figure 6.4: Comparison of treatment cost using different precursor salts**

This preliminary cost comparison study can be used to evaluate the viability of a full-scale treatment process. From this study it was found that  $\text{Co}(\text{NO}_3)_2 \cdot 6\text{H}_2\text{O}$ -derived  $\text{Co}_3\text{O}_4$  nanocatalyst was the most cost efficient and showed the best performance in the treatment of MO solution. The production process involved low reaction temperature and residence time to achieve the maximum yield whereas  $\text{CoCl}_{12} \cdot 6\text{H}_2\text{O}$  - and  $\text{Co}(\text{C}_2\text{H}_3\text{O}_2)_2$ -derived precursor salts had the higher requirements for the process conditions.

Upscaling the process using  $\text{Co}(\text{NO}_3)_2 \cdot 6\text{H}_2\text{O}$  precursor sample D15 (process conditions:  $90^\circ\text{C}$ , 0.1 M, 30 minutes, 81.74% yield), 39 batches of 500 mL MO solution can be treated (20 L) with a degradation percentage of 96.15%. Using sample D5 (process conditions:  $90^\circ\text{C}$ , 0.5 M, 30 minutes, 100% yield) 243 batches of 500mL MO can be treated (121 L) with a degradation percentage of 82.44%. Further investigations on effect of the catalyst concentration for the degradation of wastewater is required. For example, by using sample D5 the concentration during the treatment can be doubled to 0.03 g/ 500 mL ensuring that the degradation percentage is significantly closer to 100%. In this scenario the using sample D5 will treat 60 L of MO solution which is three times more than the sample D15 which provided the highest degradation.

## 6.2 Conclusions

This preliminary cost comparison study showed that  $\text{Co}(\text{NO}_3)_2 \cdot 6\text{H}_2\text{O}$  -derived  $\text{Co}_3\text{O}_4$  nanocatalyst was the most cost efficient while the catalyst produced from  $\text{CoCl}_{12} \cdot 6\text{H}_2\text{O}$  - precursor salt had the overall highest synthesis cost. Sample D5 had the overall lowest synthesis cost with a 100% yield, while A41 had the highest synthesis cost with a 67.12% yield. For both  $\text{Co}(\text{NO}_3)_2 \cdot 6\text{H}_2\text{O}$  – precursor (D3, D5) and for  $\text{CoCl}_{12} \cdot 6\text{H}_2\text{O}$  - precursor

(C26,C34) the maximum producing samples achieved a 100% yield with a lower synthesis cost in comparison with sample A41, derived from  $\text{Co}(\text{C}_2\text{H}_3\text{O}_2)_2$ -derived, that has a yield of 67.12%.

This cost comparison analysis found that  $\text{Co}(\text{NO}_3)_2 \cdot 6\text{H}_2\text{O}$  -derived  $\text{Co}_3\text{O}_4$  nanocatalyst was the most cost efficient and provided with the best performance in the treatment of MO solution. The required process parameters for production process involved lower reaction temperature and residence time to achieve the maximum yield whereas the higher process conditions were required for  $\text{CoCl}_2 \cdot 6\text{H}_2\text{O}$  and  $\text{Co}(\text{C}_2\text{H}_3\text{O}_2)_2$  precursor salts.

## Chapter 7 Conclusions and Recommendations

### 7.1. Introduction

This study aimed to firstly determine the optimal conditions for maximum yield of  $\text{Co}_3\text{O}_4$  nanoparticles synthesised using  $\text{Co}(\text{NO}_3)_2 \cdot 6\text{H}_2\text{O}$ -,  $\text{CoCl}_{12} \cdot 6\text{H}_2\text{O}$  - and  $\text{Co}(\text{C}_2\text{H}_3\text{O}_2)_2$ -derived precursor solution by the hydrothermal synthesis process. Secondly, to evaluate the efficiency of the produced nanocatalyst in the degradation of synthetic textile wastewater using an advanced oxidation process followed by a cost evaluation.

### 7.2. Conclusions

This section summarises (1) the production of nano  $\text{Co}_3\text{O}_4$  particles derived by  $\text{Co}(\text{NO}_3)_2 \cdot 6\text{H}_2\text{O}$ ,  $\text{CoCl}_{12} \cdot 6\text{H}_2\text{O}$  and  $\text{Co}(\text{C}_2\text{H}_3\text{O}_2)_2$  precursor solution under various process conditions and (2) the treatment of MO solution using the produced nanocatalyst.

After the hydrothermal synthesis process,  $\text{CoCl}_{12} \cdot 6\text{H}_2\text{O}$  - and  $\text{Co}(\text{NO}_3)_2 \cdot 6\text{H}_2\text{O}$  - $\text{Co}(\text{OH})_2$  nanoparticles had a green/blue colour and were identified as  $\alpha$ - $\text{Co}(\text{OH})_2$ .  $\text{Co}(\text{C}_2\text{H}_3\text{O}_2)_2$  precursor solution produced  $\text{Co}(\text{OH})_2$  with a pink/brown colour and was identified as  $\beta$ - $\text{Co}(\text{OH})_2$ . XRD analysis showed that after 3 hours calcination at  $350^\circ\text{C}$ ,  $\text{Co}_3\text{O}_4$  powders were produced.

#### 7.2.1 Effect of process conditions on product yield

For  $\text{Co}(\text{NO}_3)_2 \cdot 6\text{H}_2\text{O}$  - and  $\text{Co}(\text{C}_2\text{H}_3\text{O}_2)_2$  -derived  $\text{Co}_3\text{O}_4$ , the product yield was stable over the temperature range in comparison with  $\text{CoCl}_{12} \cdot 6\text{H}_2\text{O}$  where the product yield increased 40%. The product yield for  $\text{Co}(\text{NO}_3)_2 \cdot 6\text{H}_2\text{O}$  - and  $\text{Co}(\text{C}_2\text{H}_3\text{O}_2)_2$  -derived  $\text{Co}_3\text{O}_4$  increased with 7.24% and 8.12% respectively. This trend was independent of precursor salt concentration. An increase in the precursor salt concentration of  $\text{Co}(\text{NO}_3)_2 \cdot 6\text{H}_2\text{O}$  and  $\text{CoCl}_{12} \cdot 6\text{H}_2\text{O}$  will result in an increase of the product yield while the product yield for  $\text{Co}(\text{C}_2\text{H}_3\text{O}_2)_2$  will decrease. It was found that the product yield was least affected by changes in the residence time.

Table 7.1 shows the summary of the effect of the operating parameters over the full range of conditions on the yield of the produced  $\text{Co}_3\text{O}_4$ .

**Table 7.1: Range of Co<sub>3</sub>O<sub>4</sub> yield produced and optimal operating parameters**

Precursor salt	Production range	Maximum Co <sub>3</sub> O <sub>4</sub> production yield operating parameters for maximum yield		
		Reaction Temperature (°C)	Precursor Concentration (M)	Residence time (h)
Co(NO <sub>3</sub> ) <sub>2</sub> ·6H <sub>2</sub> O –derived Co <sub>3</sub> O <sub>4</sub>	56% to 100%	130	0.3	0.5
CoCl <sub>12</sub> ·6H <sub>2</sub> O –derived Co <sub>3</sub> O <sub>4</sub>	1% to 82%	180	0.3	0.5
Co(C <sub>2</sub> H <sub>3</sub> O <sub>2</sub> ) <sub>2</sub> –derived Co <sub>3</sub> O <sub>4</sub>	12% to 66%	180	0.2	6

Comparing the maximum yield obtained for each precursor the order was as follows: Co(NO<sub>3</sub>)<sub>2</sub>·6H<sub>2</sub>O (100%) > CoCl<sub>12</sub>·6H<sub>2</sub>O (82%) > Co(C<sub>2</sub>H<sub>3</sub>O<sub>2</sub>)<sub>2</sub> (66%).

**Table 7.2: Effect of operating parameters on Co<sub>3</sub>O<sub>4</sub> product yield**

Precursor	↑ Temperature (°C)	↑ Residence time (h)	↑ Concentration (M)
Co(NO <sub>3</sub> ) <sub>2</sub> ·6H <sub>2</sub> O –derived Co <sub>3</sub> O <sub>4</sub>	Increase ↑	Moderate increase ↑	Increase ↑
CoCl <sub>12</sub> ·6H <sub>2</sub> O –derived Co <sub>3</sub> O <sub>4</sub>	Major increase ↑	Moderate increase ↑	Increase ↑
Co(C <sub>2</sub> H <sub>3</sub> O <sub>2</sub> ) <sub>2</sub> –derived Co <sub>3</sub> O <sub>4</sub>	Increase ↑	Moderate decrease ↓	Major decrease ↓

## 7.2.2 Effect of process conditions on crystallite size

The crystallite size of Co(NO<sub>3</sub>)<sub>2</sub>·6H<sub>2</sub>O and Co(C<sub>2</sub>H<sub>3</sub>O<sub>2</sub>)<sub>2</sub> precursor-derived Co<sub>3</sub>O<sub>4</sub> presented the same trends. The largest crystallite sizes were found at the highest reaction temperature and the lowest residence time and precursor concentration. Whereas the smallest crystallite sizes were found at the lowest reaction temperature and residence time and the highest precursor concentration. It was found that the crystallite size decreased as the residence time was increased. At the lowest reaction temperature and highest precursor concentration there was an increase in the crystallite size as the residence time increased. The crystallite size increased as the reaction temperature increased and decreased as the precursor concentration increased. At the lowest residence time and highest reaction temperature, there was a decrease in crystallite size as the precursor concentration increase. It was found that at highest residence time the interaction of the precursor concentration is less significant in comparison with the significance of the interaction at the lowest residence time

For  $\text{CoCl}_{12}\cdot 6\text{H}_2\text{O}$  –derived  $\text{Co}_3\text{O}_4$  nanoparticles the largest crystallite sizes are found at the lowest reaction temperature and residence time and the highest precursor concentration. Whereas the smallest crystallite sizes are found intermediate process conditions. An increase in the residence time resulted in an increase in crystallite size at the lowest reaction temperature and highest precursor concentration while a decrease is observed at the highest reaction temperature and lowest precursor concentration. The interaction between the residence time and precursor concentration, at the lowest reaction temperature, was more significant at the highest residence time. Across the residence time range there was a decrease in the crystallite size between a precursor concentration range of 0.1 M and 0.3 M and a significant increase between a precursor concentration of 0.3 M and 0.5 M.

Table 7.3 gives the ranges of crystallite sizes of the  $\text{Co}_3\text{O}_4$  nanoparticles produced by  $\text{Co}(\text{NO}_3)_2\cdot 6\text{H}_2\text{O}$  -,  $\text{CoCl}_{12}\cdot 6\text{H}_2\text{O}$  - and  $\text{Co}(\text{C}_2\text{H}_3\text{O}_2)_2$  -precursor salts.

**Table 7.3: Crystallite sizes of  $\text{Co}_3\text{O}_4$  nanoparticles**

Precursor salt	Crystallite range
$\text{Co}(\text{NO}_3)_2\cdot 6\text{H}_2\text{O}$ –derived $\text{Co}_3\text{O}_4$	4.15 nm to 21.22 nm
$\text{CoCl}_{12}\cdot 6\text{H}_2\text{O}$ –derived $\text{Co}_3\text{O}_4$	3.06 nm to 17.97 nm
$\text{Co}(\text{C}_2\text{H}_3\text{O}_2)_2$ –derived $\text{Co}_3\text{O}_4$	4.15 nm to 21.22 nm

### 7.2.3 Degradation of MO solution by synthesised $\text{Co}_3\text{O}_4$ nanocatalyst

The synthesised  $\text{Co}_3\text{O}_4$  nanoparticles that were produced using  $\text{Co}(\text{C}_2\text{H}_3\text{O}_2)_2$ ,  $\text{CoCl}_{12}\cdot 6\text{H}_2\text{O}$  and  $\text{Co}(\text{NO}_3)_2\cdot 6\text{H}_2\text{O}$  precursor salts under various process conditions (reaction temperature, precursor concentration and residence time) and used as a nanocatalyst for the degradation of methyl orange dye. The final degradation result obtained for each catalyst at the end of 30 minutes was included as a response in the Design-Expert factorial trial and the following was found: for the precursor salts, the maximum degradation percentages were achieved at the lowest reaction temperature and precursor concentration.  $\text{Co}(\text{NO}_3)_2\cdot 6\text{H}_2\text{O}$  -derived  $\text{Co}_3\text{O}_4$  required the lowest reaction time while  $\text{CoCl}_{12}\cdot 6\text{H}_2\text{O}$  - and  $\text{Co}(\text{C}_2\text{H}_3\text{O}_2)_2$  -derived  $\text{Co}_3\text{O}_4$  required the highest residence time, this can be seen in Table 7.4. The degradation percentage was always higher in the following order of precursor salt used:  $\text{Co}(\text{NO}_3)_2\cdot 6\text{H}_2\text{O} > \text{CoCl}_{12}\cdot 6\text{H}_2\text{O} > \text{Co}(\text{C}_2\text{H}_3\text{O}_2)_2$ . Taking the crystallite size of the  $\text{Co}_3\text{O}_4$  samples into account, regardless of the precursor salt, a lower crystallite size resulted in higher degradation. It was found that at higher surface areas the degradation of MO was higher and a clear relationship between the surface area of the  $\text{Co}_3\text{O}_4$  nanocatalyst and its degradation potential was established.

**Table 7.4: Operating parameters for maximum degradation of MO solution and surface area of best performing Co<sub>3</sub>O<sub>4</sub> nanoparticles**

Precursor Salt	Reaction Temperature (°C)	Precursor Concentration (M)	Residence time (h)	Degradation (%)	Surface area (m <sup>2</sup> /g)
Cobalt nitrate hexahydrate (Co(NO <sub>3</sub> ) <sub>2</sub> ·6H <sub>2</sub> O)	90	0.1	0.5	96.18	106.35
Cobalt chloride hexahydrate (CoCl <sub>2</sub> ·6H <sub>2</sub> O)	90	0.1	6	90.17	41.06
Cobaltacetate tetrahydrate (Co(C <sub>2</sub> H <sub>3</sub> O <sub>2</sub> ) <sub>2</sub> )	90	0.1	6	67.93	43.16

#### **7.2.4 Cost comparison analysis on the production and treatment cost of Co<sub>3</sub>O<sub>4</sub> via various precursors**

A cost comparison analysis on the synthesis cost of Co<sub>3</sub>O<sub>4</sub> via various cobalt precursors was used to evaluate the viability of treatment process to. Co(NO<sub>3</sub>)<sub>2</sub>·6H<sub>2</sub>O -derived Co<sub>3</sub>O<sub>4</sub> nanocatalyst was the most cost efficient while the catalyst produced from CoCl<sub>2</sub>·6H<sub>2</sub>O - precursor salt had the overall highest synthesis cost. Comparing the maximum yields produced, it was found that CoCl<sub>2</sub>·6H<sub>2</sub>O and Co(NO<sub>3</sub>)<sub>2</sub>·6H<sub>2</sub>O precursors resulted in the highest yield with the low synthesis costs while Co(C<sub>2</sub>H<sub>3</sub>O<sub>2</sub>)<sub>2</sub> precursor salt resulted in the lowest yield and highest cost.

This study found that Co(NO<sub>3</sub>)<sub>2</sub>·6H<sub>2</sub>O -derived Co<sub>3</sub>O<sub>4</sub> nanocatalyst is the most cost efficient and shows the best performance in the treatment of MO solution. The production process involved low reaction temperature and residence time to achieve the maximum yield whereas CoCl<sub>2</sub>·6H<sub>2</sub>O -derived and Co(C<sub>2</sub>H<sub>3</sub>O<sub>2</sub>)<sub>2</sub> -derived precursor salts had the higher requirements for the process conditions.

### 7.3. Recommendations for future studies

This study only evaluated reaction temperatures between 90°C and 180°C, precursor concentrations from 0.1 M to 0.5 M and residence times between 30 min and 6 hours. The ranges could be widened to establish the effect of the interaction at higher and lower process conditions. This study found the maximum yield produced under various conditions depended on the precursor that was used.

The effects of the agglomeration on the true surface area should be investigated.

The effect of the concentration of  $\text{Co}_3\text{O}_4$  nanocatalyst during the degradation process should be investigated. This will help determine if a sample that produced a higher yield with an original lower degradation percentage can achieve a higher degradation at a higher concentration.

The degradation study was done only using MO solution that was produced in a laboratory; further studies using the produced nanocatalyst should be done on the actual textile wastewater that contains various additives.

For future upscaling purposes an extensive economic analysis is required that makes use of the cost of industrial grade chemicals.

## Reference List

- Abel-Raouf, M. E., Maysour, N.E., Farag, R.K Abdul-Raheim and A.M. (2019) Wastewater treatment methodologies, Review article. *Environmental and Agricultural Sciences*, 3(1):1-25.
- Ahuja, S. and Scypinski, S. (2001) Handbook of Modern Pharmaceutical Analysis, Elsevier inc, USA.
- Albuquerque, A.S., Ardisson, J.D. and Macedo, W.A.A. (1999) A study of nanocrystalline NiZn-ferrite-SiO<sub>2</sub> synthesised by sol-gel. *Magnetism and Magnetic Materials*, 192(2): 277-280.
- Almeida, T. (2010) Hydrothermal synthesis and characterisation of  $\alpha$ -Fe<sub>2</sub>O<sub>3</sub> nanorods. Unpublished PhD thesis, University of Nottingham, United States.
- Al-Ghoul, M., El-Rassy, H., Coradin, T. and Mokalled, T. (2010) Reaction-diffusion based co-synthesis of stable a- and b- cobalt hydroxide in bio-organic gels. *Crystal Growth*, 312: 856-862.
- Ambroz, F., Macdonald, T.J., Martis, V. and Parkin, I.P. (2018) Evaluation of the BET theory for the characterization of Meso and Microporous MOF's. *Small Methods*, 1: 1-17.
- Anipsitakis, G.P. and Dionysiou, D.D. (2004) Radical generation by the interaction of transitional metals with common oxidants. *Environmental Science and Technology*, 38(13): 3705-3712, May.
- Anipsitakis, G. P. and Dionysiou, D. D. (2003) Degradation of organic contaminants in water with sulphate radicals generated by the conjunction of peroxymonosulfate with cobalt. *Environmental Science and Technology*, 37: 4790-4797.
- Anipsitakis, G. P., Stathatos, E. and Dionysiou, D. D. (2005) Heterogeneous activation of oxone using Co<sub>3</sub>O<sub>4</sub>. *Physical Chemistry B*, 109(27):13052 – 13055.
- Antony, J., Viles, E., Torres, A.F., and Uncerti, T. (2020) Design of experts in the service industry: a critical literature review and future research directions. *TQM*, 1-19.
- Arai, Y., Sako, T. and Takebayashi, Y. (2002) Supercritical fluids: molecular, interactions, physical properties, and new applications, Springer-Verlag, Nerlin Heidelberg, New York.
- Asghar, A., Raman, A.A. A. and Daud, W.M.A.W. (2014) A comparison of central composite design and taguchi method for optimizing fenton process. *Scientific World*, 1-14.

- Babu, S. G. and Karvembu, R. (2013) Copper based nanoparticles-catalyzed organic transformations, *Catalysis Surveys*, 17 (3 -4):156-176.
- Box, G.E.P., Hunter, J.S. and Hunter, W.G. (2005) Statistics for experimenters: Design, innovation, Wiley-Interscience, New Jersey.
- Brunauer, S., Emmett, P.H. and Teller, E. (1938) Adsorption of gases in multimolecular layers. *American Society*, 60(2): 309-319.
- Burkinshaw, S. (1995) Chemical principles of synthetic fibre dyeing. Blackie Academic & Professional, Springer, Switzerland.
- Byrappa, K., Ohara, S. and Adschiri, T. (2008) Nanoparticles synthesis using supercritical fluid technology – towards biomedical applications. *Advanced Drug Delivery*, 60(3):299- 327.
- Carey, G.H., Abdelhady, A.L., Ning, Z., Thon, S.M., Bakr, O.M. and Sargent, E.H. (2015) Colloidal Quantum Dot Solar Cells. *Chemical Reviews*, 115(23):12732-12763.
- Chaudhry, A.A. (2008) Continuous hydrothermal flow synthesis and characterisation of nanobioceramics and their rapid consolidation using spark plasma sintering. Unpublished PhD thesis submitted, University of London, London.
- Chorkendorff, I. and Niemantsverdriet, W. (2003) Concepts of modern catalysis and kinetics, Wiley, Weinheim.
- Chipasa, K. (2001) Limits of physicochemical treatment of wastewater in the vegetable oil refining industry. *Environmental Studies*, 10(3):141–148.
- Cullity, B.D. and Stock, S.R. (2001) Elements of X-ray Diffraction. Prentice-Hall, Inc USA: New Jersey.
- Cushing, C.B.L., Kolesnichenko, V.L. and O'Connor, C.J. (2004) Recent advances in the liquid-phase synthesis of inorganic nanoparticles. *Chemical Reviews*, 104(9), 3893-3946.
- Darr, J.A. and Poliakoff, M. (1999) New directions in inorganic and metal-organic coordination chemistry in supercritical fluids. *Chemical Reviews*, 99(2):495-541.
- Deng, Y. and Zhao, R. (2015) Advanced oxidation processes (AOPs) in wastewater treatment. *Current Pollution Reports*, 1(1): 167-176.
- Dehsari, H.S., Ribeiro, A.H., Ersoz, B., Tremel, W., Jakob, G. and Asadi, K. (2017) Effect of precursor concentration on size evolution of iron oxide nanoparticles. *CrystEngComm*, 19(44): 6694-6702.

Depgni, F., C.,T. (2020) Reused of a treated textile effluent from cobalt oxide and sulphate radical-based advanced oxidation process, Unpublished Master's thesis, Cape Peninsula University of Technology, Cape Town.

Dhawane, S.H., Kumar, T. and Halder, G. (2015) Central composite design approach towards optimization of flamboyant pods derived steam activated carbon for its use as heterogeneous catalyst in transesterification of Hevea brasiliensis oil. *Energy Conversion and Management*, 100: 277–287.

Dilaver, M., Hocoğlu, S.M., Soydemir, G., Dursun, M., Keskinler, B., Koyuncu, I. and Ağtaş, M. (2018) Hot wastewater recovery by using ceramic membrane ultrafiltration and its reusability in textile industry. *Cleaner Production*, 171(1): 220–233.

Donega, C., Lijeroth, P. and Vanmeaekelbergh, D. (2005) Physicochemical evaluation of the hot-injection method, a synthesis route for monodisperse nanocrystals. *Small: nano micro*, 1(12): 1152-1162.

Drever, J. (2005) *Water, Weathering and Soils*, Elsevier, UK: Oxford.

El-Batlouni, H. El-Rassy, H. and Al-Ghoul, M (2008) Cosynthesis, coexistence and self-organization and  $\alpha$  – and  $\beta$ -cobalt hydroxide based on diffusion and reaction in organic gels. *Physical Chemistry*,112(1):7755 -7757.

Evans, E. (2006) Continuous hydrothermal synthesis of inorganic nanoparticle, Unpublished PhD thesis,University of Nottingham, UK.

Frenkel A. I., Hills C.W. and Nuzzo R.G. (2001) A view from the inside: Complexity in the atomic scale ordering of supported metal nanoparticles. *Physical Chemistry B*, 105(51):12689-12703.

Gates, B.C. (2008) Catalysis: Individual nanoparticles in action. *Nature Nanotechnology*, 3(10); 583-584.

Ghaly, A., Ananthashankar, R., Alhattab, M. and Ramakrishnan, V. (2014) Production, characterization and treatment of textile effluents: a critical review. *Chemical Engineering & Process Technology*, 5(1):1-18.

Gunn, J.W. (2008) The preparation and characterization of superparamagnetic nanoparticles for biomedical imaging and therapeutic application, ProQuest LLC, Washington.

Hakuta, Y., S. Onai, H. Terayama, T. Adschiri and K. Arai (1998). Production of ultra-fine ceria particles by hydrothermal synthesis under supercritical conditions. *Materials Science Letters*, 17(14): 1211-1213.

Hao, Y. and Teja, A.S. (2003) Continuous hydrothermal crystallization of  $\alpha$ -Fe<sub>2</sub>O<sub>3</sub> and Co<sub>3</sub>O<sub>4</sub> nanoparticles. *Materials Research*, 18(2): 415-422.

Hassanzadeh, E., Farhadian, M., Razmjou, A. and Askari, N. (2017) An efficient wastewater treatment approach for a real woollen textile industry using a chemical assisted NF membrane process. *Environmental Nanotechnology, Monitoring and Management*, 8(1): 92–96.

Hayashi, H. and Torii, K. (2003) Hydrothermal synthesis of titania photocatalyst under subcritical and supercritical water conditions. *Material Chemistry*, 12 (3) 3671–3676.

Hayat, H., Mahmood, Q., Pervez, A., Bhatti, Z.A. and Baig, S.A. (2015) Comparative decolorization of dyes in textile wastewater using biological and chemical treatment. *Separation and Purification Technology*, 154(1): 149–153.

Helmersson, U., M., Lattemann, J., Bohlmark, A. P., and Ehasarian & Gudmundsson, J. T. (2006) Ionized physical vapor deposition (IPVD): A review of technology and applications. *Thin Solid Films*, 513(1–2): 1-24.

Huang, J., Ren, H., Chen, K. and Shim, J. (2014) Controlled synthesis of porous Co<sub>3</sub>O<sub>4</sub> micro/nanostructures and their photocatalysis property. *Superlattices and Microstructures*, 75:843 – 856.

Heuvel, W. (2020) Effect of precursor anion in alcohol/water solutions during hydro/solvothermal synthesis on cobalt oxide morphology and catalytic ability. Unpublished Master's thesis, Cape Peninsula University of Technology, Cape Town.

Hu, P. and Long, M. (2016) Cobalt-catalyzed sulfate radical-based advanced oxidation: A review on heterogeneous catalysts and applications. *Applied Catalysis B: Environmental*, 181(1): 103–117.

Hu, A., Yao, Z. and Yu, X. (2009) Phase behavior of a sodium dodecanolallyl sulfosuccinic diester/n-pentanol/methyl acrylate/butyl acrylate/water microemulsion system and preparation of acrylate latexes by microemulsion polymerization. *Applied Polymer Science*, 113(4): 2202–2208.

IMAP Group. (2014) Cobalt oxideL Human health tier II assessment, viewed on 18 March 2022

<[https://www.industrialchemicals.gov.au/sites/default/files/Cobalt%20oxide\\_Human%20health%20tier%20II%20assessment.pdf](https://www.industrialchemicals.gov.au/sites/default/files/Cobalt%20oxide_Human%20health%20tier%20II%20assessment.pdf)>

Jolivet, J., Chanèac, C., Prenè, P., Vayssières, L. and Tronc, E. (1997) Wet chemistry of spinel iron oxide particles. *Physics*, 7(1): 573-576.

Kawai-Nakamura, A., Sato, T., Sue, K., Tanaka, S., Saitoh, K., Aida, K. and Hiaki, T. (2008) Rapid and continuous hydrothermal synthesis of metal and metal oxide nanoparticles with a microtube-reactor at 523K and 30 MPa. *Materials Letters*, 62(19): 3471-3473.

Kim, J. H., Gibb, H. J., Howe, P. D. and Organization, W. H. (2006) Cobalt and inorganic cobalt compounds, viewed 29 September 2021, <<https://apps.who.int/iris/handle/10665/43426?locale-attribute=en>>.

Koyuncu, I. and Topacik, D. (2003) Effects of operating conditions on the salt rejection of nanofiltration membranes in reactive dye/salt mixtures. *Separation and Purification Technology*, 33(3): 283–294.

Kriedemann, B. and Fester, V. (2015) Critical process parameters and their interactions on continuous hydrothermal synthesis of ironoxide nanoparticles. *Chemical Engineering*, 281: 312 -321.

Kumar, C. (2009) Magnetic nanomaterials, Wiley-VCH, Weinheim.

Lester, E., Aksomaityte, G., Li, J., Gomez, S., Gonzalez, J.G. and Poliakoff, M. (2012) Controlled continuous hydrothermal synthesis of cobalt oxide (Co<sub>3</sub>O<sub>4</sub>) nanoparticles. *Progress in Crystal Growth and Characterization of Materials*, 58(1): 3-13.

Leyssence, L., Vinck, B., Van Der Straeten, C., Wuyts, F. and Maes, L. (2017) Cobalt toxicity in humans. A review of the potential sources and systemic health effects. *Toxicology*, 387: 43 -56.

Li, W. Y., Xu, L.N. and Chen, J. (2005) Co<sub>3</sub>O<sub>4</sub> nanomaterials in lithium-ion batteries and gas sensors. *Advanced Functional Materials*, 15(5): 851-857.

Lison, D. ( 2015) Cobalt. In Handbook on the toxicology of metals, MA: Elsevier, Waltham.

Liu, B. and Hu, X. (2020) Hollow micro- and nanomaterials: Synthesis and applications. *Advanced Nanomaterials for Pollutant Sensing and Environmental Catalysis*, 1: 1-38.

López Pérez, J.A., López Quintela, M. A., Mira, J., Rivas, J. and Charles, S.W. (1997) Advances in the preparation of magnetic nanoparticles by macroemulsion method. *Chemistry*, 101(41): 8045-8394.

Malik, M.A., Wani, M.Y. and Hashim, M.A. (2010) Microemulsion method: A novel route to synthesiz organic and inorganic nanomaterials. *Chemistry*, 5(4): 397 -417.

- Man, L., Niu, B., Xu, H., Cao, B. and Wang, J. (2011) Microwave hydrothermal synthesis of nanoporous cobalt oxides and their gas sensing properties. *Materials Research Bulletin*, 46(7): 1097-1101.
- Masterton, W. L., Hurley, C. N. and Neth, E. J. (2012) Chemistry: Principles and reactions, Brooks/Cole, USA: Belmont.
- Mathew, J. and Shetty, N. (2017) Treatment of wastewater using synthesised photocatalyst cobalt oxide  $\text{Co}_3\text{O}_4$ . *Civil Engineering and Technology*, 8(7):1840 -1844.
- Mayyahi, ,A.A. and Al-Asadi, H.A.A. (2018) Advanced oxidation processes (AOPs) for wastewater treatment and Reuse: A brief review, *Applied Sciences and Technology*, 2(3): 18 -30.
- McWilliams, A. (2010) Nanotechnology: A realistic market assessment. BBC Research, viewed 17 January 2021 <<https://www.bccresearch.com/market-research/nanotechnology/nanotechnology-realistic-market-assessment-nan031d.html>>.
- Mielby, J. J. (2014) Selective oxidations using nanostructured heterogeneous catalysts. Unpublished PhD thesis submitted at Technical University of Denmark, Technical University of Denmark , Denmark.
- Montgomery, D.C. (2017) Design and analysis of experiments, John Wiley and Sons, Hoboken.
- Morris, M. (2011) Design of experiments: An introduction based on linear models, CRC Press, Boca Raton.
- Munter, R. (2001) Advanced oxidation processes—current status and prospects. *Proceedings of the Estonian Academy of Sciences*, 50(1): 59-80.
- Murray, L., Mason, R.L., Gunst, R.F. and Hess, J.L. (1990) Statistical design and analysis of experiments, Wiley-Interscience, Hoboken.
- Nagpal, N.K. (2004) Technical report – water quality guidelines for cobalt.
- Nassar, M.Y. (2013) Size-controlled synthesis of  $\text{CoCO}_3$  and  $\text{Co}_3\text{O}_4$  nanoparticles by free-surfactant hydrothermal method. *Materials Letters*, 94: 112 -115.
- Nassar, M.Y. and Ahmed, I.S. (2011) Hydrothermal synthesis of cobalt carbonates using different counter ions: An efficient precursor to nano-sized cobalt oxide ( $\text{Co}_3\text{O}_4$ ). *Materials Research Bulletin*, 20(15): 2431-2437.

- Nassar, M.Y. and Ahmed, I.S. (2012) Template- free hydrothermal derived cobalt oxide nanopowders: synthesis, characterisation, and removal of organic dyes. *Materials Research Bulletin*, 47: 2638 – 2645.
- Nautiyal, A. and Shukla, S.R. (2018) Silver nanoparticles catalyzed reductive decolorization of spent dye bath containing acid dye and its reuse in dyeing. *Water Process Engineering*, 22: 276–285.
- Neale G. (1990) B12 binding proteins. *Gut*, 31(1): 59-63.
- Nidheesh, P. and Gandhimathi, R. (2012) Trends in electro-fenton process for water and wastewater treatment: an overview. *Desalination*, 299(1), 1-15.
- Noordin, M.Y., Venkatesh, V.C., Sharif, S., Elting, S. and Abdullah, A. (2004) Application of response surface methodology in describing the performance of coated carbide tools when turning AISI 1045 steel. *Materials Processing Technology*, 145(1): 46–58.
- Nolan, N. (2010) Sol-gel synthesis and characterization of novel metal oxide nanomaterials for photocatalytic applications. Unpublished PhD thesis, Dublin Institute of Technology, Dublin.
- Oztekin, E. and Altin, S. (2016) Wastewater treatment by electro-dialysis system and fouling problems. *Science and Technology*, 6(1): 91 – 99.
- Phillips, D. (1996) Environmentally friendly, productive and reliable: Priorities for cotton dyes and dyeing processes. *Society of Dyers and Colourists*, 112(7-8): 183-186.
- Phillips, M.J., Darr, J.A., Luklinska, Z.B. and Rehman, I. (2003) Synthesis and characterization of nano-biomaterials with potential osteological applications. *Material Science: Materials in Medicine*, 14 (10): 875-882.
- Pileni, M.P. (2003) Nanocrystals: fabrication, organization and collective properties. *Comptes Rendus Chimie*. 6(8 -10): 965–978.
- Poizot, P., Laruelle, S., Grugeon, S., Dupont, L. and Tarascon, J.M. (2000) Nano-sized transition-metal oxides as negative-electrode materials for lithium-ion batteries. *Nature*, 407(6803): 496-499.
- Punzi, M., Nilsson, F., Anbalagan, A., Svensson, B.M., Jönsson, K., Mattiasson, B. and Jonstrup, M. (2015) Combined anaerobic-ozonation process for treatment of textile wastewater: Removal of acute toxicity and mutagenicity. *Hazardous Materials*, 292(1) :52–60.

Rajasimman, M., Babu, S.V. and Rajamohan, N. (2017) Biodegradation of textile dyeing industry wastewater using modified anaerobic sequential batch reactor – Start-up, parameter optimization and performance analysis. *Taiwan Institute of Chemical Engineers*, 72(1): 171–181.

Ramaiah, K. S. (1999) Electrical properties of In doped CdS thin films. *Materials Science: Materials in Electronics*, 10(4): 291-294.

Raman, V., Suresh, S., Savarimuthu, P.A., Raman, T., Tsatsakis, A.M., Golokhvast, K.S. and Vadivel, V.K. (2016) Synthesis of Co<sub>3</sub>O<sub>4</sub> nanoparticles with block and sphere morphology, and investigation into the influence of morphology on biological toxicity. *Experimental and Therapeutic Medicine*, 11(2):553 – 560.

Reduan, N.A., Ghazali, S. and Jamari, S.S. (2016) Effect of temperature and NaCl concentration on synthesis of silver nanoparticles prepared in aqueous medium. *Engineering and Applied Sciences*, 11(10): 6399-6404.

Rivas, L., Gimeno, O., Carbajo, M. and Borralho, T. (2009) Catalytic decomposition of potassium monopersulfate. Influence of variables. *World Academy of Science, Engineering and Technology*, 57(1): 218-222.

Roco, M.C. (2001) International strategy for nanotechnology research. *Nanoparticle Research*, 3(5-6): 353 -360.

Salavati-Niasari, M., Khansari, A. and Davar, F. (2009) Synthesis and characterization of cobalt oxide nanoparticles by thermal treatment process. *Inorganic Chimica Acta*, 368(14): 4937-4942.

Said, K.A.M., Afizal, M. and Amin, M. (2015) Overview on response surface methodology (RSM) in extraction processes. *Applied Science & Process Engineering*, 2(1): 8-17.

Saputra, E., Duan, X., Pinem, J. A., Bahri, S. and Wang, S. ( 2017) Shape-controlled Co<sub>3</sub>O<sub>4</sub> catalysts for advanced oxidation of phenolic contaminants in aqueous solutions. *Separation and Purification Technology*, 186: 213 – 217.

Saputra, E., Muhammad, S., Sun, H., Ang, H.M., Tade, M.O. and Wang,S. (2013) A comparative study of spinel structured Mn<sub>3</sub>O<sub>4</sub>, Co<sub>3</sub>O<sub>4</sub> an Fe<sub>3</sub>O<sub>4</sub> nanoparticles in catalytic oxidation of phenolic contaminants in aqueous solution. *Colloid and Interface Science*, 407(1):467 – 473.

- Sette, S., Boullart, L. and Langenhove, L.V. (1996) Optimising a production by a neural network/genetic algorithm approach. *Engineering Applications of Artificial Intelligence*, 9(6): 681-689.
- Singh, S.B. and Tandon, P.K. (2014) Catalysis: A brief review on nano-catalyst. *Energy and Chemical Engineering*, 2(3):106 -115.
- Silva, V.D., Simoes, T.A., Grilo, J.P.F., Medeiros, E.S. and Macedo, A.A. (2020) Impact of NiO nanostructure morphology on the oxygen evolution reaction catalysis. *Material Sciences*, 55(15): 6648 – 6659.
- Somorjai, G.A. and Kliewer, C.J. (2009) Reaction selectivity in heterogeneous catalysis. *Reaction Kinetics and Catalysis Letters*, 96: 191-208, April.
- Speel, H.C. and Schwarz, E.W.K. (2013) Textile chemicals and auxiliaries with special reference to surfactants, Reinhold, California.
- Sreeja, P.H. and Sosamony, K.J. (2016) A comparative study of homogeneous and heterogeneous photofenton process for textile wastewater treatment. *Procedia Technology*, 24(2): 217–223.
- Starkey.C.L. (2016) Continuous-flow hydrothermal and solbothermal synthesis of inorganic nanomaterials. Unpublished PhD thesis, University of Nottingham, United Kingdom.
- Strifler, W. A. and Bates, C.W. (1992) Admittance spectroscopy of CuInSe<sub>2</sub>/CdS solar cells prepared by chemical spray pyrolysis. *Applied Physics*, 71(9): 4358-4364.
- Teja, A.S. and Koh, P.Y. (2009) Synthesis, properties, and applications of magnetic iron oxide nanoparticles. *Progress in Crystal Growth and Characterization of Materials*, 55(1-2): 22-45.
- Tjong, S. C. and Chen, H. (2004) Nanocrystalline materials and coatings. *Materials Science and Engineering: R: Reports*, 45(1–2): 1-88.
- Tisa, F., Raman, A.A.A. and Daud, W.M.A W. (2014) Applicability of fluidized bed reactor in recalcitrant compound degradation through advanced oxidation processes: a review. *Environmental Management*, 15(146): 260-275.
- Tran, H.N., Lee,C., Nguyen,T.V. and Chao. (2017) Saccharide-derived microporous spherical biochar prepared from hydrothermal carbonization and different pyrolysis temperatures: synthesis, characterization, and application in water treatment. *Environmental Technology*, 39(21):2747 - 2760.

- Trishitman, D., Cassano, A., Basile, A. and Rastogi, N.K. (2020) 9-Reverse osmosis for industrial wastewater treatment. *Current Trends and Future Developments on (Bio-) Membranes*, 207 -228.
- Wang, Y., Zhou, L., Duan, X., Sun, H., Tin, E.L., Jin, W. and Wang, S. (2015) Photochemical degradation of phenol solutions on Co<sub>3</sub>O<sub>4</sub> nanorods with sulfate radicals. *Catalysis Today*, 258(2): 576 – 584.
- Warang, T., Patel, N., Fernandes, R., Bazzanella, N. and Miotello, A. (2013) Co<sub>3</sub>O<sub>4</sub> nanoparticles assembled coatings synthesised by different techniques for photo- degradation of methylene blue dye. *Applied Catalysis B: Environmental*, 132-133: 204- 211.
- Williams, B.D. and Carter, C.B. (1996) *Transmission Electron Microscopy: A Textbook for Materials Science*, Springer, USA: Huntsville.
- Yadong, Y. and Alivisatos, A. (2005) Colloidal nanocrystal synthesis and the organic-inorganic interface. *Nature*, 437(7059): 664-670.
- Yadav, R.S., Mishra, P. and Pandey, A.C. (2007) Growth mechanism and optical property of ZnO nanoparticles synthesised by sonochemical method. *Ultrasonics Sonochemistry*, 15(5): 863-868.
- Yarestani, M., Khalaji, A.D., Rohani, A. and Das, D. (2014) Hydrothermal synthesis of cobalt oxide nanoparticles: Its optical and magnetic properties. *Sciences, Islamic Republic of Iran*, 25(4):339-343.
- Yimin, L. and Somorjai. (2010) Nano-scale advances in catalysis and energy applications. *Nano Letters*, 10(7): 2289 – 2295.
- Zhang, H., Choi, H. J. and Huang, C.-P. (2005) Optimization of fenton process for the treatment of landfill leachate. *Hazardous Materials*, 125(1-3): 166-174.
- Zhang, Z., Liu, Y., Yao, G., Zu, G., Zhang, X. and Ma, J. (2012) Solid-state reaction synthesis of NiFe<sub>2</sub>O<sub>4</sub> nanoparticles by optimizing the synthetic conditions. *Physica E: Low- dimensional Systems and Nanostructures*, 45 (1): 122 – 129.
- Zheng, Z. (2009) Synthesis and modifications of metal oxide nanostructures and their applications. Unpublished PhD thesis, Queensland University of Technology, Australia.

## Appendix A

### Basis of Safety and Safety Precautions

Table A.1 illustrates the equipment and materials that were used, their hazardous qualities and safety measures that were followed to avoid any harm to the student or environment.

Table A.1: Safety precautions on materials and equipment used.

Materials and Equipment	Hazards and Causes	Safety Measures
<b>Materials</b>		
Cobalt precursors (cobalt acetate tetrahydrate, cobalt sulphate and cobalt chloride hexahydrate)	Can cause shortness of breath when inhaled. Causes redness and pain if it comes into contact with a person's eyes. Abdominal pain is experienced when ingested.	All the proper personal protective equipment (PPE) was worn when any of the chemicals were handled, including: safety glasses, laboratory coat, dust mask, gloves and safety boots.
Cobalt oxide nanoparticles	Can cause shortness of breath when inhaled. Causes redness and pain if it comes into contact with a person's eyes. Abdominal pain is experienced when ingested.	
Water	Temperatures above 100°C are required and thus steam was present in the system. This caused a pressure build-up in the system.	
<b>Equipment</b>		
Oven / Furnace	A student could burn if the reactor was removed from the oven/furnace without the proper PPE.	I ensured that I received appropriate training before using any of the equipment All the appropriate PPE was worn when any of the chemicals were handled (see above).